Numerical evaluation of the Kalina cycle for concentrating solar power plants

Modi, Anish; Haglind, Fredrik; Clausen, Lasse Røngaard; Wieland, Christoph

Publication date:
2015

Document Version
Publisher's PDF, also known as Version of record

Numerical evaluation of the Kalina cycle for concentrating solar power plants

PhD Thesis

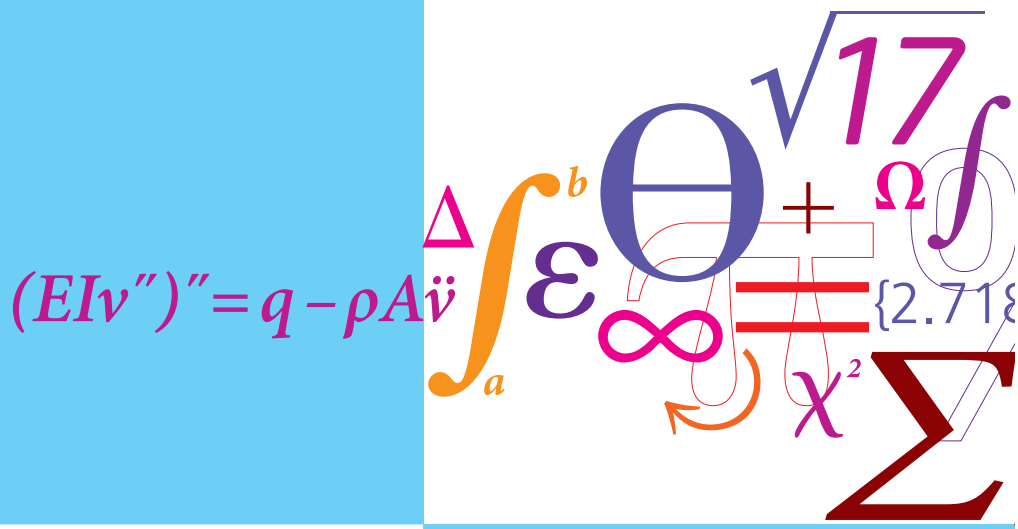

Anish Modi
DCAMM Special Report No. S188
August 2015

DTU Mechanical Engineering
Department of Mechanical Engineering

TECHNICAL UNIVERSITY OF DENMARK

Numerical evaluation of the Kalina cycle for concentrating solar power plants

Anish Modi

August 2015
Section of Thermal Energy, Department of Mechanical Engineering
Kongens Lyngby, Denmark

Numerical evaluation of the Kalina cycle for concentrating solar power plants

PhD Thesis
DCAMM Special Report No. S188
ISBN: 978-87-7475-430-5
Printed by GraphicCo A/S

DTU Mechanical Engineering
Section of Thermal Energy
Technical University of Denmark

Nils Koppels Allé, Building 403
DK-2800 Kongens Lyngby
Denmark

Phone: (+45) 4525 4131
Fax: (+45) 4588 4325
www.mek.dtu.dk

PREFACE

This thesis is submitted in partial fulfilment of the requirements for the degree of Doctor of Philosophy in Mechanical Engineering at the Technical University of Denmark (DTU).

The research was conducted at the Section of Thermal Energy, Department of Mechanical Engineering between 01st September 2012 and 31st August 2015 under the supervision of Fredrik Haglind and Lasse Røngaard Clausen from DTU and Christoph Wieland from Technische Universität München (TU Munich). The project was funded by DTU and included attending one semester of PhD level courses (30 ECTS points) and co-supervision of seven master theses.

The thesis is written as a monograph. The units are specified in the SI format and the costs are in United States Dollars ($), unless stated otherwise.

Acknowledgements

First and foremost, thanks to my supervisors Fredrik Haglind and Lasse Røngaard Clausen for giving me the opportunity to conduct research at the Section of Thermal Energy at DTU. It has been a great learning experience. To Fredrik, thank you for all the discussions, suggestions, and feedbacks, but most of all for the encouragement to always keep improving the work. To Lasse, thanks for the guidance during the early stages of the thesis and for the feedback on the thesis.

I am honoured to have Jóse González-Aguilar, Sotirios Karellas, and Brian Elmegaard in my thesis assessment committee. Thank you very much for the time and effort spent in evaluating the thesis, and for the helpful suggestions for its improvement.

Thanks to all the friends at the Section of Thermal Energy, in particular Martin and Jesper for so many fruitful discussions and useful inputs, and Jorrit, Ulrik, and Leonardo for being so patient and helping me multiple times during the project.

It has been a pleasure to share my office over the last three years with Thomas, Jonas, Christoffer, Pelle, Ju-hyuck, and Paride. Thank you all for so many interesting conversations, ranging from thermodynamics and heat transfer to Danish cakes and pastries. I will always cherish our time and travels together.

I am grateful to Hartmut Spliethoff for welcoming me to the Institute for Energy Systems at TU Munich as a guest researcher. I am also grateful to Christoph Wieland, my supervisor at TU Munich, for the discussions while I was in Munich and for the feedback on my thesis. Thanks Wei for the collaboration and for the wonderful suggestions on what to do in Munich!

As a PhD student, I have had the opportunity to interact and work with many talented bachelor and master students at DTU. Thank you all for the collaborations and for helping me look at things from several perspectives.

The research could not have been possible without the support of many excellent researchers and power industry personnel from around the world. Special thanks to Brian Ehrhart, University of Colorado at Boulder, USA for guiding me on using the DELSOL3 software and for providing a better insight into the working of central receiver solar power plants;

to Nishith Desai, Indian Institute of Technology Bombay, India for the helpful discussions on parabolic trough solar plants; to Eric Lemmon, National Institute of Standards and Technology, USA for the discussions on the estimation of the thermophysical properties of the ammonia-water mixtures and for providing the 'Ammonia (Lemmon)' fluid file for use with REFPROP; to Wolfgang Geisinger, Geothermie Unterhaching Produktions-GmbH & Co. KG, Germany for arranging a visit to the Unterhaching geothermal power plant and explaining the practical operation of the Kalina cycle; to S.M.I. Karimulla, Arani Power Systems Ltd, India for the information on the Kalina cycle turbines; and to Bengt Perers for always being so prompt in replying to my queries and providing the requested weather data files.

Lastly, I thank my family for all the love and encouragement. To my parents, I dedicate this thesis to you and thank you for making me what I am, I owe it all to you. To Bhumika, thank you for always being so supportive, loving, and patient, you complete me in more ways than I can describe. To Megha and Deepak, you bring us a lot of joy and I hope that you always stay happy and content.

Abstract

Concentrating solar power plants use a number of reflecting mirrors to focus and convert the incident solar energy to heat, and a power cycle to convert this heat into electricity. One of the key challenges currently faced by the solar industry is the high cost of electricity production. These costs may be driven down by developing more cost-effective plant components and improving the system designs. This thesis focuses on the power cycle aspect of the concentrating solar power plants by studying the use a Kalina cycle with ammonia-water mixtures as the cycle working fluid. The potential of using a Kalina cycle is evaluated with a thermoeconomic optimization with a turbine inlet temperature of 500 °C for a central receiver solar power plant with direct vapour generation, and 370 °C for a parabolic trough solar power plant with Therminol VP-1 as the solar field heat transfer fluid. No thermal storage is considered in this thesis.

A general methodology is presented to solve the high temperature Kalina cycle at both the design and the part-load conditions. Using this methodology, the plant was optimized by minimizing the levelized cost of electricity considering (1) the operation parameters from the Kalina cycle and the solar field design, (2) the part-load performances of both the Kalina cycle and the respective solar fields, and (3) the cost functions to estimate the capital investment and the operations and maintenance costs.

The results from this thesis indicate that the Kalina cycle has a higher specific capital investment cost and a higher levelized cost of electricity than the state-of-the-art steam Rankine cycle for both the central receiver and the parabolic trough plants. This is mainly because of worse power cycle design point efficiency than the corresponding steam Rankine cycle configuration and the higher capital investment cost of the power cycle itself. This causes the levelized cost of electricity for nearly all the considered Kalina cycle cases to be outside the range of the values for contemporary concentrating solar power plants. Therefore when considering both the thermodynamic and the economic perspectives, the results suggest that it is not beneficial to use the Kalina cycle for high temperature concentrating solar power plants.

Keywords: Concentrating solar power, central receiver, parabolic trough, Kalina cycle, ammonia-water mixture, thermoeconomic optimization.

Resumé

Udnyttelse af koncentreret solkraft kræver reflekterende spejle til at fokusere og konvertere solenergi til varme, samt et kraftværk til at konvertere denne varme til elektricitet. Den primære udfordring for solkraftindustrien er de høje omkostninger som er forbundet med elproduktionen. Disse omkostninger kan bringes ned ved udvikling af omkostningseffektive kraftværkskomponenter og ved at forbedre kraftværkets cyklusdesign. Denne afhandling fokuserer på kraftværkscyklussen ved at analysere brugen af Kalina-cyklussen med en blanding af ammoniak og vand som arbejdsmedium. Potentialet ved at bruge en Kalina-cyklus er evalueret ved hjælp af en termoøkonomisk optimering med en turbine-indgangstemperatur på 500 °C for et solkrafttårn med direkte dampproduktion, og 370 °C for et solkraftværk med parabolske trug der bruger Therminol VP-1 som varmeoverførende væske. Lagring af termisk energi er ikke taget i betragtning.

En generel metodik til løsning af Kalina-cyklussen ved design og dellast er præsenteret. Denne metodik benyttes til minimering af kraftværkets udjævnede elektricitetsomkostninger ved at tage driftsparametre fra Kalina-cyklussen og solfangernes design, dellastydelse for både Kalina-cyklussen og solfangerne samt funktioner til at estimere kapitalinvesteringer og drift- og vedligeholdsomkostninger med i betragtning.

Resultaterne indikerer at Kalina-cyklussen kræver en højere specifik kapitalinvestering og højere udjævnede elektricitetsomkostninger end de nyeste Rankine-cyklusser med damp som arbejdsmedium for både solkrafttårnene og de parabolske trug. Dette skyldes hovedsageligt en lavere designpunktsvirkningsgrad i forhold til Rankine-cyklussen og en højere kapitalinvestering for selve kraftværket. Dette betyder at de udjævnede elektricitetsomkostninger for næsten alle Kalina-cyklusserne som er taget i betragtning ligger udenfor intervallet for tidssvarende solkraftværker. Når både termodynamiske og økonomiske perspektiver tages i betragtning viser resultaterne dermed at det ikke er fordelagtigt at bruge Kalina-cyklussen ved høje temperaturer i koncentrerede solkraftværker.

Søgeord: Koncentreret solkraftværk, solkrafttårn, parabolske trug, Kalina-cyklus, ammoniak-vand-blanding, termoøkonomisk optimering.

PUBLICATIONS

The publications based on the work presented in this thesis are listed below. Chapter 3 of the thesis is partly based on the work presented in the journal paper 5, Chapter 4 is primarily based on the journal papers 2 and 3, and Chapter 5 is based on the work presented in the journal papers 1, 4, and 5.

Peer-reviewed journals

1. A. Modi, J.G. Andreasen, M.R. Kærn, and F. Haglind. *Part-load performance of a high temperature Kalina cycle*. Energy Conversion and Management 105:453-461, 2015.
2. A. Modi and F. Haglind. *Thermodynamic optimisation and analysis of four Kalina cycle layouts for high temperature applications*. Applied Thermal Engineering 76:196-205, 2015.
3. A. Modi and F. Haglind. *Performance analysis of a Kalina cycle for a central receiver solar thermal power plant with direct steam generation*. Applied Thermal Engineering 65:201-208, 2014.
4. M.R. Kærn, A. Modi, J.K. Jensen, J.G. Andreasen, and F. Haglind. *An assessment of in-tube flow boiling correlations for ammonia-water mixtures and their influence on heat exchanger size*. Applied Thermal Engineering, 93:623-638, 2016.
5. M.R. Kærn, A. Modi, J.K. Jensen, and F. Haglind. *An assessment of transport property estimation methods for ammonia-water mixtures and their influence on heat exchanger size*. International Journal of Thermophysics, 36:1468-1497, 2015.

Peer-reviewed conference proceedings

1. A. Modi, M.R. Kærn, J.G. Andreasen, and F. Haglind. *Economic optimization of a Kalina cycle for a parabolic trough solar thermal power plant*. 28th International Conference on Efficiency, Cost, Optimization, Simulation and Environmental Impact of Energy Systems (ECOS). Pau, France, 2015.
2. A. Modi and F. Haglind. *Optimisation of a Kalina cycle for a central receiver solar thermal*

power plant with direct steam generation. World Renewable Energy Congress XIII. London, UK, 2014.

3. A. Modi and T. Knudsen, F. Haglind, L.R. Clausen. *Feasibility of using ammonia-water mixture in high temperature concentrated solar power plants with direct vapour generation*. ISES Solar World Congress. Cancún, Mexico. Energy Procedia 57:391-400, 2014.

4. E. Baldasso, J.G. Andreasen, A. Modi, F. Haglind, and A. Stoppato. *Performance analysis a of solar driven organic Rankine cycle using multi-component working fluids*. 28th International Conference on Efficiency, Cost, Optimization, Simulation and Environmental Impact of Energy Systems (ECOS). Pau, France, 2015.

5. T. Knudsen, L.R. Clausen, F. Haglind, and A. Modi. *Energy and exergy analysis of the Kalina cycle for use in concentrated solar power plants with direct steam generation*.ISES Solar World Congress. Cancún, Mexico. Energy Procedia 57:361-370, 2014.

Contents

List of Figures

List of Tables

NOMENCLATURE

A	Area	$[\mathrm{m}^2]$
C	Cost	[$]
$\widehat{C}$	Specific cost	$[\$\,\mathrm{kW}^{-1}]$
CR	Geometric concentration ratio	
CRF	Capital recovery factor	
CSP	Concentrating solar power	
c_p	Isobaric specific heat capacity	$[\mathrm{J\,kg}^{-1}\,\mathrm{K}^{-1}]$
D	Diameter	[m]
DNI	Direct normal irradiance	$[\mathrm{W\,m}^{-2}]$
DST	Daylight savings time	[h]
D_i	Tube inside diameter	[m]
D_o	Tube outside diameter	[m]
E	Electricity	[MWh]
EOT	Equation of time	[min]
F	Focal length	[m]
f	Factor, defined locally where used	
F_{cu}	Copper loss fraction	
GA	Genetic algorithm	
H	Height	[m]
h	Specific enthalpy	$[\mathrm{J\,kg}^{-1}]$
IAM	Incidence angle modifier	
k_d	Real debt interest rate	
k_i	Annual insurance rate	
k_{tur}	Turbine constant	$[\mathrm{kg\,K}^{0.5}\,\mathrm{s}^{-1}\,\mathrm{bar}^{-1}]$
L	Length	[m]
LCOE	Levelized cost of electricity	$[\$\,\mathrm{MWh}^{-1}]$
LMTD	Logarithmic mean temperature difference	[°C]
M	Molar mass	$[\mathrm{g\,mol}^{-1}]$
$\dot{m}$	Mass flow rate	$[\mathrm{kg\,s}^{-1}]$
N_d	Number of day of the year	
N_p	Plant lifetime in years	[a]

N_{tur}	Turbine rotational speed	[rpm]
O&M	Operations and maintenance	
p	Pressure	[bar]
PCF	Plant capacity factor	
PPTD	Pinch point temperature difference	[°C]
$\dot{Q}$	Rate of heat transfer	[W]
SM	Solar multiple	
T	Temperature	[°C or K]
$\overline{T}$	Average temperature	[°C or K]
U	Overall heat transfer coefficient	$[\mathrm{W\,m^{-2}\,K^{-1}}]$
$\dot{V}$	Volumetric flow rate	$[\mathrm{m^3\,s^{-1}}]$
W	Width	[m]
$\dot{W}$	Mechanical or electrical power	[W]
X	Vapour quality	$[\mathrm{kg\,kg^{-1}}]$
x	Ammonia mass fraction	$[\mathrm{kg\,kg^{-1}}]$
y	Ammonia mole fraction	$[\mathrm{mol\,mol^{-1}}]$

Greek letters

α	Heat transfer coefficient	$[\mathrm{W\,m^{-2}\,K^{-1}}]$
α_{col}	Collector absorptivity	
β	Angle associated with the number of day of the year	[°]
δ	Declination angle	[°]
ϵ_{rec}	Receiver emissivity	
η	Efficiency	
γ_s	Solar azimuth angle	[°]
λ	Thermal conductivity	$[\mathrm{W\,m^{-1}\,K^{-1}}]$
μ	Dynamic viscosity	[Pa s]
ω	Hour angle	[°]
ϕ	Latitude, North positive	[°]
Φ	Objective function	
π	Mathematical constant, 3.1416	
ψ	Longitude, West positive	[°]
ψ_m	Standard meridian, West positive	[°]
ρ	Density	$[\mathrm{kg\,m^{-3}}]$
ρ_{col}	Collector reflectivity	
σ_{SB}	Stefan-Boltzmann constant, $5.669 \times 10^{-8}\ \mathrm{W\,m^{-2}\,K^{-4}}$	
θ	Incidence angle	[°]
θ_z	Zenith angle	[°]
ζ	Relative load	

Subscripts, including components

abs	Absorber or absorbed

amb	Ambient
amm	Ammonia
atm	Atmospheric transmittance
bel	Bellows shadowing
blo	Blocking
blr	Boiler
cd	Condenser
CF	Cost function
cln	Cleanliness
cnt	Contingencies
cold	Cold fluid
conv	Convection
cos	Cosine
crit	Critical
cw	Condenser cooling water
cy	Cycle
d	Design condition
dst	Dust loss
el	Electrical equipment and material
end	End loss
eqp	Equipment
fix	Fixed
for	Forced convection
gen	Generator
geo	Geometric accuracy
gls	Glass envelope
hot	Hot fluid
htf	Heat transfer fluid
hx	Heat exchanger
i	i^{th} control volume
in	Inlet or input
inc	Incident
insc	Instrumentation and control
inst	Installation
inv	Capital investment
is	Isentropic
land	Land
lm	Logarithmic mean temperature difference
loop	Parabolic trough loop
loss	Heat loss
m	Mechanical

M&S	Marshall and Swift equipment cost index
min	Minimum
misc	Miscellaneous
mx	Mixer
nat	Natural convection
net	Net electrical power output
out	Outlet or output
PC	Power cycle
pip	Piping
PL	Plant
pl	Part-load condition
pp	Pinch point
pres	Pressure
pt	Parabolic trough collector and receiver
pu	Pump
rad	Radiation
re	Recuperator
rec	Receiver
sep	Separator
SF	Solar field
sha	Shadowing
site	Site improvement
spa	Spacing
spg	Spillage
spl	Splitter
temp	Temperature
th	Thermal
thv	Throttle valve
tow	Tower for the central receiver solar field
trk	Tracking and twisting error
tube	Heat exchanger tube
tur	Turbine
var	Variable
wat	Water
y	Yearly or annual

1

INTRODUCTION

This chapter presents the general context for the thesis research topic, the research motivation and objectives, the overall research methodology, and an outline of the thesis.

1.1 Context

In order to mitigate the adverse climatic effects caused by using fossil fuels, renewable energy based systems have recently attracted increased interest as a clean and sustainable way of satisfying our energy demands. In this regard, several countries have adopted ambitious climate and energy targets. These include, for example, Denmark setting a target of becoming a 100 % renewable energy based society and Sweden seeking to reduce its greenhouse gas emissions by 100 % by 2050 as compared with the 1990 emission levels [1]. Similarly, India plans to install 20 GW of grid connected solar power systems by 2020 [2] while China has a target of installing 3 GW of concentrating solar power (CSP) plants by 2020 [3]. A full list of such renewable energy targets for various countries from around the world is presented in the recent REN21 report [3].

The five ultimate primary energy sources on earth are (1) the sun, (2) the motion and the gravitational potential of the earth, the sun, and the moon, (3) geothermal energy, (4) human-induced nuclear reactions, and (5) the chemical reactions from mineral sources [4]. Of these, the three renewable sources of energy are shown in Figure 1.1 – the sun, the geothermal energy from the earth, and the energy from the planetary motion. The thermal energy from the earth can be utilized by using the hot water from aquifers. This energy can be used to satisfy the space heating and power demands through the geothermal heating and power plants. The tides formed in the oceans around the world due to the motion of the sun and the moon relative to the earth contain a significant amount of energy. This energy can be harvested to generate electricity.

As may be observed from Figure 1.1, the incident power from the sun is clearly the dominant renewable energy resource. Even though the solar radiation is abundantly available, it is challenging from both practical and economic perspectives to utilize it all. The two most

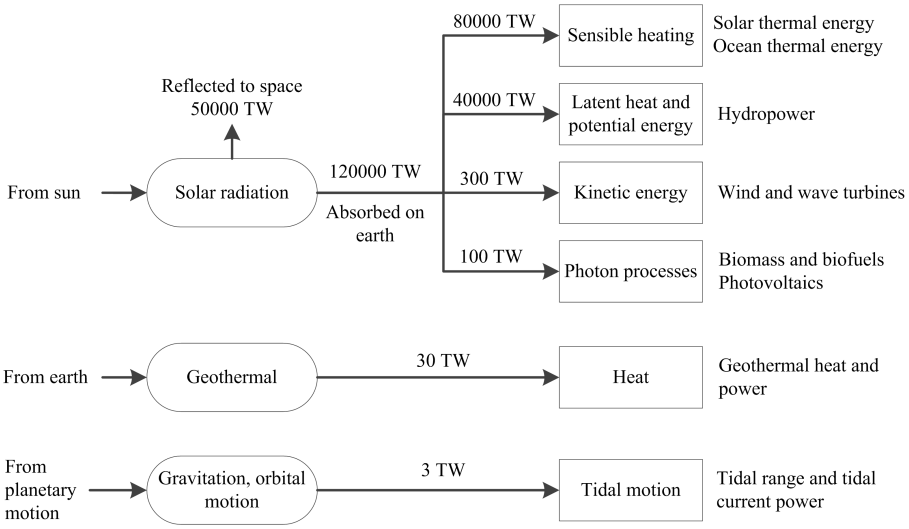

Figure 1.1: Renewable energy sources [4].

commonly used technologies to convert the incident solar radiation into electricity are the solar photovoltaic systems and the CSP plants. The solar photovoltaic systems directly convert sunlight into electrical energy, and have been proposed for electricity production [5], refrigeration [6], polygeneration [7], and the improvement of the indoor environment [8]. On the other hand, the CSP plants first convert the incident solar radiation to heat through concentration and then convert this heat into electricity through conventional power cycles such as the steam Rankine cycle [9,10].

The International Energy Agency estimates that by the year 2050, the solar energy systems will be supplying about 17 % of the global electricity demand in the 2 degree rise scenario, and about 27 % in the 2 degree rise, high renewable energy mix scenario [11]. The 2 degree rise scenario means that the average global temperature rise should be kept below 2 °C as compared with the pre-industrial levels. In the high renewable energy mix scenario, the above share makes solar the dominant source for electricity. The share of the solar thermal electricity is respectively 7 % and 11 % in the two scenarios. This amounts to about 646 GW and 954 GW of installed CSP plant capacity, respectively. In comparison, the total CSP plant installed capacity as of 2013 was merely about 3.4 GW [3]. This huge gap between the current and the estimated future CSP capacities is primarily due to the high investment costs and the challenges towards managing the fluctuating nature of the source. However with a surge in the research and development in the past few years, CSP plants are rapidly gaining interest as viable candidates for large scale electricity generation [12,13].

A typical CSP plant will always have a solar field (including the collectors and the receivers) to concentrate the available energy in the sunlight and a power cycle (or *power block*) to

convert the heat obtained through concentration into electricity. In addition, a thermal energy storage system could also be present to store excess heat and use it in times of little or no sunshine. The large investment costs of the CSP plants can be driven down by research in any of these areas through development of more cost-effective components and improved system designs. This thesis focuses on the power cycle aspect of the CSP plants by investigating the use of a fluid mixture as the cycle working fluid.

1.2 Motivation

The motivation behind the current study is that the irreversibility during a heat transfer process can be reduced by using a *zeotropic mixture* which evaporates and condenses at a varying temperature, contrary to the isothermal evaporation and condensation of a pure fluid [14]. In addition, using a mixture instead of a pure fluid allows the designer to have an additional degree of freedom in terms of varying the mixture composition in order to obtain better performance from the power cycle. One such working fluid is the mixture of ammonia and water which is used in a Kalina cycle [15], and to the author's knowledge, the use of a Kalina cycle in high temperature CSP plants has never been investigated before.

The reduction in the irreversibility during the heat transfer using a fluid mixture however comes at a price of increased heat exchanger areas and the need to use a complex cycle layout. These compromises have economic consequences. Hence, for a thorough analysis, it is important to consider the total thermoeconomic performance of the power cycle including the thermodynamic design, the part-load performance, and the economic aspects. These criteria define the key research question for this thesis: will the use of an ammonia-water mixture as a working fluid in high temperature CSP plants result in an economic advantage over the state-of-the-art steam Rankine cycle CSP plants?

1.3 Research objectives

The primary objective of this thesis is to evaluate the thermoeconomic potential of using a Kalina cycle with CSP plants. Only high temperature cycles are considered in the thesis, i.e. with a turbine inlet temperature of 500 °C for a central receiver CSP plant with direct vapour generation, and 370 °C for a parabolic trough CSP plant with a thermal oil as the solar field heat transfer fluid. The main objective is achieved through the following sub-objectives: (1) thermodynamic analysis of the Kalina cycle performance at different turbine inlet pressures and ammonia mass fractions, (2) thermoeconomic optimization of the Kalina cycle for a central receiver CSP plant and a parabolic trough CSP plant, and (3) the comparison of the Kalina cycle performance with that of the state-of-the-art steam Rankine cycle.

1.4 Overall methodology

Figure 1.2 shows the overall methodology for the thesis. In order to carry out the thermoeconomic optimization, a computationally efficient algorithm to thermodynamically solve and design the Kalina cycle was first developed. Using the required design heat input to the Kalina cycle, the solar field size and layout were determined. The central receiver and the parabolic trough solar fields were modelled for the respective CSP plants. Using the power cycle and the solar field design parameters, the respective part-load performances were determined. Suitable cost functions, along with the plant operation strategy and site solar radiation data, were then used to estimate the levelized cost of electricity (LCOE) for the Kalina cycle CSP plants. The LCOE was then minimized as a part of the thermoeconomic optimization. Since it is a first attempt to analyse the Kalina cycle for CSP applications, it was decided to exclude storage systems and fossil backup from the study.

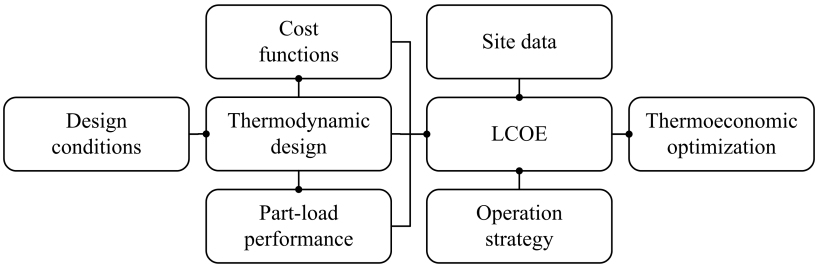

Figure 1.2: Overall project methodology.

All the simulations for the Kalina cycle were run using MATLAB R2015a [16]. The central receiver solar field was designed using DELSOL3 [17], whereas the parabolic trough solar field was simulated with MATLAB. The simulations for the state-of-the-art steam Rankine cycle were run using System Advisor Model 2015.6.30 [18]. As System Advisor Model uses a similar approach for the central receiver CSP plants as DELSOL3 and as the parabolic trough model in this thesis broadly follows the methodology outlined in System Advisor Model, it is reasonable to compare the Kalina cycle simulation results with the steam Rankine cycle simulation results from System Advisor Model. The thermodynamic properties for the ammonia-water mixtures were estimated using REFPROP 9.1 [19].

1.5 Thesis outline

The rest of the thesis is structured as follows.

Chapter 2 presents a general background on the CSP systems. The various parts of a CSP plant (the solar field, the power block, and the storage system) are briefly described with a more detailed overview of the central receiver and the parabolic trough solar fields.

Chapter 3 presents a general background on the Kalina cycles for both low and high temperature applications. An overview of the thermodynamic and transport property estimation methods for the ammonia-water mixtures is also presented along with different cycle configurations.

Chapter 4 presents a detailed algorithm to solve and optimize the Kalina cycle for a high temperature CSP plant. The results from the thermodynamic optimization are presented and analysed.

Chapter 5 presents a methodology to solve the Kalina cycle at part-load conditions, an algorithm for the thermoeconomic optimization of the Kalina cycle CSP plants, and the results from the optimization. The performance of the Kalina cycle CSP plants is then compared with that of the state-of-the-art steam Rankine cycle CSP plants.

Chapter 6 concludes the thesis with a summary of the modelling approach, the key findings, and suggestions for future research.

The thesis is ended with a list of references, the appendices, and a glossary with the definitions of some important terms. The definitions for the glossary have primarily been referred from Winter et al. [9], Lovegrove and Stein [10] and Kistler [20].

2

CONCENTRATING SOLAR POWER

This chapter presents a brief overview of the available solar resource, the different kinds of CSP plants based on the collector types and the power cycles, and the various sections of a typical CSP plant.

2.1 Solar radiation

The solar radiation incident on any collector surface on earth mainly consists of the direct, the diffuse, and the reflected components. These are illustrated in Figure 2.1. The direct or beam radiation is the solar radiation received without being scattered by the atmosphere, while the diffuse radiation is the solar radiation received after scattering by the atmosphere. The reflected radiation is the radiation reflected from the ground to the surface under consideration.[1]

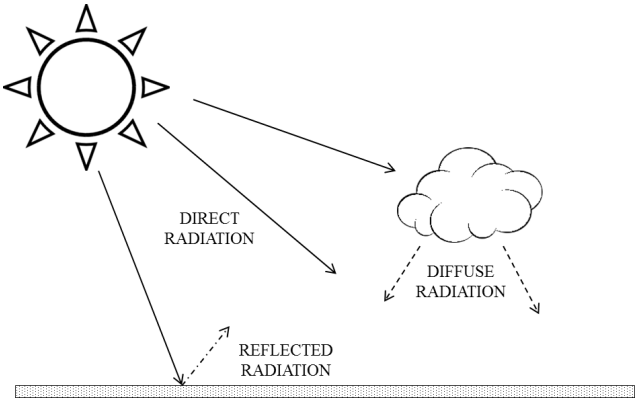

Figure 2.1: Solar radiation components.

In order to determine the available solar radiation at any time of the day on any day of the year, it is necessary to know the position of the sun in the sky along with the latitude (ϕ)

[1] All the definitions and equations presented in this section are referred from Duffie and Beckman [21].

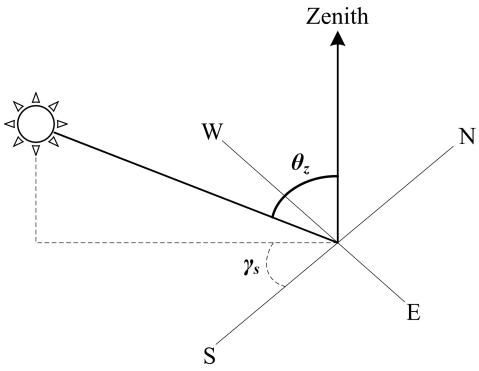

Figure 2.2: Sun-earth geometry and solar angles.

and longitude (ψ) of the plant site. The position of the sun in the sky can be described using the zenith angle (θ_z) and the solar azimuth angle (γ_s), as shown in Figure 2.2. The letters 'N', 'S', 'E', and 'W' represent respectively the north, south, east, and west directions. The *zenith* is the vertical line from any point on the earth and the zenith angle (θ_z) is defined as the angle between this vertical line and the line joining the sun with the location on earth. The solar azimuth angle (γ_s) is the angular displacement of the projection of the solar beam from south direction. The following text presents the mathematical equations to calculate the above angles.[2]

The zenith angle (θ_z) can be found using:

$$\theta_z = \cos^{-1}\left(\cos\phi \cdot \cos\delta \cdot \cos\omega + \sin\phi \cdot \sin\delta\right) \tag{2.1}$$

where δ is the declination angle which is defined as the angular position of the sun at solar noon with respect to the plane of the equator. This angle is always between $-23.45°$ and $23.45°$, the range of the tilt of earth's axis. The hour angle (ω) is the angular displacement of the sun, east or west of the local meridian, due to the rotation of the earth on its axis at $15°$ per hour. It is negative in the morning and positive in the afternoon. The declination angle (δ) depends on the day of the year and can be found using:

$$\delta = \frac{180}{\pi} \cdot \left(\begin{array}{l} 0.006918 - 0.399912 \cdot \cos\beta + 0.070257 \cdot \sin\beta - 0.006758 \cdot \cos 2\beta \\ + 0.000907 \cdot \sin 2\beta - 0.002697 \cdot \cos 3\beta + 0.00148 \cdot \sin 3\beta \end{array} \right) \tag{2.2}$$

where β is calculated depending on the number of day (N_d) in the year as follows:

$$\beta = \frac{360}{365} \cdot (N_d - 1) \tag{2.3}$$

[2] Note that all the equations and descriptions mentioned in this study are valid only for plant locations in the northern hemisphere. These will need to be modified if the plant is located in the southern hemisphere.

The hour angle (ω) can be found using:

$$\omega = 15 \cdot (t_{\text{sol}} - 12) \tag{2.4}$$

where the solar time (t_{sol}) and the local clock time (t_{clk}) are related as follows:

$$t_{\text{sol}} = t_{\text{clk}} + \frac{\psi_m - \psi}{15} + \frac{\text{EOT}}{60} - \text{DST} \tag{2.5}$$

where ψ is the site longitude, ψ_m is the standard meridian for the site location, EOT is the equation of time in min, and DST is the daylight saving time in h, if applicable. The value of DST in the above equation is equal to 1 if it is employed (typically during summer) and equal to zero if it is not (typically during winter). The value of the equation of time (EOT) in minutes can be found using:

$$\text{EOT} = 229.2 \cdot \begin{pmatrix} 0.000075 + 0.001868 \cdot \cos\beta - 0.032077 \cdot \sin\beta \\ - 0.014615 \cdot \cos 2\beta - 0.04089 \cdot \sin 2\beta \end{pmatrix} \tag{2.6}$$

where the value of β is given by Equation (2.3).

The solar azimuth angle (γ_s) can be found using:

$$\gamma_s = \text{sgn}(\omega) \cdot \left| \cos^{-1} \left(\frac{\cos\theta_z \cdot \sin\phi - \sin\delta}{\sin\theta_z \cdot \cos\phi} \right) \right| \tag{2.7}$$

where 'sgn' represents the sign function.

2.2 Concentration

In order to operate any power plant, the temperature of heat supply must be higher than the temperature of heat rejection. In a CSP plant, a high temperature of the heat supply is achieved by concentrating the solar energy using mirrors or reflectors on a relatively smaller receiver area. The heat available on the receiver surface can be extracted using a heat transfer fluid which then delivers it to the power cycle. The ratio of the collector aperture area (A_{col}) to the receiver area (A_{rec}) is called the geometric concentration ratio (CR) and it signifies the intensification of the incident solar radiation:

$$\text{CR} = \frac{A_{\text{col}}}{A_{\text{rec}}} \tag{2.8}$$

In a CSP plant, only direct radiation can be utilized because of the possibility to concentrate it by changing its direction through a collector-receiver system. The incident direct solar radiation is usually concentrated by using either a *line focusing* or a *point focusing* collector-receiver system. An illustration of the four most common collector-receiver systems

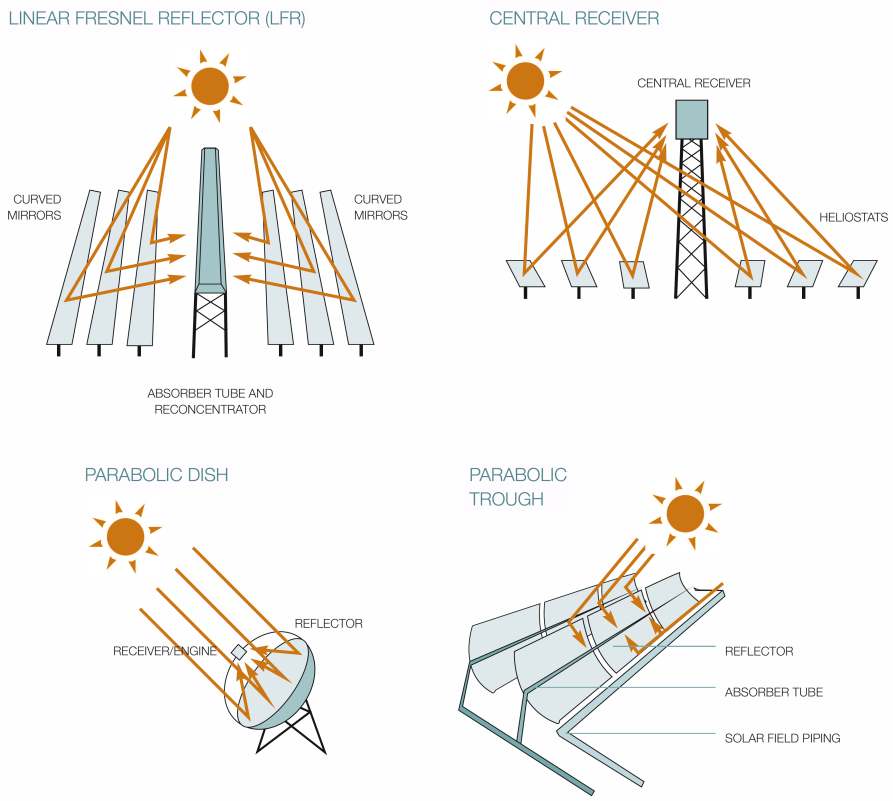

Figure 2.3: Line and point focusing collector-receiver systems [13].

is shown in Figure 2.3. The line focusing systems have a two-dimensional concentration with the solar radiation concentrated along a line. This is done using the parabolic troughs or the linear Fresnel reflectors, where the radiation reflected from the mirror surface is absorbed in a receiver tube. These systems usually employ a single-axis tracking mechanism. The point focusing systems have a three-dimensional concentration with the solar radiation concentrated on a 'point'. This is done using the central receiver or the parabolic dish systems. These systems usually employ a two-axis tracking mechanism.

A schematic of the energy flow through the different parts of a solar-only CSP plant – the solar field including the collector and the receiver, the thermal energy storage, and the power cycle – is shown in Figure 2.4. The different parts are then briefly explained in the coming sections. There will of course be energy losses during all the transfers, but they are not shown in the figure for simplification.

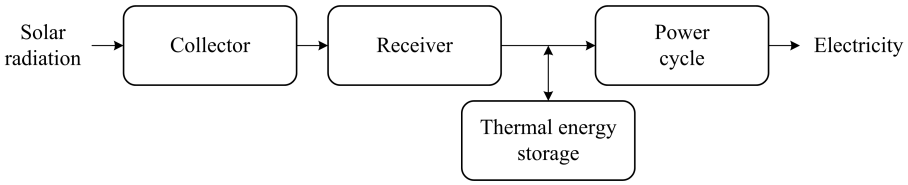

Figure 2.4: Energy flow through a solar-only CSP plant.

2.3 Solar field

The solar field comprises of the collector-receiver system which is used to collect the energy available in the incident solar radiation and transfer it to a receiver. From the receiver, the received thermal energy can either be transported to a thermal energy storage system, or to a power cycle for conversion to electricity. The size of the solar field is usually specified in terms of the collector aperture area which depends on the power cycle design heat input and the storage capacity. The ratio of the power delivered by the solar field at design condition ($\dot{Q}_{\mathrm{SF,d}}$) to the power required by the power cycle to operate at nominal conditions ($\dot{Q}_{\mathrm{SF,PC,d}}$) is called solar multiple (SM). It is defined as follows [22]:

$$\mathrm{SM} = \frac{\dot{Q}_{\mathrm{SF,d}}}{\dot{Q}_{\mathrm{SF,PC,d}}} \tag{2.9}$$

In other words, it is the ratio by which the solar field is oversized with respect to the power cycle design heat input requirements, and therefore is always ≥ 1. If a storage system is present in the plant, then it is a must to have an oversized solar field, i.e. a solar multiple greater than 1, to be able to simultaneously charge the storage and operate the power cycle at design point. Even if there is no storage in the CSP plant, it might still be interesting to have a solar multiple greater than one to improve the CSP plant capacity factor. The plant capacity factor (PCF) is the ratio of the actual output of a plant over a period to the maximum possible output during the same period (which is when the plant operates at its rated or 'nameplate' capacity all the time). The capacity factor is usually defined using annual values:

$$\mathrm{PCF} = \frac{E_{\mathrm{y}}}{\dot{W}_{\mathrm{net,d}} \cdot 8760} \tag{2.10}$$

where E_{y} and $\dot{W}_{\mathrm{net,d}}$ are respectively the amount of electricity generated by the power plant in one year and the plant's net electrical power output at the design point of operation, while 8760 is the number of hours in a typical year. A higher solar multiple will allow the plant to run at design point for more hours per year even when the incident solar radiation is less than the design value. However it also means a higher capital investment cost for the larger solar field. Thus, there will always be a compromise between increasing the solar multiple and reducing the overall cost of electricity production.

Among the concentration technologies commonly used today (Figure 2.3), the central receiver and the parabolic trough are the most developed ones and occupy nearly all the market share for both the currently operational and the under-construction CSP plants [23]. Therefore, these two solar fields are considered in this study.

2.3.1 Central receiver

The three main parts of a central receiver solar field are the heliostat mirror collectors, the central receiver, and the tower. Along with these, there will be auxiliary equipment such as electrical wiring, the support structures, and the tracking motors. The heliostats are large mirrors with two-axis tracking and come in various sizes and shapes. An example is shown in Figure 2.5. These heliostats reflect the incident sunlight on to the central receiver as illustrated in Figure 2.3.

Figure 2.5: Heliostat mirror [24].

Most of the receivers can be broadly classified as external cylindrical, cavity, or volumetric. An external cylindrical receiver is shown in Figure 2.6.

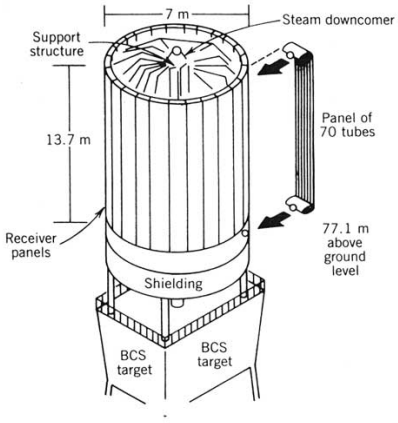

Figure 2.6: External cylindrical central receiver with water/steam as the heat transfer fluid [25].

As the name suggests, a number of tubes are arranged in a cylindrical manner and the solar radiation from the heliostats is focused on the outer surface of the receiver cylinder. This type of receiver is typically used with molten salt or water/steam as the heat transfer fluid. With the same heat transfer fluids, a cavity receiver can also be used. A cavity receiver is a closed enclosure with a large opening (cavity) on one side with the tube bundles inside. Figure 2.7a shows the view from the top of a cavity receiver.

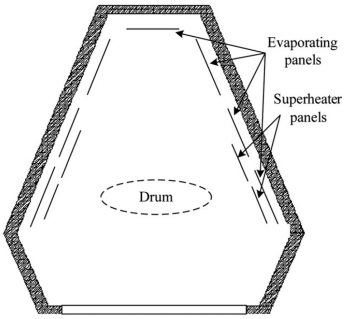

(a) Top view of a cavity receiver [26].

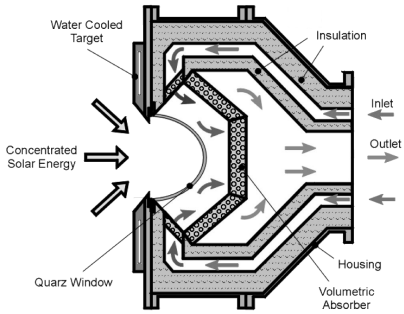

(b) Pressurized volumetric receiver [27].

Figure 2.7: Cavity and volumetric receivers with water/steam and air as the respective heat transfer fluids.

A volumetric receiver is primarily used with air as the heat transfer fluid as shown in Figure 2.7b. The key difference between the tube-based external cylindrical and cavity receivers and the volumetric receivers is that the absorber in a volumetric receiver is made of a porous material such as ceramic foam [27]. The air passes through this porous material where the heat generated by concentrating the solar radiation is transferred to the air. Another difference between the different receivers is in the possibility to use a surround or a north heliostat field as shown in Figure 2.8.

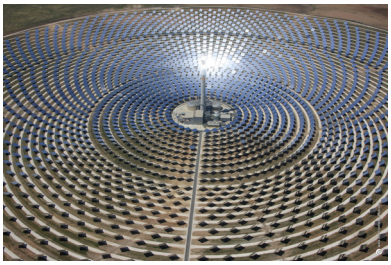

(a) Surround heliostat field [28].

(b) North heliostat field [29].

Figure 2.8: Surround and north heliostat fields.

In a surround field, the heliostats surround the tower; whereas in a north field, only the area north of the tower is used for placing the heliostats. The external cylindrical receiver operates with a surround field, whereas the cavity and the volumetric receivers operate

with a north field. A detailed review of the high temperature receiver designs was recently conducted by Ho and Iverson [30]. The receiver is mounted on the top of a tower in order to improve the concentration optics when using a large heliostat field. Depending on the tower height, the tower could either be made with mainly a concrete structure, or with a steel structure. Usually, the towers shorter than 120 m in height are steel towers, whereas the towers which are 120 m or more in height are concrete towers [20].

2.3.2 Parabolic trough

A parabolic trough solar field consists of a parabolic trough collector and a receiver tube along with the support structure, hydraulic drives, electrical wiring, tracking motors, and the joints connecting the tubes between two collector assemblies. Figure 2.9 shows the parabolic trough collector-receiver assembly. A highly reflecting material such as silver is used behind a glass surface to construct the collector surface [31]. These surfaces are curved in the shape of a parabola with the receiver tube passing through the focal line of this parabola. Typically, the rows of the parabolic trough collector-receiver systems are either aligned in the North-South direction with East-West tracking, or in the East-West direction with North-South tracking.

Figure 2.9: Parabolic trough collector-receiver system [32].

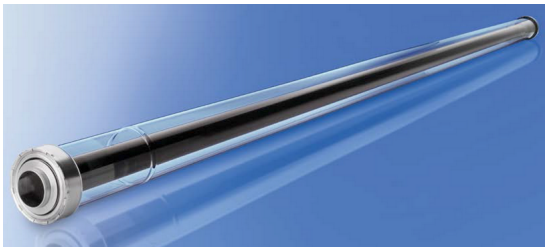

Figure 2.10: Parabolic trough receiver [33].

The parabolic trough receiver, as shown in Figure 2.10, has a metallic absorber tube through which the heat transfer fluid flows while collecting the energy from the concentrated solar

radiation. The metallic tube is surrounded by a glass tube with vacuum in-between. The vacuum enclosure significantly reduces the heat losses at high operating temperatures while protecting the solar-selective absorber surface from oxidation [31].

2.4 Thermal energy storage

The use of thermal storage systems allows to increase the CSP plant operation hours beyond the sunny periods, thus improving the plant dispatchability, i.e. the ability of the plant to generate electricity when desired. The high temperature thermal storage systems for CSP plants can be classified in two ways: (1) on the basis of the storage medium, and (2) on the basis of the storage system arrangement in the plant.

On the basis of the storage medium, the thermal storage systems can be sensible, latent, or thermochemical systems [34]. In the sensible storage systems, the phase of the storage medium does not change and the heat exchange only occurs with a change in the temperature. In such a system, the heat will be transferred to the storage medium by raising its temperature, while it will be extracted by cooling it down. Examples of such a medium are molten salt, thermal oil, concrete, etc. [34,35]. The latent storage systems use a phase change material as the storage medium where the energy is stored by changing the phase of the medium. In such systems, the heat is transferred to the storage medium by melting it, while it is extracted through solidification. Examples of such a medium include sodium nitrate, potassium nitrate, calcium nitrate, sodium sulphate, potassium carbonate, etc. [36]. The thermochemical storage systems use a reversible chemical reaction as a method of storing heat. A relatively more complex compound is broken down into two or more simpler compounds by supplying heat for an endothermic reaction. The separated compounds are then stored until the time when the stored energy is required again. When the stored energy needs to be extracted, the separated compounds are allowed to react again resulting in an exothermic reaction releasing the stored energy as heat. Examples of such a medium include metal hydrides, carbonates, hydroxides, etc. [37].

On the basis of arrangement, the thermal energy storage systems can be divided into active and passive systems [34]. The active storage systems are those where the storage medium 'flows' in the plant. The active systems could further be classified as active direct or active indirect systems. In the active direct systems, the heat transfer fluid in the solar receiver is also used as the storage medium, whereas in the active indirect systems, the heat transfer fluid in the solar receiver is different from the storage medium.

An example of the active direct system is a molten salt central receiver solar field with a two-tank molten salt storage, as shown in Figure 2.11. Similarly, an example of the active indirect system is a parabolic trough solar field with thermal oil as the heat transfer fluid,

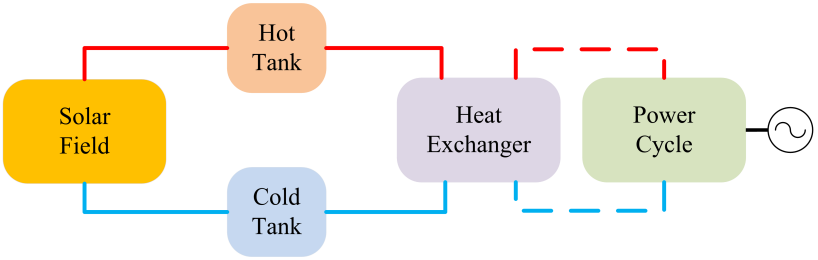

Figure 2.11: Active direct thermal energy storage system.

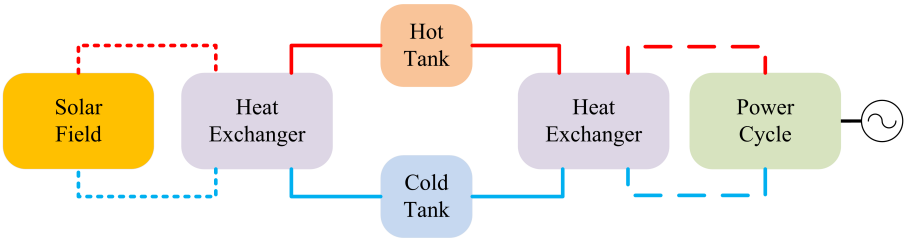

Figure 2.12: Active indirect thermal energy storage system.

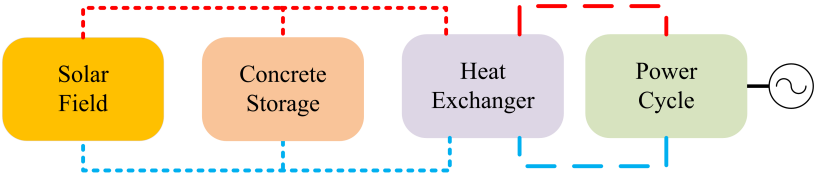

Figure 2.13: Passive thermal energy storage system.

but molten salt as the storage medium in a two-tank arrangement, as shown in Figure 2.12. In a passive storage system, the storage medium remains stationary, i.e. it does not 'flow'. An example of such an arrangement is a concrete based solid storage which gets charged or discharged by the heat transfer fluid from the solar field, as shown in Figure 2.13. In the figures, the solid lines (——) represent molten salt, the dashed lines (– – –) represent the power cycle working fluid, and the dotted lines (·····) represent thermal oil. The 'red' lines represent hot fluid and the 'blue' lines represent the cold fluid.

2.5 Power cycles

All the contemporary large-scale commercial CSP plants operate with the conventional steam Rankine cycle [39]. A typical CSP plant layout is shown in Figure 2.14. It includes a parabolic trough solar field, a two-tank molten salt thermal energy storage system (active indirect), and a steam Rankine cycle . The steam Rankine cycle is with reheat and regeneration, and

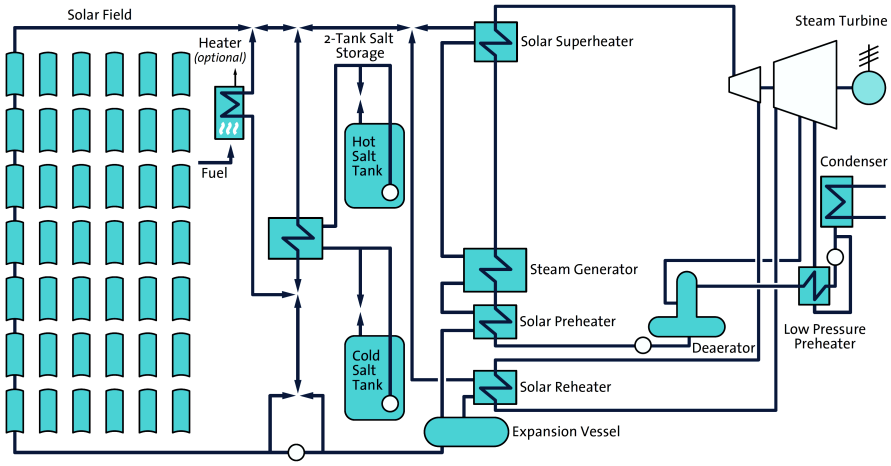

Figure 2.14: Parabolic trough CSP plant with a two-tank active direct molten salt storage system and a steam Rankine cycle [13].

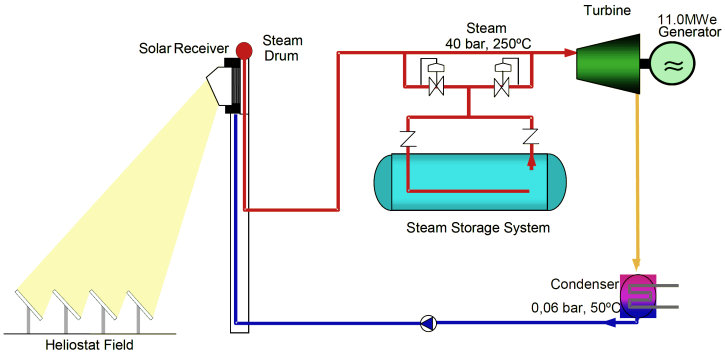

Figure 2.15: Central receiver CSP plant with direct steam generation [38].

the heat is supplied to the cycle in a boiler and a reheater. Another configuration with a steam Rankine cycle with direct steam generation is shown in Figure 2.15. In this configuration, the steam is generated directly in the solar receiver using the heat input from the concentrated solar radiation. A buffer steam storage tank is also a part of this plant to continue the plant operation for brief periods in situations like cloud passage.

Other power cycles and several configurations to incorporate a solar field with existing fossil fuel based power plants to reduce the fuel consumption have also been recently proposed for CSP plants. For example, a combined cycle power plant with a gas turbine and a steam Rankine cycle is shown in Figure 2.16. In this configuration the compressed air passes through a pressurized volumetric receiver where it is heated through concentrated solar radiation before going trough the combustion chamber and the turbine. The exhaust

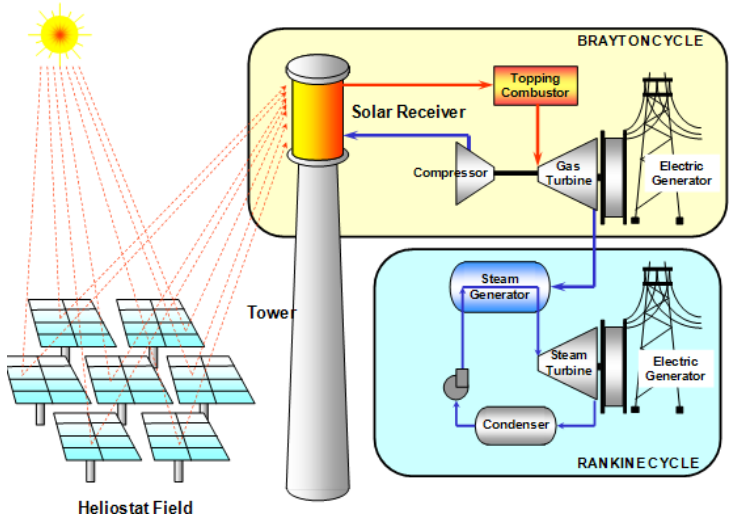

Figure 2.16: Central receiver CSP plant with a combined cycle [40].

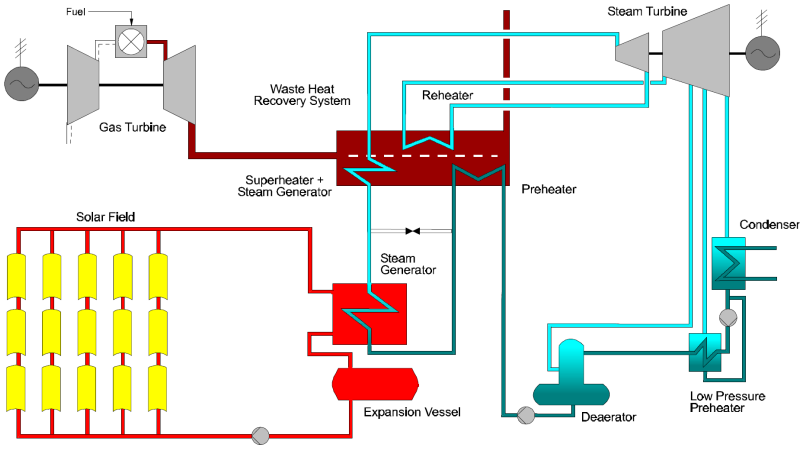

Figure 2.17: Integrated solar combined cycle power plant [41].

from the gas turbine is then used to operate a bottoming steam Rankine cycle. Similarly, an integrated solar combined cycle power plant is shown in Figure 2.17 where the solar field supplies a part of the required heat input to the bottoming cycle. Using the heat from the parabolic trough solar field, water is evaporated before being superheated by the gas turbine exhaust gases and entering the high pressure steam turbine. Novel cycles such as supercritical carbon dioxide Brayton cycle [42], and receivers such as falling film receivers have also been recently investigated for use with CSP plants [30]. In this study, the focus is on the use of a Kalina cycle in a CSP plant.

3

KALINA CYCLE

This chapter presents an overview of the Kalina cycle for both low and high temperature applications. The methods used to estimate the thermodynamic and transport properties of the ammonia-water mixtures are also presented.

3.1 Fluid mixtures

Fluid mixtures have been widely studied for their use in refrigeration systems and heat pumps [43]. These include mixtures of natural as well as artificial refrigerants, and could either be azeotropic or zeotropic. A mixture for which there is at least one combination of temperature and pressure where the mass fractions of the liquid and vapour phases are the same is referred to as an azeotropic mixture [43]. The state where this happens is called the azeotropic point. This point is highlighted in Figure 3.1a for a binary azeotropic mixture with the azeotropic point boiling temperature lower than the boiling temperatures of the pure fluid components.

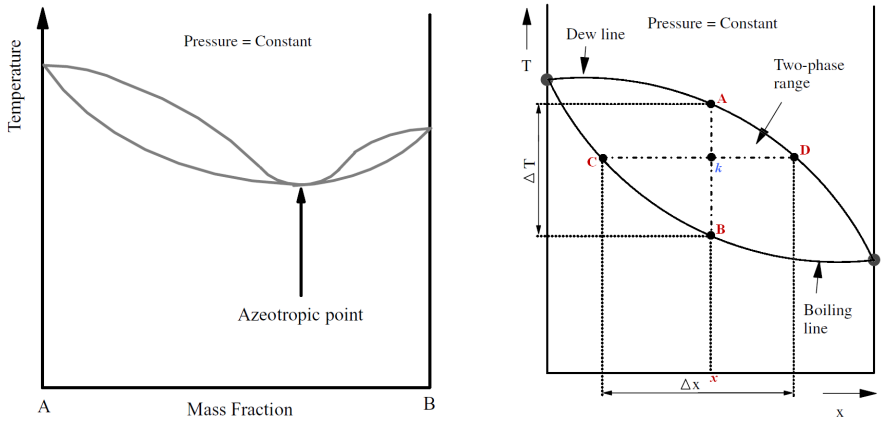

(a) Binary azeotropic mixture.

(b) Binary zeotropic mixture.

Figure 3.1: Temperature-composition diagram at a constant pressure [43].

For a zeotropic mixture, on the other hand, the mass fraction of the liquid and vapour phases are always different in phase equilibrium. The temperature-composition diagram for a binary zeotropic mixture is shown in Figure 3.1b. In the figure, for any bulk composition 'x' at a state 'k' in the two-phase region, the points 'A' and 'B' represent respectively the dew point and the bubble point temperatures for the mixture. The points 'C' and 'D' represent respectively the liquid and the vapour saturation points for the equilibrium liquid and vapour phase compositions. The temperature difference 'ΔT' on the vertical axis of the curve represents the *temperature glide* for the mixture, i.e. the difference between the bubble and the dew point temperatures for a particular mixture composition. The composition here could either be the mole or the mass fraction with respect of one of the components.

In recent years, the use of fluid mixtures in power cycles has attracted increased interest because of the possibility to reduce the irreversibility during a heat transfer process. Most of these studies have focused on the use of organic Rankine cycles for low temperature systems such as industrial waste heat recovery, geothermal power plants, and low temperature solar power. The non-isothermal evaporation and condensation with zeotropic mixtures present the potential to increase the exergy efficiency of the power cycle by matching the temperature profiles of the working fluid during evaporation and condensation to those of the hot source and the cooling source, respectively. However, maximizing the exergy efficiency does not automatically result in economic gains since it might mean using larger heat exchangers, very high turbine rotational speeds, and more expensive components such as electromagnetic bearings [44].

Braimakis et al. [44] compared several natural refrigerants and their mixtures for use in organic Rankine cycles with heat source temperatures between 150 °C and 300 °C. The comparison included both subcritical and supercritical operation of the power cycle. The results suggest that it is possible to obtain different pure fluids, zeotropic mixtures, or different compositions of zeotropic mixtures resulting in the maximum exergy efficiency for the power cycle for different types and temperatures of the heat source. At the same time, the overall cycle exergy efficiency is also dependent on how well the cooling source in the condenser matches with the condensation temperature glide. Therefore, it is necessary to compare the use of pure fluids and mixtures based on the temperature of the heating and the cooling sources on a case by case basis in order to be certain about both the thermodynamic and economic superiority of any option. The use of the supercritical organic Rankine cycles was found to be justifiable only when the critical temperature of the working fluid was significantly lower than the temperature of the heat source.

Angelino and Colonna Di Paliano [45] presented the merits of using fluid mixtures in organic Rankine cycles. The non-isothermal phase change at both high and low temperatures was indicated as the main advantage over pure fluids. Siloxane mixtures and hydrocarbon mixtures were respectively studied for heat recovery and geothermal applications. Chys

et al. [46] examined the effect of using mixtures in an organic Rankine cycle with heat sources at 150 °C and 250 °C. The use of binary mixtures resulted in a 15.7 % increase in the cycle efficiency and a 12.3 % increase in the electricity generation for the heat source temperature of 150 °C. A 6 % efficiency increase and a 5.5 % electricity generation increase was observed for the heat source temperature of 250 °C. The publication also highlighted leakage and additional costs as disadvantages when using fluid mixtures instead of pure fluids in a power cycle.

Heberle et al. [47] investigated the use of zeotropic mixtures of isobutane and isopentane, and R227ea and R245fa, as working fluids in organic Rankine cycles for low enthalpy geothermal resources. Heat source temperatures between 80 °C and 180 °C were analysed. The results suggested that the non-isothermal phase change with mixtures lead to an efficiency increase when compared with using pure fluids. It was also concluded that the mixture compositions, where the condensation temperature glide matched with the temperature profile of the condenser cooling water, were the most efficient. Among the considered cases, the R227ea-R245fa mixtures resulted in higher efficiencies as compared with the isobutane-isopentane mixtures except for the heat source temperature of 180 °C. Andreasen et al. [48] presented a generic methodology for the optimization of the organic Rankine cycle with a heat source temperature of 90 °C and 120 °C. Both pure and mixed fluids were compared and the results suggested that the mixed working fluids increased the net power output from the cycle while reducing the pressure levels.

Weith et al. [49] analysed the performance of siloxane mixtures for waste heat recovery from a biogas plant both numerically and experimentally. One of the key disadvantages of using a fluid mixture in a power cycle is the degradation of the heat transfer coefficients as compared with the pure fluids, resulting in an increase in the required heat transfer areas. The publication mentioned degradations of up to 46 % as compared with the ideal values (i.e. the values from linear interpolation for the pure components). With mixtures, a higher efficiency increase was observed for combined heat and power application than for only electricity generation. Heberle and Brüggemann [50] presented a thermoeconomic evaluation of organic Rankine cycles for geothermal power generation using zeotropic mixtures as the working fluid. The primary objective of the study was to assess if the efficiency increase by using mixtures is sufficient to compensate for the additional costs of the plant components. Heat source temperatures between 100 °C and 180 °C were evaluated. The results suggest that the electricity generation costs for geothermal organic Rankine cycles could be decreased by using zeotropic mixtures as working fluids.

The use of fluid mixtures for high temperature power cycles (in 350-550 °C range) has only been studied for the ammonia-water mixtures for the Kalina cycle as most of the other compounds dissociate at such high temperatures. The methods to estimate the fluid properties along with other relevant information for the ammonia-water mixtures are presented below.

3.2 Ammonia-water mixture

The ammonia-water mixture has been used in absorption chillers and heat pumps for a long time. In power generation applications, the ammonia-water mixtures are used as the working fluid for the Kalina cycle. One of the main advantages of using an ammonia-water mixture as the power cycle working fluid is that ammonia and water have similar molar masses. This enables using similar equipment for the Kalina cycle as has been conventionally used for the steam Rankine cycle [51]. The key properties for ammonia and water are given in Table 3.1. In order to evaluate the thermoeconomic performance of a power cycle with ammonia-water mixtures as the working fluid, it is necessary to estimate the thermophysical properties of the mixture. These are the thermodynamic properties such as temperature, pressure, specific enthalpy, specific entropy, density, and specific heat capacity, and transport properties such as viscosity and thermal conductivity.

Table 3.1: Key properties for ammonia and water.

Property	Ammonia	Water
Chemical formula	NH_3	H_2O
Molar mass	17.0305 g mol^{-1}	18.0153 g mol^{-1}
Boiling point at atmospheric pressure	–33.33 °C	100 °C
Freezing point at atmospheric pressure	–77.73 °C	0 °C
Autoignition temperature	651 °C	-
Critical temperature	132.4 °C	373.9 °C
Critical pressure	113.33 bar	220.64 bar

3.2.1 Thermodynamic properties

The thermodynamic properties for ammonia-water mixtures define the thermodynamic state of the mixture. In order to calculate the thermodynamic properties of ammonia-water mixtures, more than 40 correlations have been developed so far [51]. These include cubic equations of state, virial equations of state, Gibbs excess energy formulations, corresponding states method, perturbation theory, group contribution theory, Leung-Griffiths model, Helmholtz free energy formulation, and polynomial functions. Detailed reviews of the different methods are provided by Thorin [52], Zhang et al. [51], and Mao et al. [53]. For numerical modelling of the Kalina cycle, the thermodynamic properties of the ammonia-water mixtures could be obtained from either developing an in-house function using one of the methods mentioned above, or from one of the following established software: using REFPROP with MATLAB [54], or using the in-built 'NH3H2O' function in EES [55].

Developing an in-house code to calculate the thermodynamic properties is a time consuming task and requires a good knowledge of the property relations for a stable and robust code. Therefore, it was decided to use one of the established software. The outputs from REFPROP with different formulations and from EES using the Ibrahim-Klein equation of state are

presented in Appendix A. The plots presented in the Appendix A compare the different methods with respect to the density, the specific enthalpy, and the specific entropy of the ammonia-water mixtures at different combinations of pressures (between 1 bar and 160 bar), temperatures (between 300 K and 800 K), and ammonia mass fractions (between 0.3 and 0.9). The compared methods are:

1. REFPROP with MATLAB with the default Tillner-Roth and Friend formulation for ammonia-water mixtures [56].
2. REFPROP with MATLAB with the Peng-Robinson equation of state [57].
3. REFPROP with MATLAB with the 'Ammonia (Lemmon)' formulation [58] to be used in calculation of properties for ammonia-water mixtures.
4. REFPROP with MATLAB with the 'Ammonia (Lemmon)' formulation to be used in calculation of properties for ammonia-water mixtures using the Peng-Robinson equation of state.
5. Ibrahim-Klein equation of state with EES using the in-built 'NH3H2O' function. The data from the EES property calculations was obtained from a colleague [59].

Even though the calculation of the properties using the Tillner-Roth and Friend formulation is the default option with REFPROP, it failed to converge on several occasions, particularly in the two-phase region, for high ammonia mass fractions, and near critical point. It was also found to be computationally more intensive than the alternatives. The calculations using the Peng-Robinson equation of state with REFPROP were slightly faster than the Tillner-Roth and Friend formulation but with very different density values in the liquid regions at high pressures. This is highlighted, for example, in Figures A.2 and A.23. In contrast, the 'Ammonia (Lemmon)' formulation was found to be more stable and with few convergence failures, without significantly compromising on the accuracy of the calculations as compared with the Tillner-Roth and Friend formulation. The specific enthalpy and the specific entropy values for about 2400 combinations of pressures, temperatures, and ammonia mass fractions were compared for the two methods. The maximum and the average deviations of the 'Ammonia (Lemmon)' formulation from the Tillner-Roth and Friend formulation for the specific enthalpy values were respectively 6.97 % and 1 %, while for the specific entropy values were respectively 4.49 % and 0.65 % [60]. When using EES, the values of density were found to be close to those from the Tillner-Roth and Friend formulation, but the values of specific enthalpy and specific entropy, while following a similar trend, were quite different. Therefore, the 'Ammonia (Lemmon)' formulation with REFPROP was used to calculate the thermodynamic properties of ammonia-water mixtures in this thesis. In order to be able to use the 'Ammonia (Lemmon)' formulation, at least REFPROP 9.1 is required. Along with this, the AMMONIAL.FLD fluid file [58], and the REFPROPM.M and RP_PROTO.M functions [54] are required for use with the 32-bit version of MATLAB. For 64-bit versions, the necessary files are available on the REFPROP website [54].

The critical temperature (T_{crit}) in K and the critical pressure (p_{crit}) in bar for the ammonia-water mixture were estimated using the ammonia mole fraction (y) in the following correlations by M. Conde Engineering [61]:

$$T_{crit} = 647.14 - 199.822371 \cdot y + 109.035522 \cdot y^2 - 239.626217 \cdot y^3 + 88.689691 \cdot y^4 \quad (3.1)$$

$$p_{crit} = 220.64 - 37.923795 \cdot y + 36.424739 \cdot y^2 - 41.851597 \cdot y^3 - 63.805617 \cdot y^4 \quad (3.2)$$

where the ammonia mole fraction (y) is related to the ammonia mass fraction (x) as follows:

$$y = \frac{[x/M_{amm}]}{[x/M_{amm}] + [(1-x)/M_{wat}]} \quad (3.3)$$

where M_{amm} and M_{wat} are the molar masses of ammonia and water, respectively. The critical temperature and pressure equations were validated in M. Conde Engineering [61] using the experimental data from Sassen et al. [62].

3.2.2 Transport properties

The transport properties for the ammonia-water mixtures are necessary for heat exchanger design and the estimation of the heat transfer areas. Very little experimental data is available for transport properties of ammonia-water mixtures. There are some correlations available for predicting mixture transport properties (Reid et al. [63], as mentioned in Thorin [64]), but none developed particularly for the polar ammonia-water mixtures [52]. Historically, the correlations by Stecco and Desideri and El-Sayed have been used to evaluate the transport properties of ammonia-water mixtures [52,64]. A set of correlations for estimating the transport properties is given by Nordtvedt [65], but the use was limited to pressures and temperatures up to 19 bar and 160 °C. Another set of correlations is provided by M. Conde Engineering [61], but again limited to low temperatures and pressures.

A detailed review of the different transport property estimation methods for ammonia-water mixtures is provided by Kærn et al. [66]. The different methods are compared at various temperatures and pressures. The effect of using the different correlations on the boiler area is also presented for two cases – a flue gas based boiler for a gas turbine bottoming Kalina cycle and an oil based boiler for a parabolic trough CSP plant with a Kalina cycle. The results suggest that all possible combinations for the various transport property estimation methods resulted in a maximum 4.3 % deviation in the heat exchanger area for the flue gas based boiler, and a maximum 12.3 % deviation for the oil based boiler.

In the current study, the correlations by El-Sayed [67] as reported in Thorin [64] were used for the estimation of the ammonia-water mixture transport properties. The correlations are presented in Appendix B.

3.2.3 Safety precautions

The use of ammonia-water mixtures requires some additional measures when it comes to the safety of the personnel. Ammonia is toxic in nature and causes irritation when it gets in contact with the human body. It can also be lethal in high doses. From the safety perspective, it is important to have adequate ventilation in place so as to vent out the hazardous ammonia vapour in case of a leakage. Since ammonia vapour has a distinct pungent odour and is lighter than air, it is easy to detect and rises up naturally. For designing the ammonia-water power plants, the experience from the ammonia synthesis industry, fertilizer industry, and the absorption industry can be used [52].

The feasibility of using ammonia-water mixtures at high temperatures has been questioned due to the nitridation effect resulting in the corrosion of the equipment [51]. However, the use of an ammonia-water mixture as the working fluid at high temperature has been successfully demonstrated in the Canoga Park demonstration plant with a turbine inlet temperature and pressure of 515 °C and 110 bar [68]. Moreover, a patent by Kalina [69] claims the stability of ammonia-water mixtures along with prevention of nitridation for plant operation preferably up to 1093 °C for temperature and 689.5 bar for pressure using suitable additives. Water itself prevents the ammonia in the mixture from corroding the equipment up to about 400 °C, and above this temperature, the amount of the additive is far below the threshold for it to cause any damage [70]. Lastly, it is advised to avoid copper and copper alloys because of potential corrosion problems [71]. Other than this, there is no particular restriction in using ammonia-water mixtures with the conventional equipment.

3.3 Power cycle

The Kalina cycle was introduced in 1984 [15] as an alternative to the conventional steam Rankine cycle. The power cycle was based on the principles of ammonia-water absorption refrigeration systems. It was proposed to be used as a bottoming cycle for combined cycle power plants with a mixture of ammonia and water as its working fluid, instead of pure water as in the case of a steam Rankine cycle. The composition of the ammonia-water mixture could be varied by changing the *ammonia mass fraction* which is defined as the ratio of the mass of ammonia in the mixture to the total mass of the mixture. Kalina and Leibowitz [72] presented a conceptual flow diagram for using Kalina cycle as a bottoming cycle for a utility combined cycle power plant. Additional off-design benefits were also presented for situations when the condenser cooling water temperature went below a certain temperature, for which it would not be possible to reduce the condenser pressure for a steam Rankine cycle any further. It was also mentioned that since the molar masses of ammonia and water are nearly equal, the aerodynamic correlations based on the Mach number are equivalent. Therefore similar turbine designs as in the conventional steam

Rankine cycles could be used for the Kalina cycles as well. Finally, since the turbine outlet pressures of the Kalina cycle are usually above atmospheric pressure, the condenser need not operate in vacuum, and the turbine sizes were much smaller than the steam turbines for similar power outputs (because of a much smaller volumetric flow rate at the turbine outlet). Kalina and Leibowitz [73] presented a detailed discussion on the system design and experimental development of the Kalina cycle technology. The various cycle components were discussed on the basis of the similarity and differences from the off-the-shelf available equipment for a steam Rankine cycle. Kalina and Leibowitz [74] presented the design of a 3 MW Kalina cycle demonstration plant. Based on single pressure designs at comparable peak cycle temperatures, the Kalina cycle was expected to have a 25 % more output than a steam Rankine cycle. Kalina et al. [75] elaborated on the design aspects of the key Kalina cycle equipment such as the turbine and the heat recovery vapour generator. A cost analysis was presented based on the purchased equipment cost for both the Kalina and the steam Rankine cycles. The Kalina cycle layout KCS6 was used for comparison. It was concluded that even though the purchasing cost of the Kalina cycle was slightly higher than the steam Rankine cycle, the incremental power generation easily compensates for the added cost over the plant lifetime. In a two-part article, Kalina and Tribus [76,77] presented the advances made in the Kalina cycle technology between the years 1980 and 1991. The topics in the papers ranged from a general description of the various categories of irreversibility in the power plant and how can it be reduced, to an update on the various Kalina cycle layouts and uses. Exemplary cycle characteristics of the KCS6 Kalina cycle system were also provided.

Zervos [78] presented a preliminary design and the economic aspects of a 100 MW coal-fired Kalina cycle power plant. It was reiterated in this paper that none of the Kalina cycle equipment required any significant modifications in the state-of-the-art for design, materials, or fabrication. For the regenerative heat transfer network, the conventional shell-and-tube type heat exchangers could be used. Zervos et al. [79] presented the start-up and operational experience of the 3 MW Kalina cycle demonstration plant. Smith et al. [80] presented the Kalina cycle performance and operability characteristics for a combined cycle power plant. The advantages of using a Kalina cycle during start-up, shut-down, and part-load operation over the conventional steam Rankine cycle were mentioned. These included the above atmospheric pressure operation in all components of the power cycle, use of a single-pressure, once-through heat recovery vapour generator, and less degradation of the Kalina cycle performance at part-load conditions. The steps for start-up and shut-down of the Kalina cycle system were elaborated in detail. It was highlighted that the Kalina cycle is particularly well suited for unattended operation and sub-freezing ambient conditions.

Since the introduction of the Kalina cycle as a bottoming cycle for gas turbine combined cycle power plants, several other uses for the cycle have been proposed, primarily for low grade heat to power conversion applications. Ogriseck [81] presented the possibility of the integration of a Kalina cycle in a combined heat and power plant. The net efficiency of the

plant was calculated for different cooling water temperatures and basic solution ammonia mass fractions. Bombarda et al. [82] presented a thermodynamic comparison between the Kalina cycle and an organic Rankine cycle for heat recovery from the exhaust of a diesel engine. The publication concluded that although the obtained electrical power outputs are nearly equal, the Kalina cycle requires a much higher turbine inlet pressure to attain the similar output, thereby making it unjustified for such use. Singh and Kaushik [83] presented the energy and exergy analyses and optimization of a Kalina cycle coupled with a coal-fired steam power plant for exhaust heat recovery. The results suggest that an ammonia mass fraction of 0.8 gives the maximum cycle efficiency at a turbine inlet pressure of 40 bar. Coskun et al. [84] presented a comparison between different power cycles for a medium temperature geothermal resource. It was concluded that the Kalina cycle and the double flash cycle provided the least LCOE and the shortest payback periods. Wang et al. [85] presented a parametric analysis and optimization of a Kalina cycle driven by solar energy. The results suggest that the net power output and the system efficiency are less sensitive to the turbine inlet temperature under given conditions, and that there exists an optimal turbine inlet pressure which results in maximum net power output.

Sun et al. [86] presented an energy-exergy analysis and parameter design optimization for a Kalina cycle with an auxiliary superheater for a low grade thermal energy conversion system using solar energy as heat input. Larsen et al. [87] presented the optimization and a simplified cost analysis of the Kalina split-cycle using genetic algorithm (GA) in MATLAB with primary focus on the boiler, the turbine, and the mixing subsystem of the cycle. The publication also compared the performance of the Kalina split-cycle to that of a normal Kalina cycle. Nguyen et al. [88] conducted an exergy analysis of the Kalina split-cycle. The two studies [87,88] concluded that the Kalina split-cycle with reheat was thermodynamically better than the normal Kalina cycle but this improvement came at the price of increased initial cost and a more complex cycle design. Other recent studies on the low temperature Kalina cycle applications include their use in waste heat recovery [89–91], for exhaust heat recovery in a gas turbine modular helium reactor [92], in combined heat and power plants [93], as a part of Brayton-Rankine-Kalina triple cycle [94], and in solar power plants [85].

For high temperature applications, fewer studies have been conducted as compared with the low temperature applications. All of these studies however suggest potential thermodynamic benefits of using the Kalina cycle, thus motivating further research. The high temperature Kalina cycles have been investigated to be used as gas turbine bottoming cycles [95–98], for industrial waste heat recovery, biomass based cogeneration, and gas engine waste heat recovery [52], for direct-fired cogeneration applications [99], and in CSP plants [60,100–104]. Marston [95] presented the parametric analysis of a Kalina cycle to serve as a bottoming cycle for a gas turbine. Marston and Hyre [96] compared the performance of a triple-pressure steam cycle and a Kalina cycle as a gas turbine bottoming cycle. The publication concluded that the Kalina cycle is more efficient. Ibrahim and Kovach [97] studied the effect of varying

the ammonia mass fraction and the separator temperature on the cycle efficiency for a Kalina bottoming cycle using gas turbine exhaust as the heat source. The results suggest that the Kalina cycle is 10-20 % more efficient than the Rankine cycle with the same boundary conditions. Nag and Gupta [98] performed an exergy analysis of a Kalina cycle with gas turbine exhaust as the heat source. The publication concluded that the important parameters affecting the cycle efficiency are the turbine inlet temperature and composition, and the separator temperature. Thorin [52] presented the analysis of a Kalina cycle to be used for industrial waste heat recovery, biomass based cogeneration, and gas engine waste heat recovery. Various methods for calculating the thermophysical properties of the ammonia-water mixture were also presented.

From the experimental perspective, very little information was found in the open literature on ammonia-water power cycles, and whatever was found was for low temperature applications. Amano et al. [105] presented the experimental results for a Kalina cycle with steam as the heat source. The layout used two vapour-liquid separators and the turbine was directly connected to rich vapour outlet of one of the separators. It was suggested that the evaporating pressure be as low as possible to obtain a high enthalpy at the turbine inlet. Takeshita et al. [106] presented the results from the continuation of the above experiment. The experimental results for a turbine inlet ammonia mole fraction between 0.4 and 0.7 were presented. A horizontal shell-and-tube heat exchanger was used as the evaporator. The publication concluded that the characteristics of the turbine were mainly determined by the turbine outlet volumetric flow rate irrespective of the basic composition. Amano et al. [107] found that the turbine power output oscillated severely when the turbine inlet ammonia mass fraction was varied simultaneously with the evaporation pressure and the oscillations were observed for several hours. The oscillations were experienced because of the changes in the fluid specific volume with changes in ammonia mass fraction. Takeshita et al. [108] highlighted the advantages of a combined ammonia-water power and absorption refrigeration cycle. The results indicate that the ammonia-water power cycle consume less steam (heat source) than the steam Rankine cycle for similar output. More recently, Yuan et al. [109] presented an experimental analysis of an ammonia-water power cycle for ocean thermal energy conversion application. The heat source temperature was between 30 °C and 40 °C, and the cooling source temperature was between 5 °C and 15 °C. The results suggest that the heating source temperature affects the cycle efficiency most significantly, then the cooling source temperature, while the solution flow rate has the least impact. Mirolli [68] lists the various plants, both past and current, operating with the Kalina cycle around the world.

3.3.1 Layouts

For the Kalina cycle, several configurations have been proposed depending on the end use. One of the simplest configurations, termed as KCS34 [51], is shown in Figure 3.2. It consists of a turbine (TUR), a generator (GEN), a low temperature recuperator (LT-RE), a high

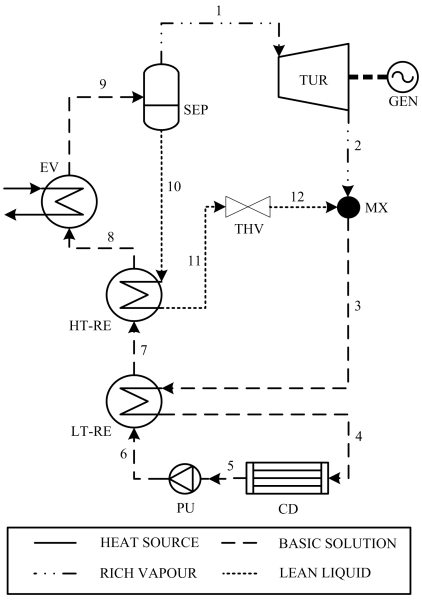

Figure 3.2: Kalina cycle KCS34 for low temperature applications.

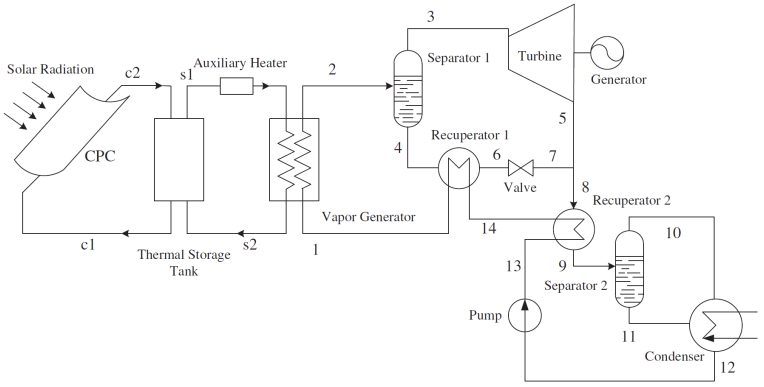

Figure 3.3: Low temperature Kalina cycle with two separators [85].

temperature recuperator (HT-RE), a condenser (CD), a pump (PU), a separator (SEP), a throttle valve (THV), a mixer (MX), and an evaporator (EV) with an external heat source which could be a waste heat stream, geothermal brine, etc. This configuration is used for low temperature applications and the ammonia rich vapour from the separator outlet is directly fed to the turbine. This configuration was used in the Húsavik geothermal power plant in Iceland and was also proposed as a bottoming cycle to the steam Rankine cycle for a parabolic trough CSP plant by Mittelman and Epstein [110].

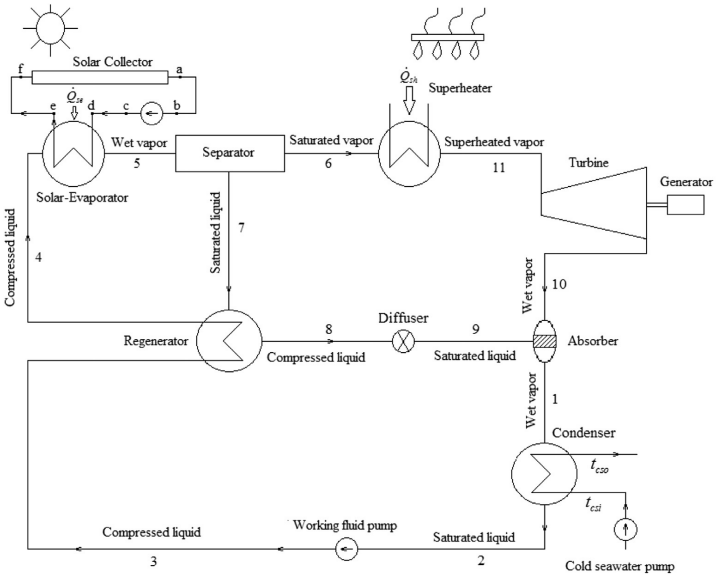

Figure 3.4: Kalina cycle driven by low temperature solar energy [86].

Few modifications to the KCS34 layout lead to other configurations suitable for low temperature solar applications (Figures 3.3 and 3.4). In Figure 3.3, the power plant consists of solar collectors, a thermal energy storage tank, an auxiliary heater, and the Kalina cycle with two separators. The solar radiation is collected using compound parabolic collectors with a solar field outlet temperature equal to 132 °C. In this layout it is thermodynamically not necessary to have two separators as the separated stream is mixed again in the condenser. The second separator is used mainly because of practical reasons, i.e. to separate the two phases and mix them just before the condenser in order to have a well-mixed fluid entering the condenser. In the configuration shown in Figure 3.4, the ammonia rich vapour stream from the separator enters the turbine, but after getting superheated from an external heat source. Several other similar low temperature configurations such as KCS1-2, KCS11, KCS34g, etc. can be found in the literature for various applications [51]. The Kalina cycle configurations for high temperature applications are inherently more complex than those used for the low temperature applications. Four high temperature Kalina cycle layouts for a central receiver CSP plant are shown in Figures 3.5 to 3.8. The different cycle layouts are named according to the positions of the various recuperators in the cycle. The Kalina cycle with two recuperators, termed KC12, is shown in Figure 3.5. Figures 3.6 and 3.7 show the two layouts with three recuperators each, but at different positions, and are respectively termed KC123 and KC234. The layout with four recuperators in the cycle, termed KC1234, is shown in Figure 3.8. All the layouts have four different ammonia mass fractions in the cycle represented by different types of lines: (1) the working solution, (2) the basic solution, (3) the rich vapour, and (4) the lean liquid.

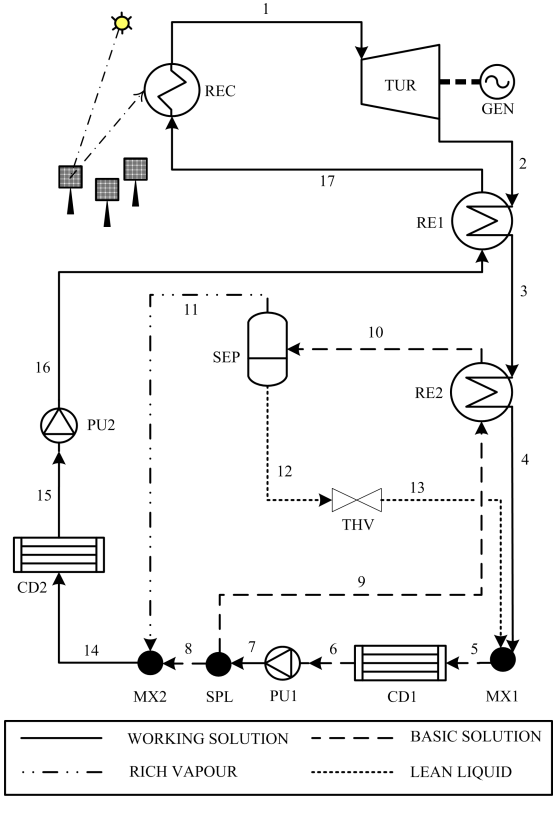

Figure 3.5: Kalina cycle KC12.

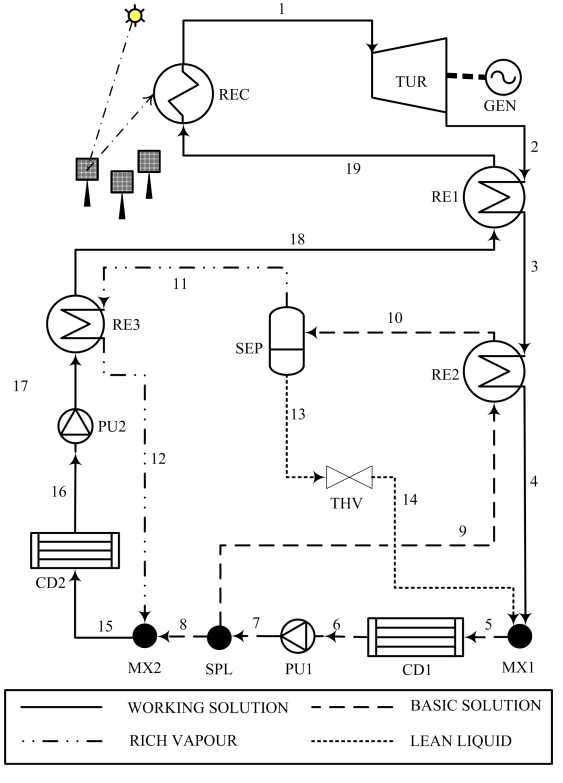

Figure 3.6: Kalina cycle KC123.

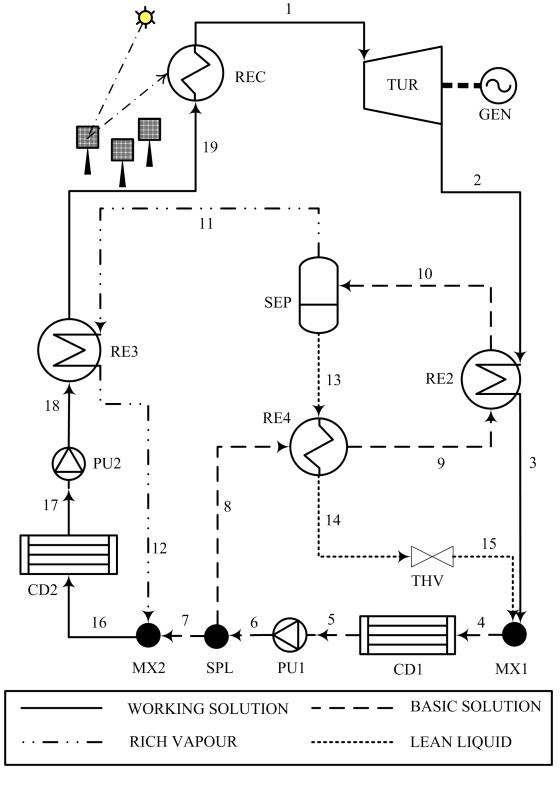

Figure 3.7: Kalina cycle KC234.

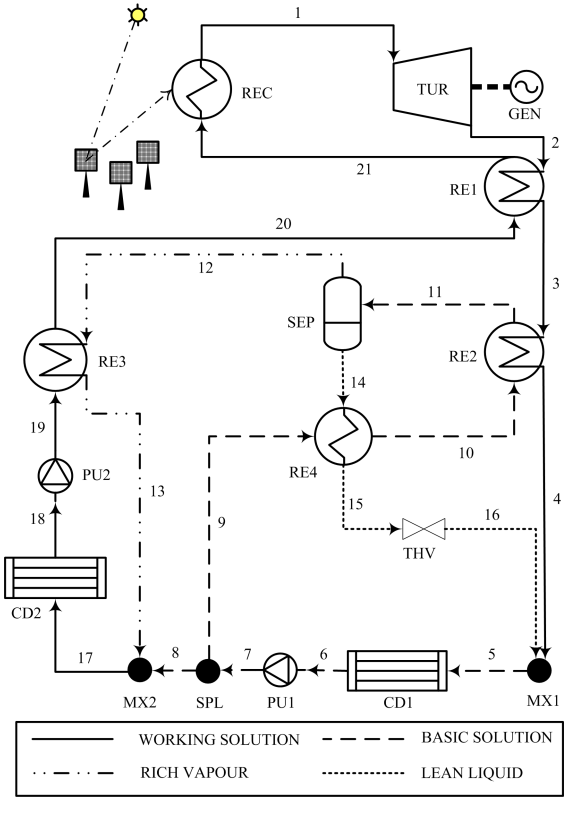

Figure 3.8: Kalina cycle KC1234.

The cycle components in the different layouts are represented in abbreviated forms where REC is the receiver/boiler, TUR is the turbine, GEN is the generator, SEP is the vapour-liquid separator, RE∗ is the recuperator, PU∗ is the pump, CD∗ is the condenser, MX∗ is the mixer (where '∗' denotes the respective component number), SPL is the splitter, and THV is the throttling valve. The layout KC234 was studied as the standard high temperature layout by Marston [95] and Nag and Gupta [98], while the layout KC12 was used in a preliminary analysis for a CSP plant by Modi and Haglind [100]. The remaining two layouts (KC123 and KC1234) were derived by adjusting the number and placement of the recuperators in the KC12 and the KC234 layouts. The Kalina cycle KC12 for a parabolic trough CSP plant is shown in Figure 3.9. Any of the high temperature Kalina cycle configurations may be modified by adding a boiler where the heat transfer fluid ('htf' in the figure) from the solar field delivers the energy to the working fluid of the power cycle. The boiler includes the superheater (SH), the evaporator (EV), and the economizer (EC).

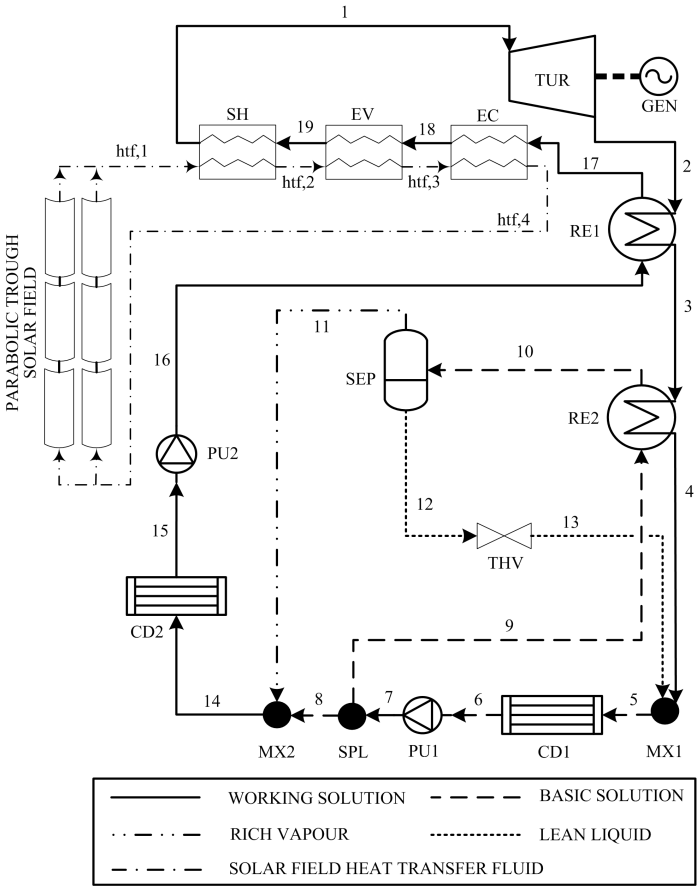

Figure 3.9: Kalina cycle KC12 for a parabolic trough CSP plant.

3.3.2 Operational considerations

The key difference between the Kalina cycle and the steam Rankine cycle is the use of ammonia-water mixture as the working fluid instead of pure water. Because of this, the cycle layout needs to be modified in order to fully exploit the benefits of using a mixture. Except for the number and the position of the recuperators, the different high temperature Kalina cycle configurations (Figures 3.5 to 3.9) work broadly in a similar manner. The superheated ammonia-water mixture (stream 1), i.e. the working solution, expands in the turbine and is subsequently mixed in the mixer MX1 with the ammonia lean liquid from the separator SEP to lower the ammonia mass fraction in the condenser CD1. The fluid after the mixer MX1 is called the basic solution. The ammonia rich vapour from the separator SEP is mixed in the mixer MX2 with a part of the basic solution from the splitter SPL in order to obtain the working solution ammonia mass fraction. This working solution then passes through the condenser CD2 and the pump PU2. The external heat input to the working fluid is provided in the receiver/boiler.

The ammonia-water mixture condenses at much higher pressures than steam at the same condenser cooling water conditions, e.g. a mixture with an ammonia mass fraction of 0.5 has a saturation liquid pressure of 3.46 bar at 25 °C whereas the same for pure water is 0.03 bar. Additionally, a higher ammonia mass fraction will result in a larger condensation pressure. It is for this reason that a distillation-condensation subsystem is introduced in the Kalina cycle. The distillation-condensation subsystem includes the separator SEP, the mixers MX1 and MX2, the splitter SPL, the throttle valve THV, the condenser CD1, and the pump PU1 along with the recuperators within this internal loop. In order to lower the condensation pressure so as to maximize the expansion in the turbine, the ammonia mass fraction in the condenser CD1 is reduced as compared with the turbine inlet ammonia mass fraction. This is done by mixing the working solution from the turbine TUR outlet with the lean liquid from the separator SEP. In order to do this, one of the key requirements is to have two-phase flow at the separator SEP inlet. The separator SEP then separates the vapour part of the two-phase stream from the liquid part.

Being a zeotropic mixture, the ammonia mass fraction of the vapour part at the separator SEP outlet is significantly higher than the ammonia mass fraction of the lean liquid. This is because the ammonia in the mixture starts to vaporize much before water due to its lower boiling point. This is the reason for the presence of a temperature glide during the evaporation or condensation of an ammonia-water mixture, as compared with pure water. This temperature glide could become as high as about 97 °C at a pressure of 10 bar as shown in Figure 3.10 (at an ammonia mass fraction of 0.65). Once the two streams (liquid and vapour) are separated in the separator SEP, the lean liquid becomes a part of the fluid passing through the condenser CD1, whereas the rich vapour is mixed with a part of the basic solution in the mixer MX2 to obtain the working solution composition. The state of the

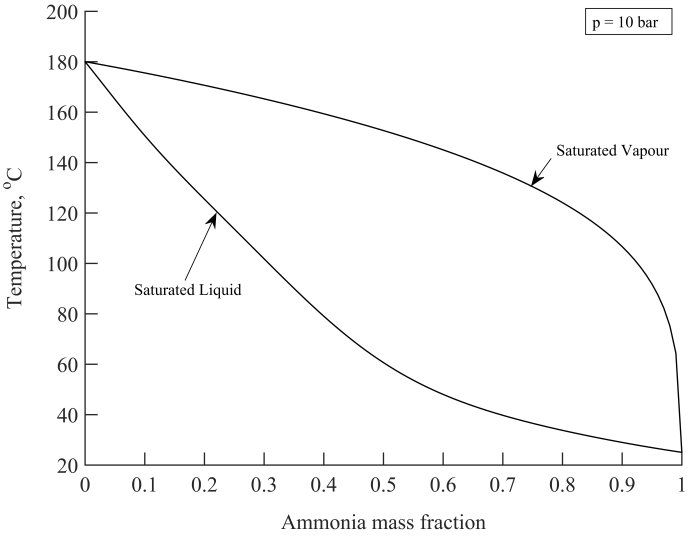

Figure 3.10: Ammonia-water mixture temperature-composition diagram at a pressure of 10 bar.

resulting stream after the mixing in the mixer MX2 (e.g. stream 14 in Figure 3.5) might be in the two-phase region. For a high temperature Kalina cycle with a turbine inlet temperature in the range of 350-550 °C, high turbine inlet pressures (80-140 bar) would most likely be used. This requirement is the primary reason for the additional condenser (CD2) and pump (PU2) so that the turbine inlet pressures could be raised to the required level. This is what makes the high temperature configurations more complex than the low temperature ones where the rich vapour stream could directly be fed to the turbine (as shown in Figure 3.2).

4

THERMODYNAMIC ANALYSIS

This chapter presents a general methodology to solve and optimize the Kalina cycle for high temperature applications. The solution algorithm is presented and explained for a central receiver CSP plant as a case study. The key results from the optimization are then presented and discussed along with the choice of one of the layouts for the detailed thermoeconomic optimization.

4.1 Cycle design

A general methodology to solve a Kalina cycle for high temperature applications is proposed and presented. The solution algorithm was used to find the design point operation state of the Kalina cycle for a set of given assumptions and bounds, and would later become a part of the optimization routine to maximize the thermodynamic efficiency (Section 4.2), or minimize the LCOE (Section 5.2). The Kalina cycle KC12 for a central receiver CSP plant (Figure 4.1) is used to explain the solution algorithm (Section 4.1.1) where the cycle is solved for the required net electrical power output at design condition. The same algorithm can also be used for other applications such as a bottoming cycle for a gas turbine, waste heat recovery, geothermal power plants, and other types of CSP plants with slight modifications. As an example relevant to the current study, the algorithm was extended to make it applicable for a parabolic trough CSP plant (Section 4.1.2). This was done by adding a boiler and a heat transfer fluid pump to the power block. The boiler section is where the heat transfer fluid from the parabolic trough solar field transfers energy to the power cycle working fluid. The algorithm for the central receiver CSP plant was then demonstrated for use with different Kalina cycle layouts to highlight the algorithm's flexibility (Section 4.1.3).

4.1.1 Solution algorithm

For solving the cycle to obtain the design condition, the cycle was modelled in steady state. All the models were implemented in MATLAB [16], and the thermodynamic properties of the ammonia-water mixtures were estimated using REFPROP [19]. The pressure drops and

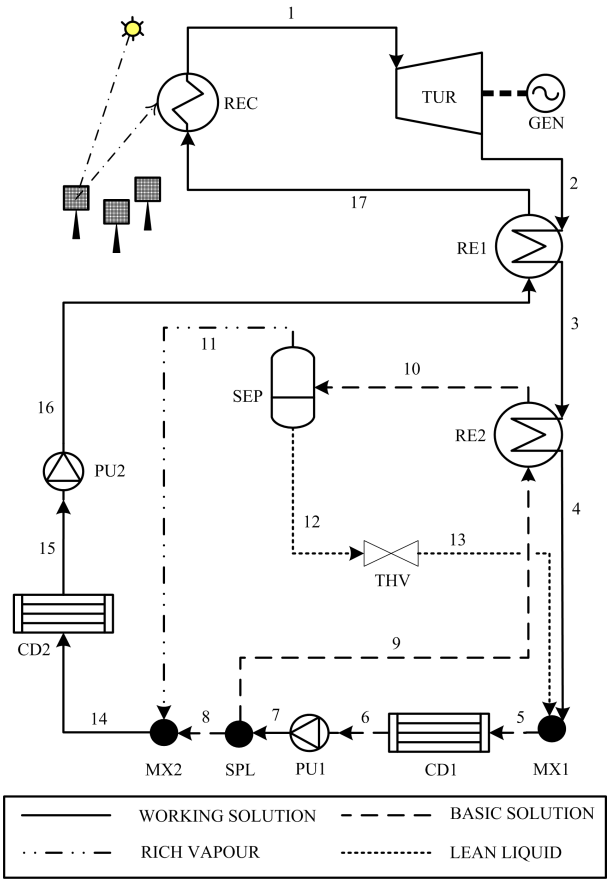

Figure 4.1: Kalina cycle KC12 for a central receiver CSP plant.

heat losses were neglected. The most important parameters in the Kalina cycle performance evaluation are the turbine inlet and outlet conditions, and the separator inlet conditions [51, 98]. Therefore in this study, the turbine outlet pressure, and the separator inlet temperature and ammonia mass fraction were selected as the decision variables (initial guess variables), while the pressure and the ammonia mass fraction at the turbine inlet were varied for parametric analysis.

For any given value of the turbine inlet pressure and ammonia mass fraction, the Kalina cycle KC12 (Figure 4.1) was solved for each iteration of the optimization process as shown in Figure 4.2.

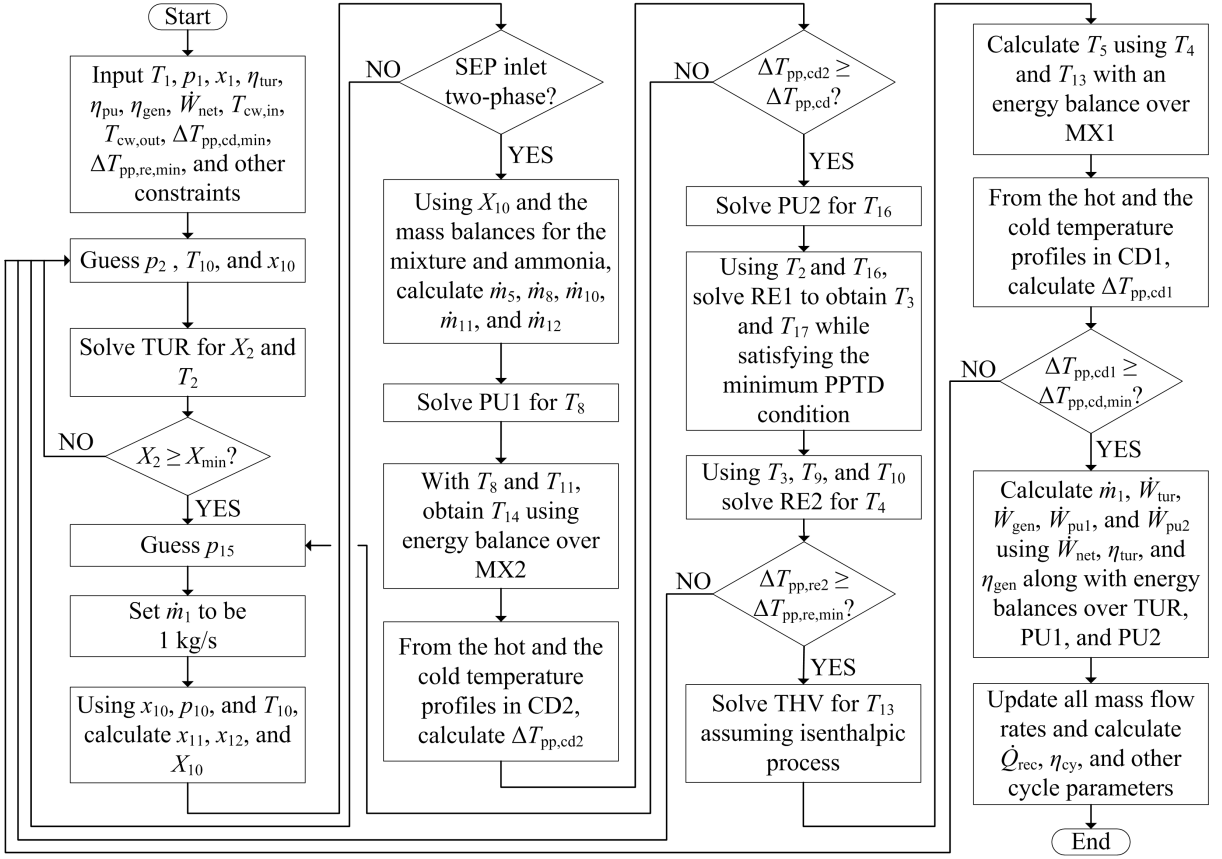

Figure 4.2: Solution algorithm for every iteration for the Kalina cycle KC12 for a central receiver CSP plant.

The turbine TUR was solved at the beginning using the assumed inlet conditions and isentropic efficiency to obtain the state at the turbine outlet. Then, assuming a condenser pressure for condenser CD2, the mass flow rates in the cycle were then obtained as suggested in Marston [95]. With respect to the mass flow rates at different points in the cycle, the entire cycle (Figure 4.1) can be represented in a simplified manner shown in Figure 4.3.

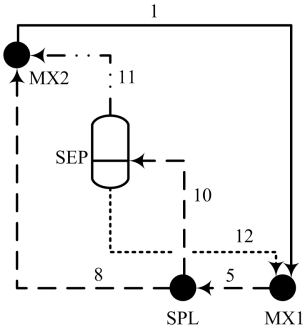

Figure 4.3: Different mass flow rates in the Kalina cycle KC12.

The equations relating the mass flow rates for the mixture and the quantity of ammonia in the mixture for the streams shown in Figure 4.3 are as follows:

$$\dot{m}_5 = \dot{m}_1 + \dot{m}_{12} \tag{4.1}$$

$$\dot{m}_5 \cdot x_5 = \dot{m}_1 \cdot x_1 + \dot{m}_{12} \cdot x_{12} \tag{4.2}$$

$$\dot{m}_1 = \dot{m}_8 + \dot{m}_{11} \tag{4.3}$$

$$\dot{m}_1 \cdot x_1 = \dot{m}_8 \cdot x_8 + \dot{m}_{11} \cdot x_{11} \tag{4.4}$$

$$\dot{m}_{10} = \dot{m}_{11} + \dot{m}_{12} \tag{4.5}$$

$$\dot{m}_{10} \cdot x_{10} = \dot{m}_{11} \cdot x_{11} + \dot{m}_{12} \cdot x_{12} \tag{4.6}$$

$$\dot{m}_{11} = \dot{m}_{10} \cdot X_{10} \tag{4.7}$$

$$x_5 = x_{10} \tag{4.8}$$

$$x_8 = x_{10} \tag{4.9}$$

where $\dot{m}$ is the mass flow rate, x is the ammonia mass fraction, and X is the vapour quality. The mass balances are over the mixer MX1 (Equations (4.1) and (4.2)), the mixer MX2 (Equations (4.3) and (4.4)), and the separator SEP (Equations (4.5) and (4.6)). The ammonia mass fraction balances are over the splitter SPL (Equations (4.8) and (4.9)). Since SEP is simply a vapour-liquid separator, Equation (4.9) only relates the mass flow rate of stream 11 to the mass flow rate and the vapour quality of the stream 10. On using Equations (4.3), (4.4), and (4.8), and Equations (4.1), (4.2), (4.5)-(4.7), and (4.9), the following relations were derived:

$$\frac{\dot{m}_{10}}{\dot{m}_1} = \frac{x_1 - x_{10}}{X_{10} \cdot (x_{11} - x_{10})} \tag{4.10}$$

$$\frac{\dot{m}_8}{\dot{m}_1} = \frac{x_{11} - x_1}{x_{11} - x_{10}} \tag{4.11}$$

These relations were then used to calculate the different mass flow rates after assuming $\dot{m}_1$ to be 1 $\mathrm{kg\,s^{-1}}$ as an initial guess value, and calculating the values of the ammonia mass fractions for the two outlet streams of the separator (x_{11} and x_{12}) with REFPROP using the state at the separator SEP inlet as input. This was done iteratively until the pinch point temperature difference (PPTD) in the condenser CD2 became greater than or equal to the minimum PPTD value for the condensers. Once the mass flow rates of the different streams were known, and it was ensured that the inlet stream to the separator SEP is in two-phase flow, then the pumps, the mixers, the recuperators, and the condensers were solved while satisfying all the design constraints such as minimum PPTD, minimum vapour quality at the turbine outlet, etc. using the following equations for the various cycle components:

TUR: $$\dot{W}_{\mathrm{tur}} = \dot{m}_1 \cdot (h_1 - h_2) \tag{4.12}$$

GEN: $$\dot{W}_{\mathrm{gen}} = \dot{W}_{\mathrm{tur}} \cdot \eta_{\mathrm{tur,m}} \cdot \eta_{\mathrm{gen}} \tag{4.13}$$

RE1: $$\dot{m}_2 \cdot (h_2 - h_3) = \dot{m}_{16} \cdot (h_{17} - h_{16}) \tag{4.14}$$

RE2: $$\dot{m}_3 \cdot (h_3 - h_4) = \dot{m}_9 \cdot (h_{10} - h_9) \tag{4.15}$$

CD1: $$\dot{m}_5 \cdot (h_5 - h_6) = \dot{m}_{\mathrm{cw,cd1}} \cdot c_{p,\mathrm{cw}} \cdot (T_{\mathrm{cw,out}} - T_{\mathrm{cw,in}}) \tag{4.16}$$

CD2: $$\dot{m}_{14} \cdot (h_{14} - h_{15}) = \dot{m}_{\mathrm{cw,cd2}} \cdot c_{p,\mathrm{cw}} \cdot (T_{\mathrm{cw,out}} - T_{\mathrm{cw,in}}) \tag{4.17}$$

PU1: $$\dot{W}_{\mathrm{pu1}} = \dot{m}_6 \cdot (h_7 - h_6) \tag{4.18}$$

PU2: $$\dot{W}_{\mathrm{pu2}} = \dot{m}_{15} \cdot (h_{16} - h_{15}) \tag{4.19}$$

SEP: $$\dot{m}_{10} \cdot h_{10} = \dot{m}_{11} \cdot h_{11} + \dot{m}_{12} \cdot h_{12} \tag{4.20}$$

MX1: $$\dot{m}_5 \cdot h_5 = \dot{m}_4 \cdot h_4 + \dot{m}_{13} \cdot h_{13} \tag{4.21}$$

MX2: $$\dot{m}_{14} \cdot h_{14} = \dot{m}_8 \cdot h_8 + \dot{m}_{11} \cdot h_{11} \tag{4.22}$$

SPL: $$h_8 = h_7 \tag{4.23}$$

SPL: $$h_9 = h_7 \tag{4.24}$$

THV: $$h_{12} = h_{13} \tag{4.25}$$

where $\dot{W}_{\mathrm{tur}}$ is the turbine power output, $\dot{W}_{\mathrm{pu}}$ is the required pump power, $\dot{W}_{\mathrm{gen}}$ is the generator electrical power output, $\dot{m}$ is the mass flow rate, h is the specific enthalpy, c_p is the isobaric specific heat capacity, and T is the temperature. The subscript 'cw' denotes the condenser cooling water. In addition, the equations for the turbine and pump isentropic efficiencies relating the efficiencies to the real and isentropic specific enthalpy differences over the respective components were also used. These are as follows:

$$\eta_{\text{tur,is}} = \Delta h_{\text{tur}} / \Delta h_{\text{tur,is}} \tag{4.26}$$

$$\eta_{\text{pu,is}} = \Delta h_{\text{pu,is}} / \Delta h_{\text{pu}} \tag{4.27}$$

It may be observed from Figure 4.2 that instead of using an overall logarithmic mean temperature difference (LMTD) value for the heat exchangers, a more general pinch point approach was used in order to ensure that there were no second law violations in the heat exchangers. All the recuperators and condensers were discretized into 50 control volumes on the basis of the heat transfer rate so that the position of the PPTD could be calculated with sufficient accuracy and that the heat exchanger temperature profiles could be generated for estimating the heat exchanger areas.

Most of the currently operational commercial CSP plants have a rated capacity in the range of 10 to 50 MW, e.g. the PS10 and PS20 plants in Spain, and the initial SEGS units in the USA [31,111]. Moreover, the largest Kalina cycle turbine ever manufactured was about 8 MW in size [112]. Thus, considering a trade-off between the two aspects, the CSP plants in this thesis were designed for a net electrical power output of 20 MW. According to a turbine manufacturer, Arani Power Systems Ltd [112], and from the available literature [52,98], it was found that the turbines can operate with an isentropic efficiency between 79 % and 90 % at design condition. The lower values in the range are valid for smaller turbines (upto a few MW). Therefore, a value of 85 % was assumed in this study. Similarly, for the pumps, the efficiency was found to vary between 60 % to 85 % [18,52,98]. A typical value of 70 %, which is also within this range, was therefore considered in this study. The minimum separator inlet vapour quality was fixed at 5 % to ensure two-phase flow at the separator inlet. The other assumed values are in the range generally used for such analyses [98,99]. Table 4.1 lists the other assumed values for the cycle design calculations that were provided as the input to the solution algorithm.

Table 4.1: Assumptions for Kalina cycle design calculations [60,98].

Parameter	Symbol	Assumed value
Turbine inlet temperature	T_1	500 °C
Turbine mechanical efficiency	$\eta_{\text{tur,m}}$	98 %
Generator efficiency	η_{gen}	98 %
Minimum PPTD for recuperators	$\Delta T_{\text{pp,re,min}}$	8 °C
Minimum PPTD for condensers	$\Delta T_{\text{pp,cd,min}}$	4 °C
Minimum turbine outlet vapour quality	$X_{\text{tur,out,min}}$	90 %
Minimum separator inlet vapour quality	$X_{\text{sep,in,min}}$	5 %
Condenser cooling water inlet temperature	$T_{\text{cw,in}}$	20 °C
Cooling water temperature rise	ΔT_{cw}	10 °C

4.1.2 Algorithm extension

The algorithm presented in Figure 4.2 can be extended to suit other applications in a fairly straightforward manner. As an example, the extended algorithm for a parabolic trough CSP plant (Figure 4.4) is shown in Figure 4.5. This algorithm later becomes a part of the thermoeconomic optimization routine for the parabolic trough CSP plant as presented in Chapter 5. The additional components in the power block of the parabolic trough CSP plant are the boiler (consisting of a superheater, an evaporator, and an economizer) and the heat transfer fluid pump. The additional inputs for the cycle design were the desired solar field outlet temperature ($T_{\mathrm{htf},1}$) and the assumptions regarding the solar field design. In the current study, the desired solar field outlet temperature ($T_{\mathrm{htf},1}$) was fixed at 390 °C assuming the use of Therminol VP-1 as the heat transfer fluid whose operating temperature range is 12-400 °C [113]. The assumptions for the parabolic trough solar field design are explained in detail in Section 5.2.

For the power block, an additional parasitic consumption in terms of the required power for the solar field heat transfer fluid pump ($\dot{W}_{\mathrm{pu,htf}}$) needs to be calculated in this case. This was done by using the total pressure drop on the heat transfer fluid side based on assumptions for the SEGS VI parabolic trough CSP plant, calculated using the following equation [114,115]:

$$\dot{W}_{\mathrm{pu,htf}} = \frac{\Delta p_{\mathrm{htf}} \cdot \dot{V}_{\mathrm{pu,htf}}}{\eta_{\mathrm{pu,is}}} \tag{4.28}$$

$$\Delta p_{\mathrm{htf}} = \Delta p_{\mathrm{pip}} + \Delta p_{\mathrm{loop}} + \Delta p_{\mathrm{blr}} \tag{4.29}$$

where Δp_{htf} is the total pressure drop on the heat transfer fluid side calculated as the sum of Δp_{pip}, Δp_{loop} and Δp_{blr}, which respectively are the pressure drop in the field headers and piping, the pressure drop in every loop, and the pressure drop in the boiler or steam generator on the heat transfer fluid side. $\dot{W}_{\mathrm{pu,htf}}$ is the required pump power to operate the heat transfer fluid pump, $\eta_{\mathrm{pu,is}}$ is the pump efficiency, and $\dot{V}_{\mathrm{pu,htf}}$ is the volumetric flow rate of the heat transfer fluid passing through the pump.

A heat transfer fluid pressure drop of 21 bar was assumed for the SEGS VI plant solar field (headers and loop) in the current study against the 20.684 bar mentioned in Lippke [114]. This value was then used for calculating the field design pressure drop in the current study through extrapolation. Δp_{blr} was assumed to be 2 bar on the heat transfer fluid side at design condition, a little lower than the 2.964 bar for the SEGS VI plant [114] in order to conservatively design the heat exchanger giving a larger area that would directly affect the cost of the plant. Similarly, Δp_{loop} was assumed to be 3 bar at design condition for typical design velocities [18]. Finally, Δp_{pip} at design condition was estimated using a pressure drop of 18 bar for a field size for the 50 loops of the SEGS VI plant (a value higher than the actual pressure drop in SEGS VI plant [114] for a conservative assumption), and changing it based on the number of loops required in the solar field for every iteration [114]. The

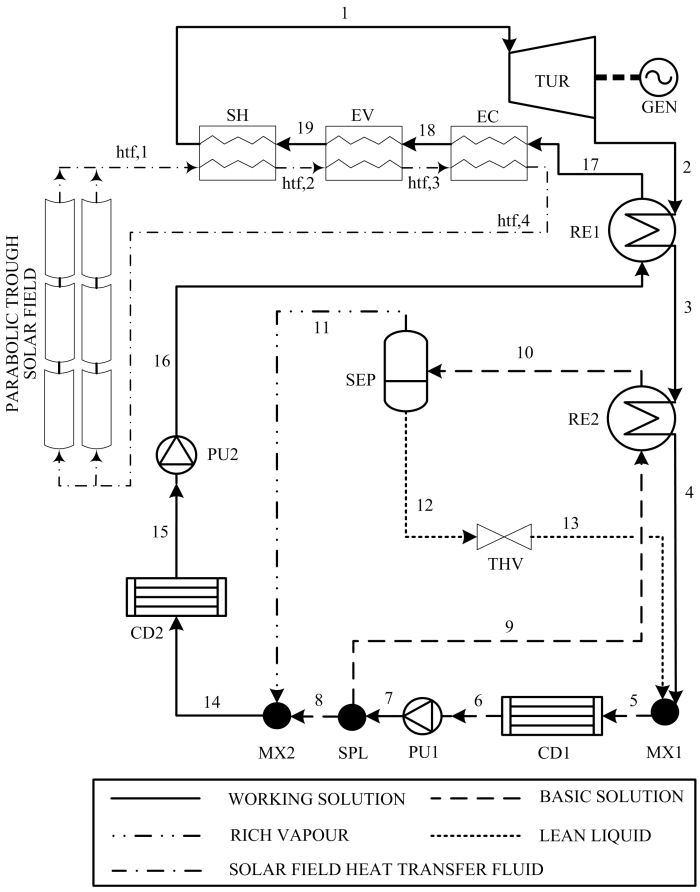

Figure 4.4: Kalina cycle KC12 for a parabolic trough CSP plant.

volumetric flow rate of the heat transfer fluid at the pump inlet ($\dot{V}_{\mathrm{pu,htf}}$) was calculated at solar field inlet temperature ($T_{\mathrm{htf,4}}$ in Figure 4.4).

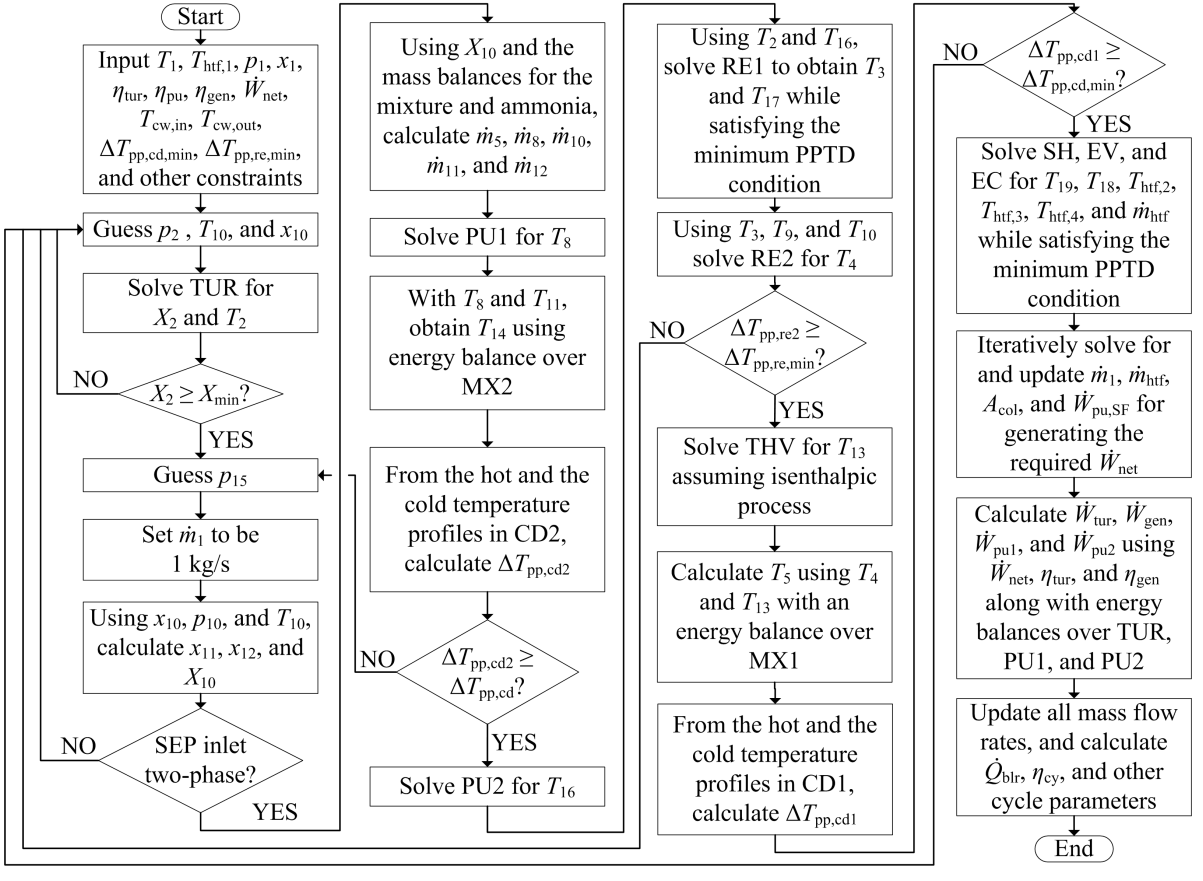

Figure 4.5: Solution algorithm for every iteration for the Kalina cycle KC12 for a parabolic trough CSP plant.

4.1.3 Algorithm flexibility

The presented general solution methodology can be used to solve other Kalina cycle configurations in a similar manner. As an example, the detailed algorithm to solve the more complex KC1234 layout (Figure 3.8) using the proposed methodology is shown in Appendix C. The stream numbers for KC12 layout in Figure 4.3 for the simplified mass balances should be replaced by the respective stream numbers from the other layouts as shown in Table 4.2. The results from the thermodynamic optimization of four different Kalina cycle layouts for a central receiver CSP plant are compared in Section 4.4.

Table 4.2: Respective stream numbers for different Kalina cycle layouts for the simplified mass balances.

	Corresponding number for		
Number in Figure 4.3 for KC12	KC123	KC234	KC1234
1	1	1	1
5	5	4	5
8	8	7	8
10	10	10	11
11	11	11	12
12	13	13	14

4.2 Optimization

The objective of the thermodynamic optimization was to maximize the cycle efficiency for a required plant rated capacity (the net electrical power output):

$$\Phi = \max\left(\frac{\dot{W}_{\text{net}}}{\dot{Q}_{\text{cy,in}}}\right) \tag{4.30}$$

where Φ is the optimization objective function, $\dot{W}_{\text{net}}$ is the power plant net electrical power output (i.e. the plant rated capacity), and $\dot{Q}_{\text{cy,in}}$ is the heat input to the power cycle. The overall thermodynamic design optimization process is shown in Figure 4.6.

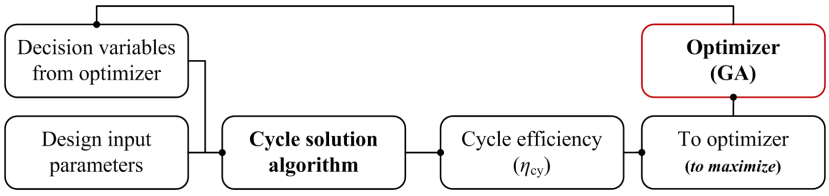

Figure 4.6: Thermodynamic design optimization process for a Kalina cycle CSP plant without storage.

Any optimization process involves the following four key quantities: (1) the objective function, (2) the decision variables, (3) the fixed input parameters, and (4) the design constraints. The objective function defines the purpose of the optimization. It could be thermodynamic, economic, or thermoeconomic, e.g. maximizing the cycle efficiency, minimizing the exergy destruction, minimizing the investment cost, etc. The decision variables are those quantities which are varied during the optimization in order to identify that combination which fulfils the optimization objective. As explained before in Section 4.1, the turbine outlet pressure and the separator inlet temperature and ammonia mass fraction were selected as the decision variables in this study. The fixed input parameters are those quantities that remain unchanged during the optimization, and are provided as input to the optimizer. These could be the turbine inlet conditions, the condenser cooling water inlet temperature, the plant rated capacity, the various component efficiencies, etc. The design constraints are the limitations or restrictions imposed on the optimization process. These constraints could be the bounds for the decision variables, meaning that range of values within which the decision variables are changed during the optimization process. The design constraints could also be other limitations on the cycle design such as the limit on the minimum PPTD in the heat exchangers, minimum vapour quality at the turbine outlet, and so on.

The Kalina cycle was optimized in this study using the GA option from the Optimization Toolbox of MATLAB [116]. The GA is particularly useful for highly non-linear or discontinuous problems such as the Kalina cycle where in addition to the pressure and temperature, the ammonia mass fraction also hugely impacts the thermodynamic state of the mixture, and thus the cycle design. In a GA based optimization, the lower and the upper bounds for the decision variables are provided as an input to the optimizer. The GA then begins with different combinations of the decision variable values (the initial 'population') covering the entire search space, gradually proceeding towards the optimum by eliminating the worse solutions following the principles of natural selection ('evolution'). The use of the bounds instead of initial guess values for the decision variables enables the GA to search the entire solution space and find a global optimum instead of a local optimum. The optimization steps in this study were as follows:

1. The design input parameters were provided as input to the GA ('Optimizer' in Figure 4.6). These included the turbine inlet conditions (temperature, pressure, and ammonia mass fraction), the required net electrical power output from the plant, the different component efficiencies (for the turbine, the pumps, and the generator), and the condenser cooling water inlet temperature and temperature rise as explained at the end of Section 4.1.1. The lower and upper bounds for the decision variables were also provided as input, along with other constraints such as the minimum values of the PPTDs for the condensers and the recuperators, and the minimum allowed vapour quality at the turbine outlet and at the separator inlet.
2. The GA then selected an initial population (several combinations of the decision variables)

covering the entire search space to commence the optimization process, moving gradually towards the optimal solution with each iteration. An 'iteration' here signifies a different combination of the decision variable values.

3. In order to ensure that a global optimum is found, and not a local one, the optimization process was run multiple times with different ranges for the decision variable bounds. As a result of the optimization, the cycle efficiency and the thermodynamic states at various points in the cycle were obtained.

4. The initial population for the GA was 100 and the maximum number of generations was 50. The elite count was 2, the crossover fraction was 0.8, and the function tolerance was 10^{-6}, all default values in the toolbox.

The cycle efficiencies from the different combinations of the decision variables (i.e. from different GA iterations) were compared, and the solution with the highest cycle efficiency was stored as the optimal solution for the given input of the turbine inlet pressure and ammonia mass fraction. The same procedure was then repeated for different values of the turbine inlet pressures and ammonia mass fractions for a parametric study.

4.3 Validation

In order to ensure the mathematical accuracy of the Kalina cycle solution algorithm, several checks related to the mixture mass balances, ammonia mass balances, and energy balances over various cycle components were included in the process. It was ensured that all the balances were satisfied with a residual below or equal to 0.001 % so that the algorithm only provides mathematically and physically feasible solutions. In case there was an error in the calculation of the thermodynamic properties by REFPROP during the optimization, or the balances were not satisfied within the specified tolerance, the solution was rejected and the optimizer selected a different combination of the decision variables for the next GA iteration.

To the author's knowledge, there is no publication with the operating states of a high temperature Kalina cycle that were either obtained experimentally, or from the measurements from a commercial plant. It was therefore only possible to validate the Kalina cycle models in this thesis with previously published modelling results. Only Marston [95] provides all the modelling assumptions and results required for a validation. The layout investigated in Marston [95] is named KC234 in this study (Figure 3.7). In order to validate the overall solution methodology, this layout was therefore used.

Table 4.3 shows the results from model validation. For different combinations of the turbine inlet ammonia mass fraction and the separator inlet temperature taken from Marston [95], it was found that the maximum deviation of the cycle efficiency values calculated using

Table 4.3: Model validation results.

x_1	x_{10}	T_{10} (°C)	η_{cy}, [95]	η_{cy}, model	Deviation (%)
0.55	0.3313	65	0.3228	0.3212	0.50
	0.3339	70	0.3267	0.3236	0.95
	0.3551	75	0.3252	0.3185	2.06
0.60	0.3683	65	0.3174	0.3152	0.69
	0.3700	70	0.3207	0.3179	0.87
	0.3738	75	0.3242	0.3204	1.17
	0.3980	80	0.3218	0.3147	2.21
0.65	0.4072	65	0.3134	0.3101	1.05
	0.4085	70	0.3161	0.3129	1.00
	0.4106	75	0.3192	0.3161	0.97
	0.4155	80	0.3233	0.3192	1.27
	0.4394	85	0.3225	0.3155	2.17
0.70	0.4443	60	0.3073	0.3048	0.81
	0.4450	65	0.3085	0.3073	0.39
	0.4475	70	0.3109	0.3098	0.35
	0.4514	75	0.3136	0.3125	0.35
	0.4563	80	0.3174	0.3159	0.47
	0.4648	85	0.3222	0.3194	0.87

the current algorithm from those presented in Marston [95] was 2.21 %, with the average deviation being 1.01 %. The validation was done using the same modelling assumptions as mentioned in Marston [95], but with the Kalina cycle solution methodology proposed here. With these low deviations, the solution algorithm proposed here was considered validated.

4.4 Results

The optimal cycle efficiency values for the four high temperature Kalina cycle layouts (KC12, KC123, KC234, and KC1234) at different turbine inlet pressures and ammonia mass fractions are shown in Figure 4.7. Among the compared configurations, the maximum cycle efficiency was obtained by the KC1234 layout (31.61 %) at a turbine inlet pressure and ammonia mass fraction of 140 bar and 0.8. The KC123 and the KC12 layouts were close with their maximum cycle efficiencies respectively equal to 31.60 % and 31.54 %, at a turbine inlet pressure and ammonia mass fraction of 140 bar and 0.8 for both the layouts. The lowest cycle efficiency was obtained by the KC234 layout (27.35 %) at a turbine inlet pressure and ammonia mass fraction of 100 bar and 0.8. The maximum turbine inlet pressure was restricted at 140 bar so as to avoid supercritical operation with higher values of the turbine inlet ammonia mass fractions which would result in using complicated designs and more expensive, high pressure resistant materials. The turbine inlet ammonia mass fraction was

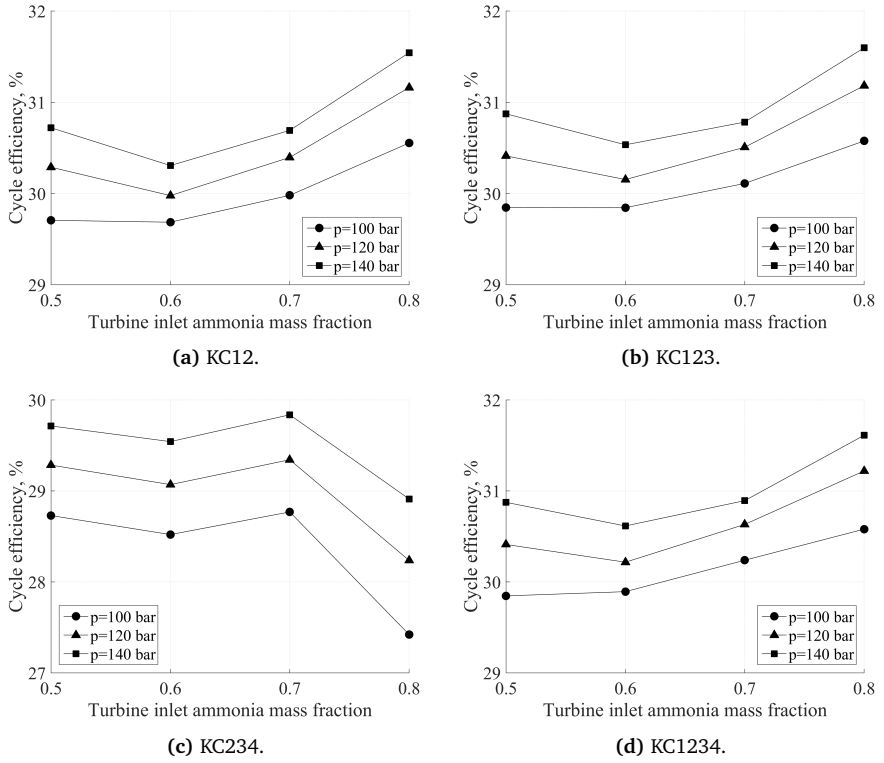

(a) KC12. **(b)** KC123.

(c) KC234. **(d)** KC1234.

Figure 4.7: Optimal cycle efficiencies at different turbine inlet pressures and ammonia mass fractions for the various Kalina cycle layouts for a central receiver CSP plant with a turbine inlet temperature of 500 °C.

varied between 0.5 and 0.8 as the ammonia mass fractions lower than 0.5 are too close to a steam Rankine cycle and may not necessarily utilize the sliding evaporation and condensing characteristics of the ammonia-water mixture. The higher values of ammonia mass fraction had many issues with the convergence of the thermodynamic property calculations, and will also result in supercritical operation conditions.

The cycle efficiency curves for the KC12, the KC123, and the KC1234 layouts (Figures 4.7a, 4.7b, and 4.7d, respectively) are similar in nature. The KC234 layout cycle efficiency curve (Figure 4.7c), on the other hand, has a distinct maxima around a turbine inlet ammonia mass fraction of 0.7, a behaviour also observed in previous studies [95,98]. For any high temperature Kalina cycle configuration, the condenser performance and the effectiveness of recuperation within the cycle govern the overall performance. These two are connected by the ammonia mass fractions of the working solution and the basic solution. From the condenser side, particularly for the condenser CD1, a lower basic solution ammonia mass fraction results in a lower condenser pressure for a given cooling water temperature, thereby

Table 4.4: Rate of heat transfer for the various Kalina cycle layouts at a turbine inlet pressure, temperature, and ammonia mass fraction of 100 bar, 500 °C, and 0.7.

		Value (MW)			
Component	Symbol	KC12	KC123	KC234	KC1234
Recuperator RE1	$\dot{Q}_{re1}$	14.60	12.76	-	11.55
Recuperator RE2	$\dot{Q}_{re2}$	27.02	28.60	28.51	21.55
Recuperator RE3	$\dot{Q}_{re3}$	-	1.48	8.27	2.22
Recuperator RE4	$\dot{Q}_{re4}$	-	-	9.01	8.31
Condenser CD1	$\dot{Q}_{cd1}$	29.84	30.76	33.34	30.22
Condenser CD2	$\dot{Q}_{cd2}$	16.02	14.81	15.33	15.07

resulting in more expansion in the turbine for the same inlet pressure. At the same time, a higher ammonia mass fraction in the condenser results in reduced irreversibility in the condenser, thereby improving the overall cycle efficiency. In addition, the recuperator pinch points also restrict the range of the basic solution ammonia mass fractions, and thus the condenser pressure, for feasible cycle operation.

For the layout KC12, the cycle efficiency first decreases, then increases with the increase in the turbine inlet ammonia mass fraction. This is because of the presence of the recuperator RE1 which restricts the basic solution ammonia mass fraction through the condenser CD1 to go below a certain value to avoid pinch violation. This results in a decrease in the efficiency between a turbine inlet ammonia mass fraction of 0.5 and 0.6. In addition, the constraint to have a two-phase flow at the separator inlet along with a minimum PPTD constraint restricts the recuperator RE2 from obtaining a better performance between the turbine inlet ammonia mass fractions of 0.5 and 0.6. The countering effect by the improved condenser and recuperator heat transfer process because of the higher ammonia mass fractions for the turbine inlet ammonia mass fractions of 0.7 and 0.8 then allows the optimal cycle efficiency to increase again. Lastly, the irreversibility for some components such as the throttle valve and the mixers keeps on decreasing with increasing turbine inlet ammonia mass fraction due to a better match between the temperature of the mixing streams [60,100]. This further adds to the rise in the cycle efficiency after reaching the minimum value. A similar explanation is also applicable for the KC123 and the KC1234 layouts because most of the heat within the cycle is still recovered in the recuperators RE1 and RE2 as may be observed in Table 4.4 for an exemplary case, thus making the KC123 and KC1234 layouts behave similarly to the KC12 layout. Although, because of the presence of additional recuperation within the cycle, the overall cycle efficiency is slightly higher. Figures 4.8 to 4.11 show the exemplary thermodynamic and flow conditions for the considered high temperature Kalina cycle layouts for comparison. All the figures are for the optimal solution at a turbine inlet pressure and ammonia mass fraction of 100 bar and 0.7. Appendix C shows the temperature-heat transfer rate (T-$\dot{Q}$) plots for the same case.

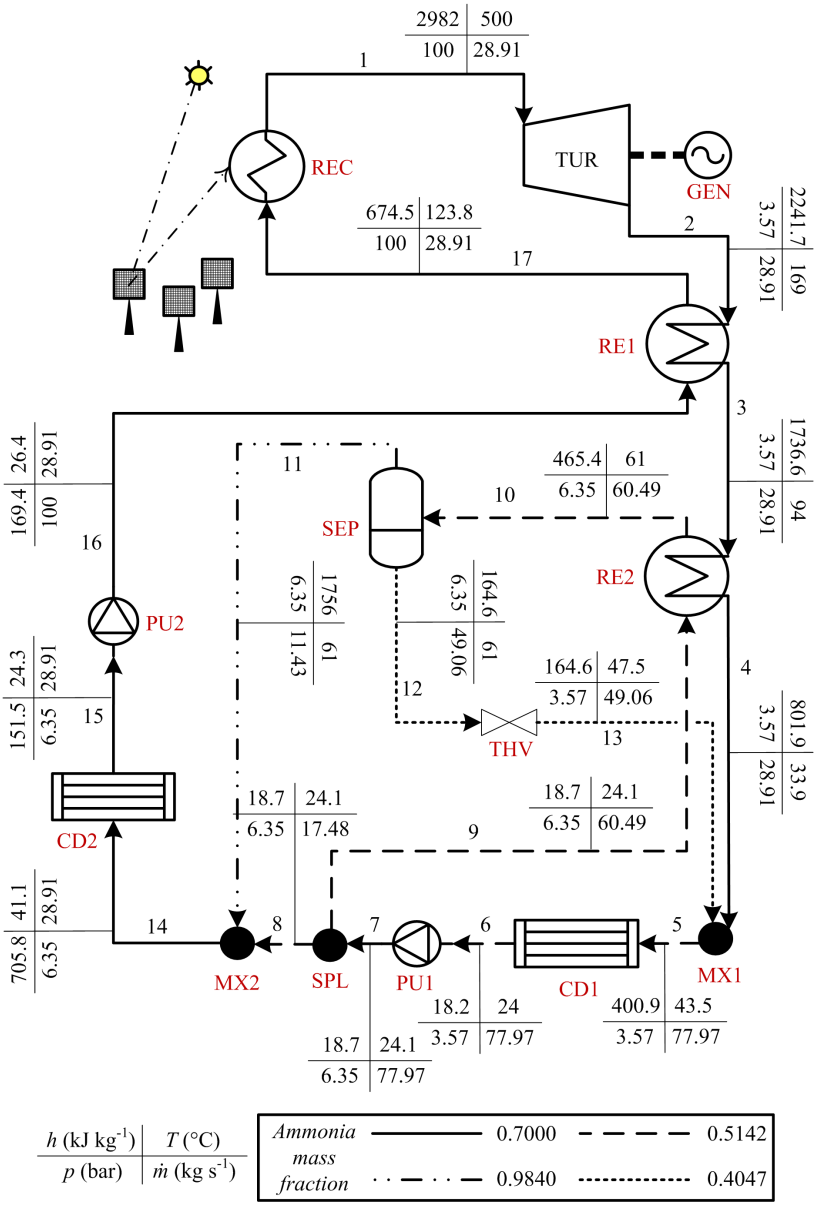

Figure 4.8: Optimal Kalina cycle KC12 design operation state for a central receiver CSP plant at a turbine inlet pressure and ammonia mass fraction of 100 bar and 0.7.

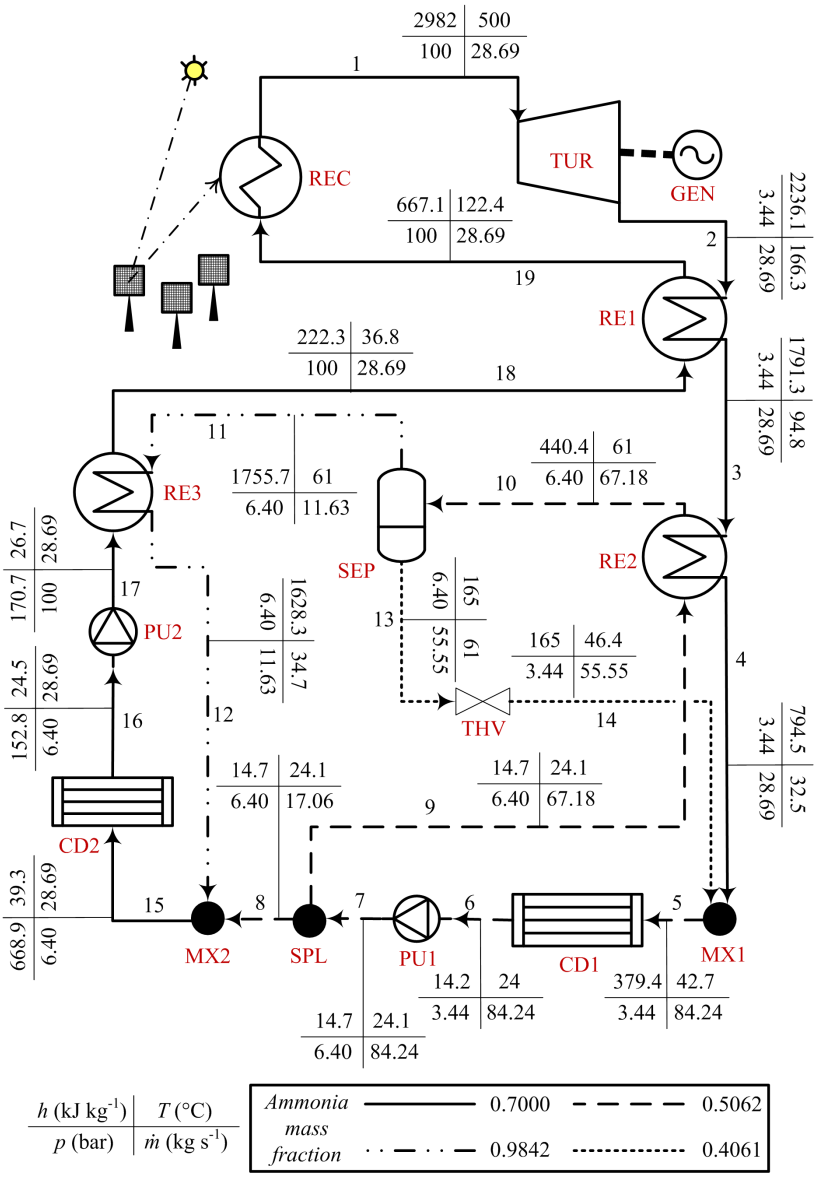

Figure 4.9: Optimal Kalina cycle KC123 design operation state for a central receiver CSP plant at a turbine inlet pressure and ammonia mass fraction of 100 bar and 0.7.

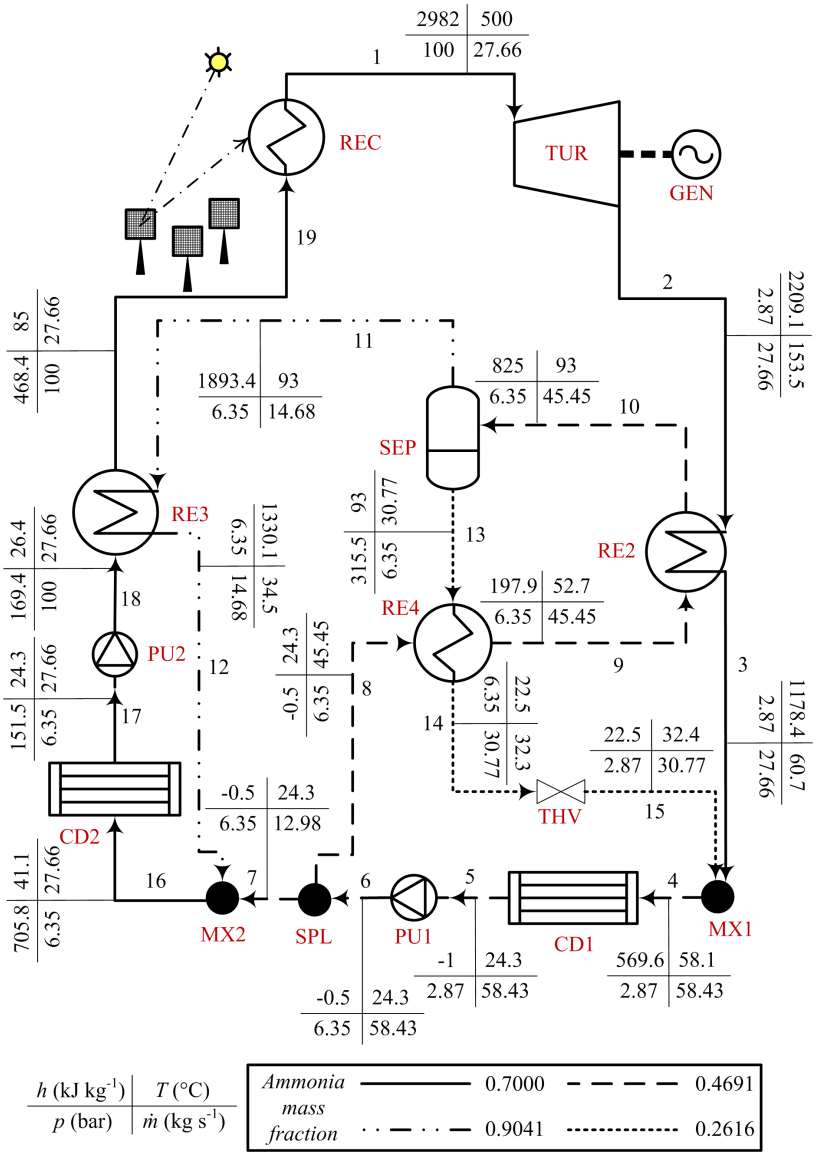

Figure 4.10: Optimal Kalina cycle KC234 design operation state for a central receiver CSP plant at a turbine inlet pressure and ammonia mass fraction of 100 bar and 0.7.

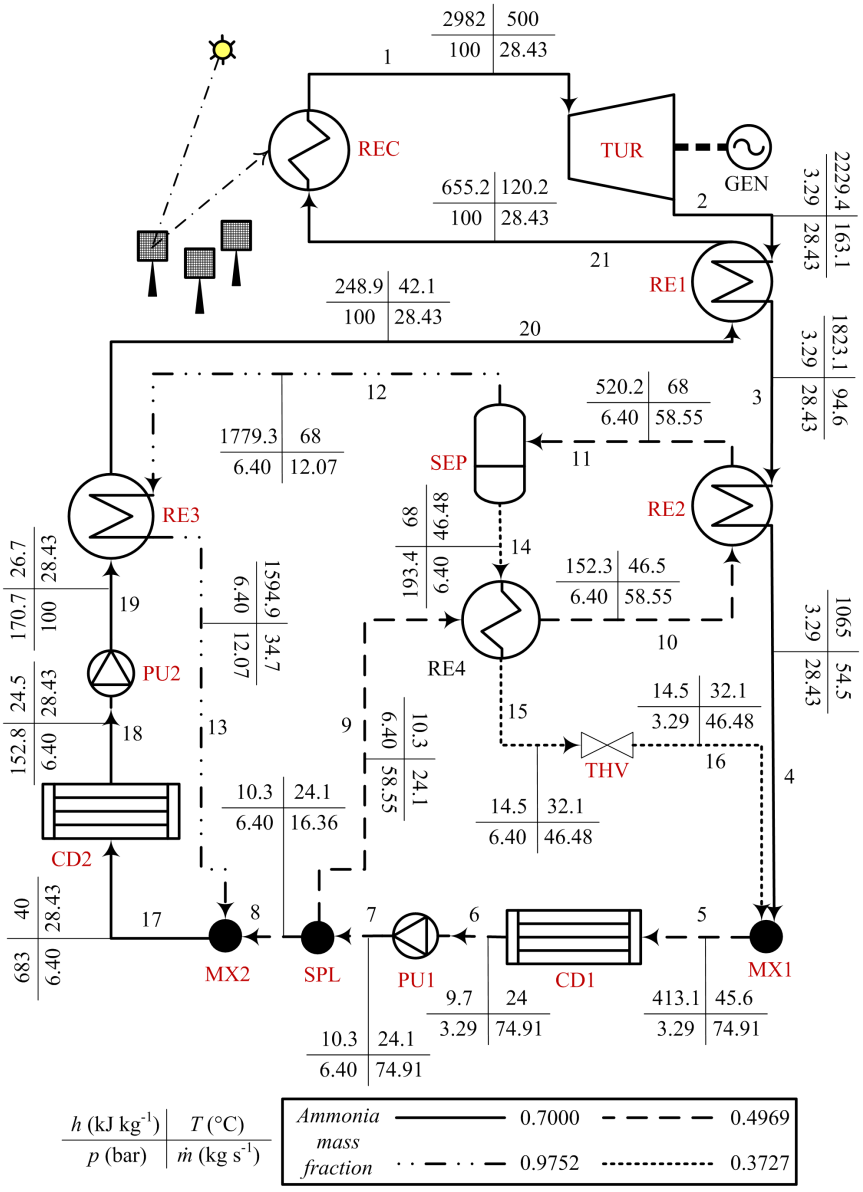

Figure 4.11: Optimal Kalina cycle KC1234 design operation state for a central receiver CSP plant at a turbine inlet pressure and ammonia mass fraction of 100 bar and 0.7.

For the KC234 layout, the existence of a maxima around a turbine inlet ammonia mass fraction of 0.7 (Figure 4.7c) can be attributed to the absence of the recuperator RE1 which is a common feature in the other three layouts. Because of the absence of the recuperator RE1, there is more heat available to be transferred to the separator SEP inlet stream in the recuperator RE2, thus relaxing the limitations on its operation to some extent. This availability of a larger amount of heat in the recuperator RE2 for the KC234 layout results in a lower value of the optimal basic solution ammonia mass fraction of 0.4691 as compared with 0.5142, 0.5062, and 0.4969 for KC12, KC123, and KC1234, respectively. This also results in a much higher separator SEP inlet temperature for the KC234 layout as compared with the other three layouts. The basic solution ammonia mass fraction in the condenser CD1 is able to attain values lower than what was possible in the layouts with the recuperator RE1 also because of the removal of the pinch violation constraint for the recuperator RE1. The higher amount of heat available in the rich vapour and the lean liquid outlet streams from the separator SEP can also be utilized more efficiently respectively in the recuperators RE3 and RE4 [60]. This causes the cycle efficiency to reach a maxima around a turbine inlet ammonia mass fraction of 0.7. The decline at higher turbine inlet ammonia mass fraction afterwards is because of the increase in the condenser CD1 pressure because of rise in the basic solution ammonia mass fraction without the possibility of utilizing the high heat content at the turbine outlet because of the absence of the recuperator RE1. This, along with the rising irreversibility in the mixers resulting in higher condenser inlet temperatures and therefore a higher heat rejection, causes the optimal cycle efficiency to decrease after attaining a maximum value.

4.5 Discussion

A Kalina cycle layout suitable for high temperature applications is inherently complex in nature with the presence of several recuperators, condensers, pumps, and an internal separator loop. Solving such a cycle with high computational efficiency presents a significant challenge. To the author's knowledge, only Marston [95] provided some overall guidelines for solving a high temperature Kalina cycle. There was no other study on high temperature Kalina cycles that presented a detailed general algorithm for solving or optimizing the cycle. For the low temperature applications, Singh and Kaushik [83] and Sun et al. [86] presented algorithms to solve a Kalina cycle for use as a bottoming cycle and as a solar based power cycle, respectively. Along with the presentation of little information on the cycle solution methodology, some inaccurate assumptions were also made concerning the zeotropic nature of the ammonia-water mixture in the above studies. For instance, Marston [95] assumed the pinch point in the condensers to always occur at the working fluid outlet, and both Singh and Kaushik [83] and Sun et al. [86] used an overall LMTD for various heat exchangers, including the evaporator and the condenser, as an input to the cycle calculation. The methodology presented here improves on these assumptions as discussed below.

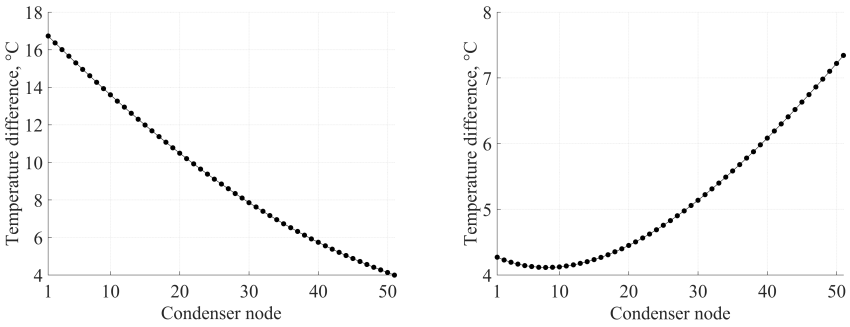

(a) Ammonia mass fraction of 0.5.

(b) Ammonia mass fraction of 0.8.

Figure 4.12: Temperature difference between the hot and the cold fluids over the condenser CD2 for KC1234 for different working fluid compositions at a turbine inlet pressure of 100 bar.

Marston [95] presented a procedure to solve a high temperature Kalina cycle by assuming the separator inlet ammonia mass fraction for a specified separator inlet temperature to initiate the iteration. The cycle mass flow rates were calculated using a simplified topology of the cycle and solving the internal separator loop using mass and energy balances. This was done until the calculated separator inlet ammonia mass fraction came within the acceptable tolerance of the initially assumed value. In the current study, instead of solving the cycle by assuming an initial value for the separator inlet ammonia mass fraction, this parameter is considered as a decision variable for the optimizer. This significantly reduced the computational time, especially when running the simulations with higher values of turbine inlet ammonia mass fractions. As an example, for KC234, a layout similar to the one presented in Marston [95], the cycle thermodynamic optimization with a turbine inlet pressure and ammonia mass fraction of 100 bar and 0.5 took about 50 min using the methodology proposed here, as compared with about 11 h using the approach suggested in Marston [95]. This is mainly because it is much faster to calculate the thermodynamic properties using the ammonia mass fraction as an input rather than trying to iteratively solve for the ammonia mass fraction in a close range of temperature values.

In the procedure suggested in Marston [95], the pinch point in the condensers was assumed to always occur at the cooling water inlet point of the condenser. This is not valid for ammonia-water mixtures with high ammonia mass fractions and leads to incorrect condenser pressure calculations. As an example to highlight this issue, the temperature difference between the working fluid and the condenser cooling water over the condenser CD2 for the KC1234 layout is shown in Figure 4.12. The curve shown in Figure 4.12a is for the optimal solution at a turbine inlet pressure and ammonia mass fraction of 100 bar and 0.5. Figure 4.12b shows the same curve, but for a working fluid ammonia mass fraction of 0.8. The condenser was discretized into 50 control volumes in order to locate the pinch point, thus resulting in 51 nodes as the nodes were assumed at the control volume boundaries. The

node 1 in both the curves represents the *exit* of the cooling water in the condenser, i.e. the node where the working fluid *enters* the condenser, given the assumption of counter-flow heat exchanger. These figures clearly show that the PPTD (the lowest point in the curve, close to 4 °C) occurs at very different positions in the condenser when the working fluid ammonia mass fraction is changed. This is primarily due to the change in the convexity of the temperature profile of the ammonia-water mixtures with changing ammonia mass fraction, as also elaborated in Kim et al. [117]. Therefore, an assumption of a fixed position for the pinch point will not only result in a calculation of an incorrect condenser pressure, but possibly also in a violation of the second law of thermodynamics. As a direct consequence, the cycle efficiency would also be overestimated. The assumption of a constant overall LMTD for the heat exchangers may also result in similar issues, or in unusually low PPTDs.

It is also possible to use the turbine inlet pressure and ammonia mass fractions as additional decision variables for the optimization, but at the cost of computational time. When considering the turbine inlet ammonia mass fraction as a decision variable, another issue is that there are several combinations of the turbine inlet ammonia mass fractions, temperatures, and pressures for which the thermodynamic property calculations were not convergent. This sometimes lead the optimizer to solution spaces away from the global optimum. For this reason, it is recommended to consider the turbine inlet ammonia mass fraction for a parametric study rather than as a decision variable.

The results presented in this chapter are for the optimizations considering the required plant rated capacity as a design input parameter. However, this approach can also be used for other applications such as a bottoming cycle for a gas turbine, waste heat recovery, geothermal power plants, and other types of CSP plants with slight modifications. These modifications are the addition of a few heat exchangers where the heat from a hot fluid is transferred to the Kalina cycle working fluid, additional pinch point evaluations for these heat exchangers, and any additional parasitic loads. In the cases where the heat input is a fixed quantity such as a waste heat recovery plant, the energy available in the hot fluid stream shall be an input to the optimizer (by mentioning the inlet and the outlet temperatures, and the mass flow rate), instead of the design rated capacity. The objective function in such cases for a thermodynamic optimization shall be to maximize the specific power output from the plant. It is also possible to convert the objective function to a thermoeconomic one by maximizing the net present value or minimizing the levelized cost of electricity, while using a similar approach to solve the cycle. This is elaborated in Chapter 5.

From the results of the thermodynamic optimization, it seems that the number and the placement of the recuperators in the cycle plays an important role in governing the cycle performance. The results suggest that the presence of the recuperator RE1 is overall more beneficial than the presence of the recuperators RE3 and RE4, especially for higher values of turbine inlet ammonia mass fractions. Thus, based on the results, it was decided to use

the Kalina cycle KC12 layout to investigate the thermoeconomic performance in this thesis (Chapter 5). It was because this configuration was found to be nearly equally efficient as the more complex KC123 and KC1234 configurations, while being simpler with fewer number of recuperators, implying a lower capital investment cost and a simpler operation and control system.

4.6 Summary

A computationally efficient general methodology to solve and optimize Kalina cycles for high temperature applications was presented. The numerical models based on the proposed methodology were validated against existing literature. The general algorithm could be used for Kalina cycles for various applications such as waste heat recovery, gas turbine bottoming cycle, different CSP plants, etc. with slight modifications depending on the case at hand. The results from the thermodynamic optimization of different Kalina cycle layouts suggest that the placement and the number of the recuperators within the cycle play an important role in determining the overall cycle performance. Among the compared alternatives, the Kalina cycle KC12 layout was selected for the thermoeconomic analysis. This layout was selected for being simpler with fewer recuperators, while being nearly as efficient as the more complex layouts.

5

THERMOECONOMIC ANALYSIS

This chapter presents the thermoeconomic optimization of the Kalina cycle KC12 for a central receiver CSP plant with direct vapour generation, and a parabolic trough CSP plant with Therminol VP-1 as the solar field heat transfer fluid. The part-load modelling approach, the heat exchanger model, and the thermoeconomic model are elaborated. The results from the thermoeconomic optimization are then presented and compared with those from a state-of-the-art steam Rankine cycle.

5.1 Thermoeconomics

In order to design or evaluate any power plant, it is relevant to consider both the thermodynamic and the economic performance of that plant. Designing a thermodynamically efficient plant might lead to an economically unattractive design, whereas the other way might lead to designs which waste resources and are detrimental to the environment. A suitable approach in this regard is to opt for a thermoeconomic design process where both the thermodynamic performance and the economic impact of the design are simultaneously considered. Such a design process for a CSP plant without storage is illustrated in Figure 5.1.

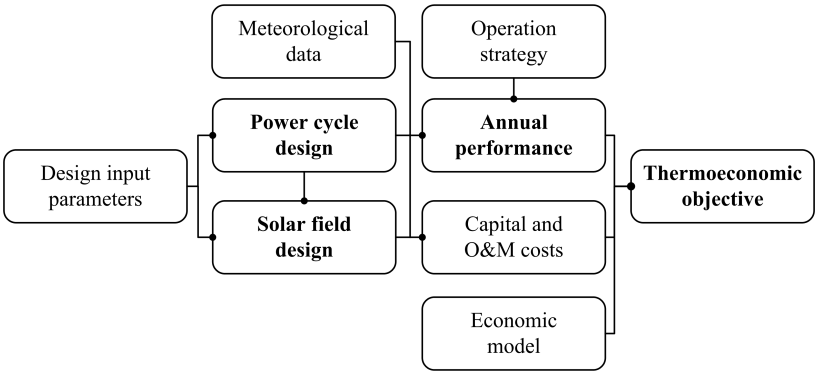

Figure 5.1: Thermoeconomic design process for a CSP plant without storage.

In this thesis, the thermoeconomic analysis of a solar-only CSP plant without storage broadly consisted of the following steps. The design input parameters for both the power cycle and the solar field were fixed based on the state-of-the-art literature and the available technologies, as discussed previously in Section 4.1. For the power cycle, these included the turbine inlet temperature, the net electrical power output from the plant, the turbomachinery and the generator performance indicators, the heat input and rejection conditions, and other constraints such as minimum PPTD and vapour quality. For the solar field, the design input parameters were the design solar irradiance, the solar multiple, and the site location and meteorological data. These are discussed in detail in Section 5.4.

Once the design input parameters were fixed, the power cycle and the solar field were designed for the nominal operation condition. In case of a CSP plant where there are significant daily and seasonal variations in the heat source, it is necessary to include a representative annual performance analysis in order to estimate the plant output over the year. For the annual performance analysis, the part-load performances of the solar field and the power cycle, the plant site location and meteorological data, and the overall plant control and operation strategies were used to estimate the annual electricity production. This was done through hourly simulations over a typical year. The hourly values of the direct normal irradiance (DNI) and other weather data were obtained for a typical meteorological year from Meteonorm [118]. The heat input to the power cycle was obtained using the DNI values along with the part-load performance of the solar field. The net electricity output was then calculated using the part-load performance of the power cycle for the available heat input. Once the thermodynamic performance (design, part-load, and annual) was assessed for a given set of input parameters, the next step was to include suitable cost functions in order to estimate the capital investment and the operations and maintenance (O&M) costs for the power plant. An economic model, with the plant lifetime and the insurance and interest rates as inputs, was used to estimate the value of the thermoeconomic objective. This thermoeconomic objective could be the net present value of the plant, or the LCOE. For CSP plants, the LCOE is the frequently preferred indicator for comparing alternatives [9,10], and is therefore also used in this thesis.

5.2 Optimization

The Kalina cycle CSP plant was optimized by minimizing the LCOE using the optimization routine shown in Figure 5.2. The optimization was done in a similar manner as the thermodynamic optimization using GA as presented in Section 4.2. All the models and analyses presented in this chapter are for the Kalina cycle KC12 layout (shown in Figure 4.1 for the central receiver CSP plant and in Figure 4.4 for the parabolic trough CSP plant).

The LCOE is the average cost of electricity production, and for a solar-only plant, it can be

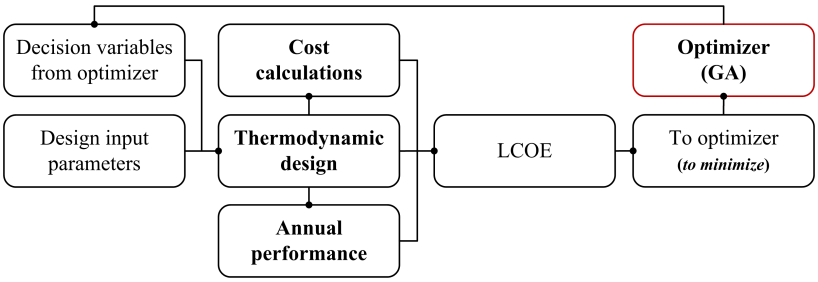

Figure 5.2: CSP plant thermoeconomic optimization routine.

defined as follows [119]:

$$\text{LCOE} = \frac{\text{CRF} \cdot C_{\text{inv}} + C_{\text{O\&M,y}}}{E_{\text{y}}} \tag{5.1}$$

with

$$\text{CRF} = k_i + \frac{k_d \cdot (1+k_d)^{N_p}}{(1+k_d)^{N_p} - 1} \tag{5.2}$$

where CRF is the capital recovery factor, C_{inv} and $C_{\text{O\&M,y}}$ are the plant total capital investment cost and the yearly O&M cost, E_{y} is the yearly electricity production, k_i and k_d are the annual insurance and real debt interest rates, and N_p is the plant lifetime in years. In order to minimize the LCOE, the Kalina cycle was first solved thermodynamically using the solution algorithm presented in Section 4.1. From this, the design point thermodynamic state and the UA values for all the control volumes of the various heat exchangers were obtained. The UA values were obtained using:

$$(\text{UA})_{\text{i,d}} = \frac{\dot{Q}_{\text{i,d}}}{\Delta T_{\text{lm,i,d}}} \tag{5.3}$$

where $U_{\text{i,d}}$, $A_{\text{i,d}}$, $\dot{Q}_{\text{i,d}}$, and $\Delta T_{\text{lm,i,d}}$ are respectively the overall heat transfer coefficient, heat transfer area, the heat transfer rate, and the LMTD for the i^{th} control volume at the design point of operation.

Table 5.1 shows the key assumptions regarding the economic model for the CSP plants referred from the ECOSTAR report [119]. The details of the Kalina cycle and the solar field models, and the cost estimation functions are presented in the coming sections.

Table 5.1: Economic model assumptions [119].

Parameter	Symbol	Value
Plant lifetime	N_p	30 a
Annual insurance rate	k_i	1 %
Real debt interest rate	k_d	8 %

5.3 Kalina cycle

For the thermoeconomic optimization of the Kalina cycle CSP plant, the Kalina cycle first needed to be solved thermodynamically to obtain the design operating conditions, which was done using the solution methodology presented in Section 4.1. The additional numerical models required for the thermoeconomic analysis for the part-load performance evaluation and the heat exchanger area estimation are presented here.

5.3.1 Part-load model

To the author's knowledge, only Kalina and Leibowitz [71] and Smith et al. [80] presented performance curves for the part-load conditions using a Kalina cycle, however without providing any methodology to estimate the part-load performance of the cycle. Kalina and Leibowitz [71] mentioned that the second law efficiency of the Kalina bottoming cycle for a gas turbine changes by about 3.2 percentage points when the cycle load reduces by 25 %. The publication did not present any details about the assumptions or the methodology used for calculating the part-load performance of the Kalina cycle. Moreover, the part-load performance until only 75 % plant load was presented. Smith et al. [80] presented the part-load performance curves for a simple gas turbine, a Rankine combined cycle, and a Kalina combined cycle. The Kalina combined cycle showed the best performance. The operational advantages of the Kalina cycle as compared with the steam Rankine cycle were also presented. This publication also did not provide the part-load characteristics of only the Kalina cycle, or any methodology for evaluating the part-load performance characteristics. From the Kalina combined cycle part-load curve, the part-load performance of only the Kalina cycle cannot be estimated without knowing the combined cycle operation and control strategy, which was also not presented in the publication. A recent patent by Mlcak and Mirolli [120] suggests varying the ammonia mass fraction in order to improve the system performance of the Kalina cycle with varying ambient conditions. The patent however discusses a relatively simpler low temperature application layout to be used with geothermal hot water or industrial waste heat sources.

As the previous studies did not present any methodology for solving the Kalina cycle in part load, a detailed methodology is therefore proposed here based on the validated cycle design models. Since the part-load performance estimation is an optimization problem in itself, the Kalina cycle was solved in part load separately for different plant loads and turbine inlet ammonia mass fractions. The obtained part-load performance curves were then fitted into algebraic equations to be used in the thermoeconomic optimization model. In this way, the computational time for the annual performance calculations with hourly simulations was significantly reduced. For the part-load performance calculations, a solution algorithm similar to the validated thermodynamic optimization algorithm was used, but with different decision variables and few additional assumptions as required for the part-load calculations.

The part-load solution algorithm is first explained for a central receiver CSP plant, and then extended to be used with a parabolic trough CSP plant.

For the **central receiver CSP plant**, the heat input to the receiver REC was gradually decreased and the part-load relative efficiency curves for different plant loads and turbine inlet ammonia mass fractions were prepared using the following assumptions for the steady-state part-load calculations:

- The turbine inlet temperature was maintained at its design value in order to have the highest temperature at the turbine inlet for better efficiency. The turbine inlet ammonia mass fraction was maintained at its respective design point value in order to avoid fluctuations in the turbine power output, as suggested by Amano et al. [107].
- The condenser cooling water inlet temperature was assumed to be the same as its design value [114]. In order to satisfy the condensing load, the condenser cooling water mass flow rate would then adjusted by regulating the cooling water pump.
- The minimum separator inlet vapour quality was fixed at 2 %, a value smaller than the design value, but enough to ensure that there will be a two-phase flow at the separator inlet. The separator inlet ammonia mass fraction was allowed to vary within ±1 % of the design value so that the power law (Equation (5.8)) could be employed for heat exchanger off-design calculations.
- The condenser working fluid outlet temperature was maintained at least 2 °C higher than the cooling water inlet temperature, and the tolerance δ_T for the estimation of the temperature T_9 (Figure 5.3) was set to 0.1 K.

The turbine was modelled in part load using the Stodola's ellipse law [121] which relates the turbine inlet temperature, pressure, and mass flow rate, and the turbine outlet pressure through a turbine constant (k_{tur}):

$$k_{tur} = \frac{\dot{m}_1 \cdot \sqrt{T_1}}{\sqrt{p_1^2 - p_2^2}} \tag{5.4}$$

while the off-design isentropic efficiency of the turbine was estimated from [122]:

$$\eta_{\text{tur,is}} = \eta_{\text{tur,is,d}} - 2 \cdot \left[\frac{N_{\text{tur}}}{N_{\text{tur,d}}} \cdot \sqrt{\frac{\Delta h_{\text{is,tur,d}}}{\Delta h_{\text{is,tur}}} - 1} \right]^2 \tag{5.5}$$

where $\eta_{\text{tur,is}}$ and $\eta_{\text{tur,is,d}}$ are the turbine isentropic efficiencies at part-load and design conditions, N_{tur} and $N_{\text{tur,d}}$ are the turbine rotational speeds at part-load and design conditions, and $\Delta h_{\text{is,tur}}$ and $\Delta h_{\text{is,tur,d}}$ are the isentropic specific enthalpy differences at part-load and design conditions. The turbine speed in a power plant is always maintained at the design value in order to keep the frequency of the generated electricity at a constant value, and therefore the

ratio of the speeds in Equation (5.5) is taken as unity [122]. Although the mechanical losses typically remain constant in absolute terms during part-load operation, the mechanical efficiency of the turbine was assumed the same as its design value for simplification.

The off-design isentropic efficiency of the pumps was obtained using [114]:

$$\eta_{\mathrm{pu,is}} = \eta_{\mathrm{pu,is,d}} \cdot \left[2 \cdot \frac{\dot{m}_{\mathrm{pu}}}{\dot{m}_{\mathrm{pu,d}}} - \left(\frac{\dot{m}_{\mathrm{pu}}}{\dot{m}_{\mathrm{pu,d}}} \right)^2 \right] \tag{5.6}$$

where $\eta_{\mathrm{pu,is}}$ and $\eta_{\mathrm{pu,is,d}}$ are pump efficiencies at part-load and design conditions, and $\dot{m}_{\mathrm{pu}}$ and $\dot{m}_{\mathrm{pu,d}}$ are the mass flow rate through the pump at part-load and design conditions.

The off-design generator efficiency was obtained using [123]:

$$\eta_{\mathrm{gen}} = \frac{\eta_{\mathrm{gen,d}} \cdot \zeta_{\mathrm{gen}}}{\eta_{\mathrm{gen,d}} \cdot \zeta_{\mathrm{gen}} + \left(1 - \eta_{\mathrm{gen,d}}\right) \cdot \left[\left(1 - F_{cu}\right) + F_{cu} \cdot \zeta_{\mathrm{gen}}^2 \right]} \tag{5.7}$$

where F_{cu} is the copper loss fraction (assumed 0.43 [123]), η_{gen} and $\eta_{\mathrm{gen,d}}$ are the generator efficiencies at part-load and design conditions, and ζ_{gen} is the generator load relative to the design value.

The heat exchangers were again discretized in the part-load conditions to obtain the temperature profiles. The UA values in part load were obtained using the power law as shown below [22,115,124]:

$$(\mathrm{UA})_{\mathrm{i}} = (\mathrm{UA})_{\mathrm{i,d}} \cdot \left(\frac{\dot{m}}{\dot{m}_{\mathrm{d}}} \right)^{0.8} \tag{5.8}$$

where $(\mathrm{UA})_{\mathrm{i}}$ and $(\mathrm{UA})_{\mathrm{i,d}}$ are the UA values at part-load and design conditions for the i^{th} control volume, and $\dot{m}$ and $\dot{m}_{\mathrm{d}}$ are the mass flow rates of the cold fluid at part-load and design conditions.

The Kalina cycle was solved in part load using Equations (4.1) to (4.11) and (5.4) to (5.8) with the algorithm shown as a flowchart in Figure 5.3. The numbers in the subscript and the component names in the flowchart correspond to the cycle layout in Figure 4.1. For the part-load operation, the following control strategy was used. A sliding pressure operation was assumed while maintaining the turbine inlet temperature at the design value. In case it was not possible to find a feasible operating point while maintaining the turbine inlet temperature at its design value, the turbine inlet temperature was gradually reduced from its design value. In order to obtain the highest part-load performance from the cycle, the separator inlet ammonia mass fraction was varied. In practice, it is easier to measure the temperatures and pressures in the cycle than the ammonia mass fraction, especially when the mixture is in two-phase flow. Since the pressure at the pump PU1 outlet is governed by the ammonia mass fraction in the condenser CD2, the splitter SPL split fraction (i.e. the ratio of the mass flow rate of stream 9 to that of stream 7 in Figure 4.1) needs to be varied to

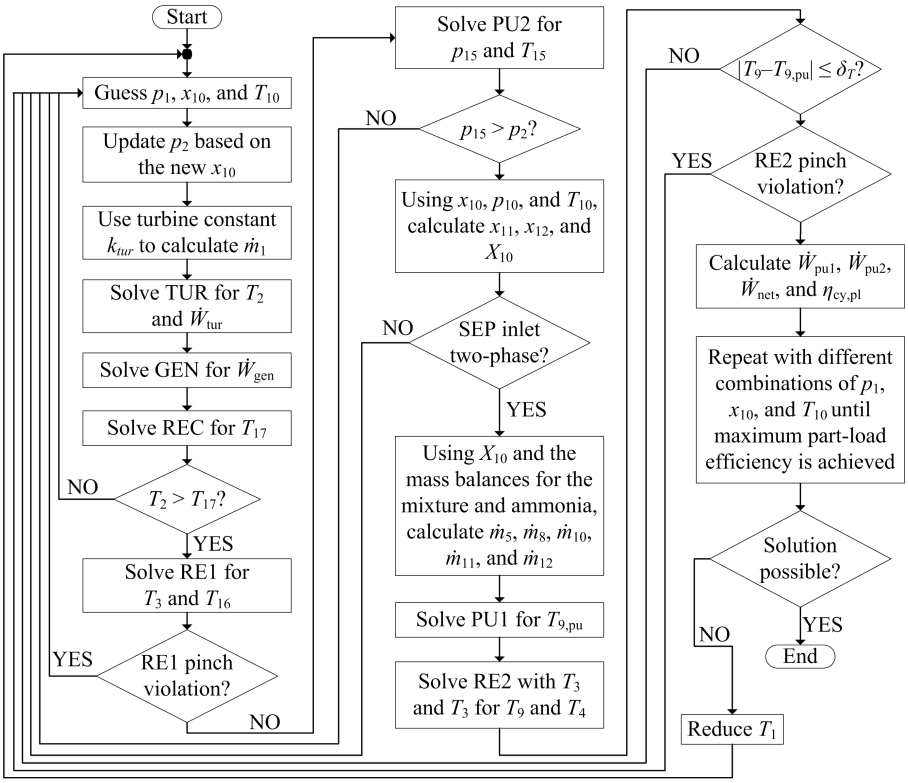

Figure 5.3: Part-load solution algorithm for the Kalina cycle KC12 for a central receiver CSP plant.

obtain the required optimal separator inlet ammonia mass fraction. This split fraction can be varied by changing the splitter SPL valve position, and this position in turn determines the separator inlet ammonia mass fraction. For a given value of the pump PU1 outlet pressure (which is also the separator SEP inlet pressure), there will be only one combination of the temperature and the ammonia mass fraction at the separator inlet which results in the highest part-load performance. Thus, the separator SEP inlet temperature can be monitored in order to specify the optimal splitter valve position, or in other words, the optimal split fraction. In practice, it is the pumps and the splitter which will be controlled during part-load operation, however for modelling purposes, it is better to provide the ammonia mass fraction as the varying parameter rather than the split fraction as it speeds up the computation significantly [60]. This is because the ammonia mass fraction is always required as an input to calculate the thermophysical properties for the mixture, and therefore providing it as an input considerably reduces the required number of iterations.

For the **parabolic trough CSP plant**, additional constraints were required for the boiler. These were the calculation of the UA values for the superheater, the evaporator, and the

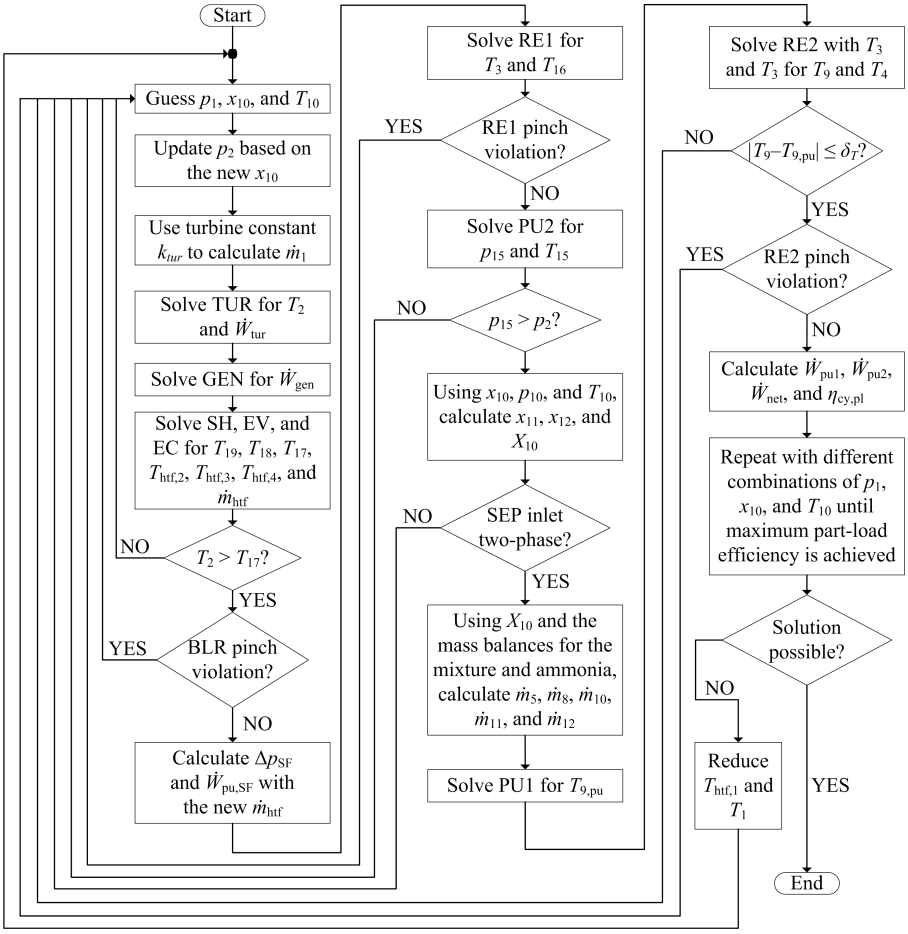

Figure 5.4: Part-load solution algorithm for the Kalina cycle KC12 for a parabolic trough CSP plant.

economizer using Equation (5.8), and ensuring that there were no pinch violations in the boiler at part-load conditions. The part-load solution algorithm for the parabolic trough CSP plant with Kalina cycle KC12 is shown in Figure 5.4. All the subscripts and component names correspond to the plant layout shown in Figure 4.4. The following operation and control strategy was used. The solar field outlet temperature ($T_{htf,1}$) was maintained at its design value by reducing the heat transfer fluid mass flow rate ($\dot{m}_{htf}$) with decreasing solar irradiance. The solar field inlet temperature ($T_{htf,4}$) was then iteratively calculated at different part loads while satisfying the energy balances in the boiler along with other constraints such as the turbine constant, the pinch violations, etc. The turbine inlet temperature was also maintained at its design value. If it was not possible to find a feasible part-load operating state while maintaining the solar field outlet and the turbine inlet temperatures at their respective design values, these temperatures were gradually reduced. The turbine, the generator, the

pumps, and the heat exchangers were modelled in part load using Equations (5.4) to (5.8) in the same way as was done for the central receiver CSP plant.

When compared with a central receiver CSP plant, an additional parasitic consumer is present in the parabolic trough CSP plant in the form of the pumping requirement for the heat transfer fluid flowing through the solar field. Therefore, in order to obtain the part-load efficiency of the Kalina cycle for a parabolic trough CSP plant, it is necessary to estimate this pump power requirement as well. This was done by calculating the total heat transfer fluid pressure drop (Δp_{htf}) as the sum of the pressure drop in the solar field headers and piping (Δp_{pip}), the pressure drop in every loop (Δp_{loop}), and the pressure drop in the boiler or steam generator (Δp_{blr}) at part-load conditions. As a conservative approximation, the pressure drop in the boiler in part-load operation was assumed to remain same as its design value. The part-load pressure drops in the field piping and the loop were calculated from [22,114]:

$$\Delta p_{\text{pip}} = \Delta p_{\text{pip,d}} \cdot \left(\frac{\dot{m}_{\text{htf}}}{\dot{m}_{\text{htf,d}}} \right)^2 \tag{5.9}$$

$$\Delta p_{\text{loop}} = \Delta p_{\text{loop,d}} \cdot \left(\frac{\dot{m}_{\text{htf,loop}}}{\dot{m}_{\text{htf,loop,d}}} \right)^2 \tag{5.10}$$

where $\dot{m}_{\text{htf}}$ and $\dot{m}_{\text{htf,d}}$ are the total heat transfer fluid mass flow rates at part-load and design conditions, and $\dot{m}_{\text{htf,loop}}$ and $\dot{m}_{\text{htf,loop,d}}$ are the heat transfer fluid mass flow rates in each loop at part-load and design conditions, as elaborated in Sections 4.1.2 and 5.4.2. The required pump power was then calculated with Equation (4.28) using the part-load volumetric flow rate through the pump.

5.3.2 Heat exchanger area

The heat exchangers were modelled in order to estimate the required heat transfer areas and thereby the associated costs, following the general approach presented by Kærn et al. [125]. The following assumptions were made for the estimation of the heat exchanger area. For large heat transfer capacities, it is common to use shell-and-tube type heat exchangers [126], therefore all the heat exchangers in this study were modelled as shell-and-tube type with counter-flow arrangement. The heat exchangers were always assumed to have a single shell pass and a single tube pass. The fluid with higher pressure was always put on the tube side as high pressure tubes are less expensive than high pressure shells; and wherever possible, the two-phase flow would be put on the tube side so as to avoid high variation in the mixture composition at different parts of the heat exchanger [127,128]. In case there was a two-phase to two-phase heat transfer, the evaporating fluid was put on the tube side while the condensing fluid was put on the shell side, mainly because the evaporating sides are usually the high pressure sides in the considered cycle layout (KC12).

The maximum shell and tube side liquid velocities were fixed at 0.8 $m\,s^{-1}$ and 2 $m\,s^{-1}$, respectively, in order to avoid excessive pressure drops [128]. The maximum vapour velocity on both the shell and the tube sides was fixed at 22 $m\,s^{-1}$ [126] for the low and intermediate pressure heat exchangers (recuperator RE2 and both the condensers). The same was fixed at 10 $m\,s^{-1}$ [128] for the high pressure heat exchangers (recuperator RE1 and the boiler). The tube outside diameter was assumed to be 20 mm while the tube thickness was assumed to be 1.6 mm for the low and intermediate pressure heat exchangers and 2.6 mm for the high pressure heat exchangers, two common standard tube sizes [128]. The 45 degrees square pattern was assumed for the tube arrangement to maximize the heat transfer [128]. The tube pitch to tube outer diameter ratio was maintained between 1.25 and 1.5 while a baffle cut of 25 % was fixed for the heat exchanger area calculations, two common design assumptions for shell-and-tube heat exchangers [128].

As the temperature profiles in the heat exchangers were not always linear, the heat exchangers were discretized into 50 control volumes on the basis of the heat transfer rate, and the area for each control volume was calculated. The area of the heat exchanger would then be the sum of the areas of all the control volumes. Table 5.2 provides an overview of the heat transfer correlations used in this study. The use of the correlations is explained in detail in Appendix B.

Table 5.2: Heat transfer correlations used in the estimation of the heat exchanger area.

Description	Correlation
Single phase in-tube flow	Gnielinski (1976) [129]
Condensing in-tube flow	Shah (2013) with Silver-Bell-Ghaly (1972) correction for mixtures [130,131]
Evaporating in-tube flow	Shah (1982) [132]
Single phase shell-side flow	Kern (1950) as presented in Smith (2005) [127,133]
Condensing shell-side flow	Kern (1950) as presented in Smith (2005), with Silver-Bell-Ghaly (1972) correction for mixtures [127,131,133]

All the calculations for the estimation of the heat transfer coefficients and areas were made for both the hot and the cold sides wherever necessary. The effect of the ratio of the bulk fluid viscosity to the wall fluid viscosity was neglected during the heat transfer calculations [128], except in case of the boiler in a parabolic trough CSP plant with thermal oil on the shell side as the heat transfer fluid. The following steps were taken to estimate the required heat exchanger areas:

1. Using the geometrical constraints and the design mass flow rates, the required number of tubes was calculated. For this tube bundle, the required shell diameter was then calculated. The required number of tubes was minimized until the maximum allowable flow velocity was reached on either the shell or the tube side.

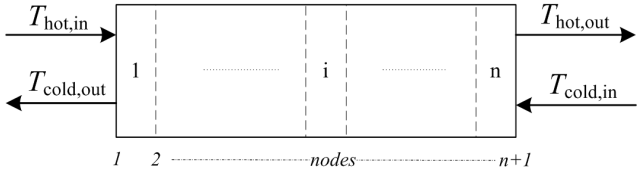

Figure 5.5: Heat exchanger discretization assuming counter-flow arrangement.

2. The heat exchanger was then discretized with respect to the heat transfer rate, as shown in Figure 5.5, using the heat exchanger inlet and outlet conditions (temperature, pressure, and mass flow rates) from the cycle thermodynamic design. This was done to generate the hot and the cold side temperature profiles, i.e. to obtain the inlet and outlet temperatures for each control volume. The subscripts 'hot' and 'cold' respectively denote the hot and the cold fluid sides (which are not necessarily the same as the shell and the tube sides).

3. The LMTDs (ΔT_{lm}) for all the control volumes were then calculated using the respective inlet and outlet temperatures on both the hot and the cold sides using:

$$\Delta T_{\text{lm,i}} = \frac{(T_{\text{hot,i+1}} - T_{\text{cold,i+1}}) - (T_{\text{hot,i}} - T_{\text{cold,i}})}{\ln\left(\frac{T_{\text{hot,i+1}} - T_{\text{cold,i+1}}}{T_{\text{hot,i}} - T_{\text{cold,i}}}\right)} \tag{5.11}$$

   where the equation is shown for the i^{th} control volume. The average fluid temperatures for each control volume were also calculated to estimate the transport properties.

4. By comparing the specific enthalpy of the fluid to the saturated specific enthalpy values, it was determined whether the fluid was in a single phase or a two-phase flow in order to select suitable heat transfer correlation. The overall heat transfer coefficient based on the tube outside area was then calculated using:

$$U_{\text{i}} = \left[\frac{1}{\alpha_{\text{hot}}} + \frac{1}{\alpha_{\text{tube}}} + \frac{D_o}{D_i} \cdot \frac{1}{\alpha_{\text{cold}}}\right]^{-1} \tag{5.12}$$

   where U_{i} is the overall heat transfer coefficient for the i^{th} control volume, α_{hot}, α_{tube}, and α_{cold} are respectively the hot side, the tube wall, and the cold side heat transfer coefficients, and D_o and D_i are respectively the tube outside and inside diameters. The tube wall heat transfer coefficient α_{tube} was obtained from:

$$\alpha_{\text{tube}} = \frac{2 \cdot \lambda_{\text{tube}}}{D_o \cdot \ln\left(\frac{D_o}{D_i}\right)} \tag{5.13}$$

   where λ_{tube} is the tube thermal conductivity (assumed 42 $\text{W m}^{-1}\,\text{K}^{-1}$ for steel [66]).

5. The area of each control volume was then calculated using:

$$A_{\text{i}} = \frac{\dot{Q}_{\text{i}}}{U_{\text{i}} \cdot \Delta T_{\text{lm,i}}} \tag{5.14}$$

where A_i, U_i, $\dot{Q}_i$, and $\Delta T_{lm,i}$ are respectively the heat transfer area based on the tube outside diameter, the overall heat transfer coefficient, the heat transfer rate, and the LMTD for the i^{th} control volume. In the two-phase region, where the heat transfer coefficient is a function of the heat transfer area or the heat flux, the area was computed iteratively.

6. The total heat transfer area for any heat exchanger was the sum of the areas of all its control volumes.

5.4 Solar field

The solar field was modelled for the central receiver and the parabolic trough CSP plants for both design and part-load operation. The common assumptions for the design of the solar field for both the central receiver and the parabolic trough CSP plants are as follows. The location Seville, Spain was assumed in this thesis as several CSP plants have already been built in the region and are currently in operation. The latitude (ϕ), the longitude (ψ), and the standard meridian (ψ_m) for Seville are 37.25 °N, 5.54 °W, and 15 °E, respectively.

For the design value of DNI, it is common to use values between 850 and 950 W m^{-2} [20,134]. Therefore a value of 900 W m^{-2} from this range was assumed in this thesis. For a solar-only plant without storage, the solar multiples (SM) are commonly in the range of 1.15-1.3 for CSP plants in Spain, Morocco, and other countries at similar geographical latitude [10], therefore a value of 1.3 was assumed in this thesis. The design ambient temperature (T_{amb}) was assumed to be 20 °C.

5.4.1 Central receiver

The central receiver solar field includes a number of heliostats with two-axis tracking to follow the sun and concentrate the sunlight on a receiver placed on the top of a tower. For the current study, an external cylindrical receiver with direct vapour generation and a surrounding heliostat field were assumed. Figure 5.6 shows the energy flow for the central receiver solar field and Figure 5.7 highlights the various losses between the energy in the incident DNI and the final heat absorbed by the heat transfer fluid in the receiver. Note that for the direct vapour generation configuration assumed here, the receiver heat transfer fluid is the same as the power cycle working fluid.

In the figures, $\dot{Q}_{sol}$ is the energy in the incident DNI at the plant site while $\dot{Q}_{inc}$ is the energy incident on the receiver surface after the losses due to heliostat reflection, cosine effect, shadowing and blocking, atmospheric attenuation, spillage, and the receiver reflection and absorptivity. These are explained in the description of Equation (5.21). $\dot{Q}_{rec,loss,th}$ accounts for the receiver convective and radiative thermal losses. The energy absorbed by the heat transfer fluid inside the receiver (which is ammonia-water mixture for the direct vapour

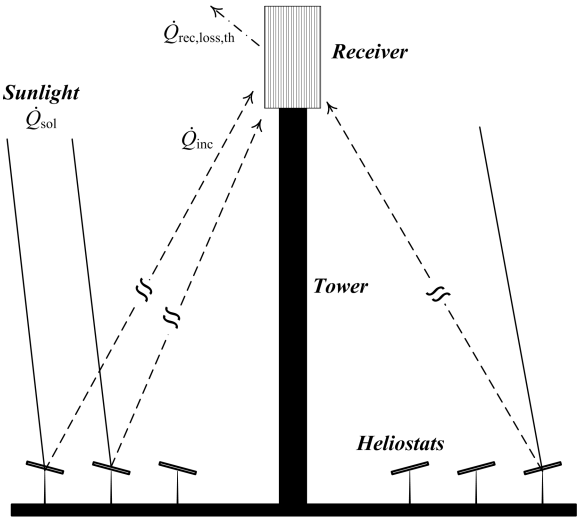

Figure 5.6: Energy flow in the central receiver solar field.

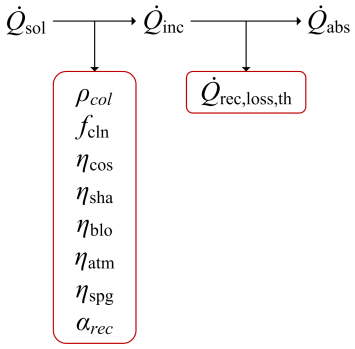

Figure 5.7: Energy loss mechanisms in the central receiver solar field.

generation configuration) is then:

$$\dot{Q}_{abs} = \dot{Q}_{inc} - \dot{Q}_{rec,loss,th} \tag{5.15}$$

where

$$\dot{Q}_{rec,loss,th} = \dot{Q}_{rec,loss,rad} + \dot{Q}_{rec,loss,conv} \tag{5.16}$$

The absorbed energy in the receiver ($\dot{Q}_{abs}$) is equal to the product of the required heat input for the power cycle ($\dot{Q}_{cy,in}$) and the specified solar multiple (SM). The software DELSOL3 [17] by Sandia National Laboratories, USA was used to model the solar field in

design. The radiative losses from the receiver were calculated in DELSOL3 using [20]:

$$\dot{Q}_{\text{rec,loss,rad}} = \epsilon_{rec} \cdot \sigma_{SB} \cdot A_{\text{rec}} \cdot \overline{T}^4_{\text{rec}} \tag{5.17}$$

where ϵ_{rec} is the receiver surface emissivity (assumed 0.90 [20]), σ_{SB} is the Stefan-Boltzmann constant (equal to 5.669×10^{-8} W m^{-2} K^{-4}), and A_{rec} is the receiver surface area. The receiver surface average temperature ($\overline{T}_{\text{rec}}$) in the equation was assumed to be 753 K (480 °C), the default value in DELSOL3 [20]. As the turbine inlet temperature for the power cycle at design point was fixed at 500 °C, it is reasonable to assume an average receiver surface temperature equal to 480 °C, albeit on the conservative side. The convective thermal losses from the receiver were calculated using the following equations [20]:

$$\dot{Q}_{\text{rec,loss,conv}} = \alpha_{\text{conv}} \cdot A_{\text{rec}} \cdot (\overline{T}_{\text{rec}} - T_{\text{amb}}) \tag{5.18}$$

$$\alpha_{\text{conv}} = (\alpha^{3.2}_{\text{for}} + \alpha^{3.2}_{\text{nat}})^{1/3.2} \tag{5.19}$$

where α_{conv} is the overall convective heat transfer coefficient calculated using Equation (5.19) with α_{for} and α_{nat} respectively being the forced and the natural convective heat transfer coefficients. T_{amb} is the design ambient temperature. For the range of receiver diameter in this analysis ($4 \leq D_{\text{rec}} \leq 125$ m), α_{for} and α_{nat} are equal to 14 and 9.09 W m^{-2} K^{-1}, respectively [20]. Once the required heat input to the power cycle (obtained from the power cycle design) was provided to DELSOL3 as an input together with the required solar multiple (SM), the software optimized the receiver dimensions (the height and the diameter), the tower height, and the heliostat field layout by minimizing the energy cost for the given assumptions and bounds. DELSOL3 also provided the required land area for the optimized heliostat field layout as an output.

An example of the input file for DELSOL3 used in this analysis is presented in Appendix D. All the parameters in DELSOL3 were left at their default values, except for the ones mentioned in the input file. The receiver absorptivity is based on the Pyromark paint which is commonly used in contemporary central receiver CSP plants [135]. The overall heliostat reflectivity (0.893) is a product of the mirror reflectivity (ρ_{col}) of 0.94 and an average cleanliness factor (f_{cln}) of 0.95 [135]. The maximum flux limit on the receivers with direct steam generation is typically between 0.35 and 0.8 MW m^{-2} depending on if it is a superheater, an evaporator, or an economizer [136]. Since DELSOL3 allows to specify only one value for the flux limit, an average value of 0.6 MW m^{-2} for the entire receiver was employed in this study.

In order to size the heliostat field, the area around the central tower was divided into radial zones as shown in Figure 5.8. The zones were then filled with heliostats starting near the tower, and moving radially outwards until the required heat input to the power cycle is satisfied. The number of heliostats required, their position (coordinates), the tower height, and the receiver diameter and height were calculated in this way.

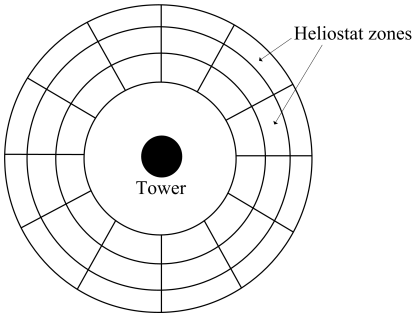

Figure 5.8: Heliostat field design using DELSOL3.

At part-load conditions, the following operation strategy was employed for the solar field. In case there was more heat available than the design heat input to the receiver, some heliostats would be defocused in order to prevent the receiver from operating outside the design conditions. In case the available energy input to the power cycle from the receiver was lower than the minimum power cycle operating point (assumed 20 % of the design rated capacity), the power plant was shut down. Finally, the receiver incident energy ($\dot{Q}_{\text{inc}}$) must obviously always be greater than the receiver thermal loss ($\dot{Q}_{\text{rec,loss,th}}$) for feasible receiver operation. The heat absorbed by the ammonia-water mixture in the receiver during part-load operation was calculated from:

$$\dot{Q}_{\text{abs}} = \text{DNI} \cdot A_{\text{col}} \cdot \eta_{\text{SF}} - \dot{Q}_{\text{rec,loss,th}} \tag{5.20}$$

where the solar field efficiency (η_{SF}) was obtained from:

$$\eta_{\text{SF}} = (\rho_{col} \cdot f_{\text{cln}}) \cdot \eta_{\text{cos}} \cdot \eta_{\text{sha}} \cdot \eta_{\text{blo}} \cdot \eta_{\text{atm}} \cdot \eta_{\text{spg}} \cdot \alpha_{rec} \tag{5.21}$$

In Equations (5.20) and (5.21), A_{col} is the total heliostat field (collector) aperture area obtained from the solar field design using DELSOL3, ρ_{col} is the heliostat mirror reflectivity, f_{cln} is the average mirror cleanliness, α_{rec} is the average receiver absorptivity, and η_{cos} is the field cosine efficiency. The terms η_{sha}, η_{blo}, η_{atm}, and η_{spg} respectively represent the shadowing efficiency (1 – shadowing loss), the blocking efficiency (1 – blocking loss), the atmospheric transmittance (1 – atmospheric attenuation), and the receiver intercept factor (1 – spillage) [20]. As the power cycle operates in part load with the design turbine inlet temperature, the average receiver surface temperature ($\overline{T}_{\text{rec}}$) was conservatively assumed to remain the same at part-load conditions [137]. Assuming the ambient temperature remains near the design value for simplification, the receiver thermal loss ($\dot{Q}_{\text{rec,loss,th}}$) was thus fixed at its design value during part-load operation [137].

The values of the cosine efficiency, the shadowing efficiency, the blocking efficiency, the atmospheric transmittance, and the receiver intercept factor during part-load operation

Table 5.3: Example of a solar field efficiency (η_{SF}) matrix from DELSOL3.

	Zenith angle (θ_z)					
Solar azimuth angle (γ_s)	90°	75°	65°	45°	25°	0°
130°	0.242	0.444	0.517	0.572	0.596	0.618
110°	0.244	0.445	0.518	0.573	0.596	0.618
90°	0.208	0.436	0.518	0.575	0.597	0.618
75°	0.247	0.450	0.521	0.575	0.598	0.618
60°	0.209	0.438	0.521	0.577	0.598	0.618
30°	0.210	0.440	0.524	0.579	0.599	0.618
0°	0.212	0.441	0.525	0.579	0.600	0.618

were calculated in two steps, depending on the sun's position in the sky. The first step was to create a matrix of the solar field efficiency (η_{SF}), including all the efficiencies and factors mentioned in Equation (5.21), from DELSOL3 using the heliostat layout from the design run. This matrix provides the solar field efficiency (η_{SF}) as a function of the solar azimuth (γ_s) and the zenith (θ_z) angles. The second step was to calculate the solar azimuth and the zenith angles for every hour of the year as explained in Section 2.1, and interpolate the solar field efficiency for any hour from the matrix obtained from DELSOL3. In this thesis, the solar angles are calculated at the beginning of every hour for their use in the annual performance calculations.

The solar field efficiency matrix looks like Table 5.3 and the efficiency values include effects of the heliostat reflectivity, the heliostat cleanliness, the cosine efficiency, the shadowing efficiency, the blocking efficiency, the atmospheric transmittance, the receiver intercept factor, and the receiver absorptivity as indicated in Equation (5.21). It is not possible to practically operate with zenith angles equal to 90° as that would mean the sun is at the horizon, and therefore any angles greater than 90° are not included in the table. The DELSOL3 input code used to obtain this matrix is shown in Appendix D. This code is run after the solar field has already been designed from a previous DELSOL3 design run. In other words, the first software run is used to design the solar field using the required heat input to the power cycle as a design input. Once the solar field is designed, the software is run for a second time to obtain the solar field efficiency matrix for part-load operation, with the field design parameters from the first run as the input.

5.4.2 Parabolic trough

The parabolic trough solar field design process is very different from the central receiver solar field design process. A parabolic trough solar field consists of a number of parabolic trough collector assemblies (or just 'collectors' in short) connected in series and parallel with the receiver tubes passing through the focal line of the troughs. Figure 5.9 shows a schematic of a parabolic trough solar field. In the figure, the thick 'blue' lines, representing

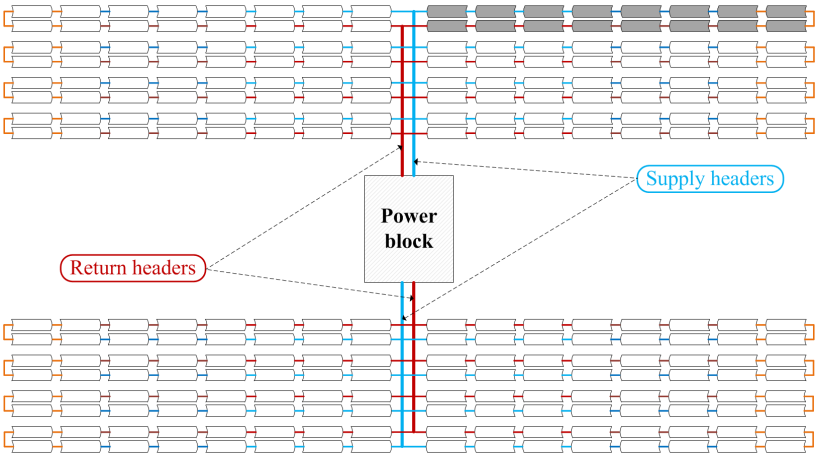

Figure 5.9: Schematic of a parabolic trough CSP plant without storage.

the flow of the cold heat transfer fluid from the boiler in the power block to the collectors, are referred to as the supply headers. The thick 'red' lines, representing the flow of the hot heat transfer fluid from the collectors to the boiler, are referred to as the return headers.

The shaded group of collectors represents one *collector loop*. Every such loop is connected to the supply header at the inlet of the loop and to the return header at the outlet. This implies that the performance of every loop in terms of the pressure drop and the temperature rise is nearly the same, if the respective mass flow rates through them are equal. Several such loops are connected in parallel to distribute the total heat transfer fluid mass flow rate into practically operable values depending on the flow velocity limits inside the receiver tubes. In this study, the parabolic trough solar field was designed following the guidelines from the commercial SEGS VI CSP plant [18,114,115] as the rated capacity of the SEGS VI CSP plant (30 MW) is comparable to the one considered here (20 MW). The key assumptions used in the design of the parabolic trough solar field are listed in Table 5.4.

Using the required heat input for the power cycle at design ($\dot{Q}_{\mathrm{cy,in,d}}$) and the specified solar multiple (SM) to oversize the solar field, the required aperture area for the parabolic trough solar field (A_{col}) was calculated using:

$$A_{\mathrm{col}} = \frac{\dot{Q}_{\mathrm{SF}}}{\mathrm{DNI} \cdot \cos\theta \cdot \eta_{\mathrm{SF}} \cdot \mathrm{IAM} - U_{\mathrm{loss}} \cdot (\overline{T}_{\mathrm{htf}} - T_{\mathrm{amb}})} \tag{5.22}$$

where the required heat output from the solar field ($\dot{Q}_{\mathrm{SF}}$) at the design point is the product of the solar multiple (SM) and the required design point power cycle heat input ($\dot{Q}_{\mathrm{cy,in,d}}$). $\overline{T}_{\mathrm{htf}}$ is the average of the solar field heat transfer fluid inlet and outlet temperatures while θ is the incidence angle at noon of June 21 calculated using the zenith angle (θ_z), the

Table 5.4: Parabolic trough solar field design assumptions [10,18,114,115,138].

Parameter	Symbol	Value
Design point	-	21 June at noon
Collector model	-	Luz LS-2
Receiver tube model	-	Schott PTR70 2008
Collector length	L_{col}	49 m
Collector width	W_{col}	5 m
Collector focal length	F_{col}	1.49 m
Collector spacing	$L_{\text{col,spa}}$	15 m
Solar field heat loss coefficient	U_{loss}	0.1 $\text{W m}^{-2}\,\text{K}^{-1}$
Solar field heat transfer fluid	-	Therminol VP-1
Solar field fluid outlet temperature	$T_{\text{htf,1}}$	390 °C
Number of collectors in one loop	$N_{\text{col,loop}}$	16

declination angle (δ), and the hour angle (ω) with the following equation [21]:

$$\cos\theta = \sqrt{\cos^2\theta_z + \cos^2\delta \cdot \sin^2\omega} \tag{5.23}$$

Once the collector field aperture area (A_{col}) is fixed from the design calculations, Equation (5.22) was later used to calculate the energy output from the solar field ($\dot{Q}_{\text{SF}}$) for the hourly simulations for the annual performance calculations, using the incident DNI known from the meteorological data for the plant site. The incidence angle modifier (IAM) in Equation (5.22) for the Luz LS-2 parabolic trough collector model was calculated by [115]:

$$\text{IAM} = 1 + \frac{8.84\times10^{-4}\cdot\theta}{\cos\theta} - \frac{5.369\times10^{-5}\cdot\theta^2}{\cos\theta} \tag{5.24}$$

The parabolic trough solar field efficiency (η_{SF}) in Equation (5.22) was estimated by [115]:

$$\eta_{\text{SF}} = \eta_{\text{col}}\cdot\eta_{\text{rec}}\cdot\eta_{\text{sha}}\cdot f_{\text{end}} \tag{5.25}$$

while neglecting the effect of the solar field availability for simplification. The optical efficiency for the collector (η_{col}), the receiver efficiency (η_{rec}), the shadowing efficiency (η_{sha}), and the end loss factor (f_{end}) were calculated using the following equations [18,115]:

$$\eta_{\text{col}} = f_{\text{trk}}\cdot f_{\text{geo}}\cdot\rho_{col}\cdot f_{\text{cln}} \tag{5.26}$$

$$\eta_{\text{rec}} = f_{\text{dst}}\cdot f_{\text{bel}}\cdot f_{\text{gls}}\cdot f_{\text{abs}} \tag{5.27}$$

$$\eta_{\text{sha}} = \frac{L_{\text{col,spa}}}{W_{\text{col}}}\cdot\frac{\cos\theta_z}{\cos\theta} \tag{5.28}$$

$$f_{\text{end}} = 1 - \frac{F_{\text{col}}\cdot\tan\theta}{L_{\text{col}}} \tag{5.29}$$

where the different parameters used in the above equations are elaborated in Table 5.5.

Table 5.5: Parameters used in calculating the parabolic trough solar field efficiency [18,114,115].

Parameter	Symbol	Value
Collector		
Tracking and twisting error factor	f_{trk}	0.99
Geometric accuracy of the collector mirrors	f_{geo}	0.98
Mirror reflectivity	ρ_{col}	0.935
Average mirror cleanliness	f_{cln}	0.95
Receiver		
Dust losses factor	f_{dst}	0.98
Bellows shadowing factor	f_{bel}	0.963
Glass envelope transmissivity factor	f_{gls}	0.963
Absorber absorption factor	f_{abs}	0.96

In order to obtain the parabolic trough solar field output during part-load operation, Equations (5.22) to (5.29) were used but with the updated values of the solar angles calculated at the beginning of every hour for the annual performance simulation. For simplification, the heat loss to the ambient was assumed to remain constant at the design value as a conservative assumption.

5.5 Steam Rankine cycle

As the steam Rankine cycle based CSP plants have already been in commercial operation for several years, it was decided to compare the Kalina cycle CSP plants with the state-of-the-art steam Rankine cycle CSP plants. For this reason, an established software in the CSP industry, System Advisor Model 2015.6.30 [18] by the National Renewable Energy Laboratory, USA, was used to model the steam Rankine cycle CSP plants. The software is available to download for free and includes the details of the various plant components. For a fair comparison, the same assumptions were made for the steam Rankine cycle simulations as for the Kalina cycle CSP plants (as mentioned in Table 5.1 and Section 5.4). The 'uniform dispatch' option was selected for the time of delivery factor scheduling. The site meteorological data was read from the same weather file as used in the Kalina cycle simulations.

For the central receiver CSP plant, the model 'CSP power tower direct steam' was selected. The heliostat mirror and other solar field specifications were the same as used in DELSOL3 (as mentioned in Section 5.4.1). The steam Rankine cycle design point efficiency was assumed to be 38.7 % as suggested by DLR German Aerospace Center [139] for tower plants. For the parabolic trough CSP plant, the model 'CSP parabolic trough (physical)' was selected. The collector model, the receiver model, and the solar field layout options for the parabolic trough plants were modified to match the assumptions made for the Kalina cycle simulations (as mentioned in Table 5.4). The power cycle design efficiency was modified to 32 % as

suggested in Suresh et al. [140] for a 20 MW parabolic trough CSP plant with steam Rankine cycle. The solar field inlet and outlet temperatures were set to 290 °C and 390 °C as per the state-of-the-art parabolic trough CSP plants with steam Rankine cycles [10].

5.6 Cost functions

The cost functions used to estimate the capital investment and the O&M costs are presented in this section. In order to consider the effect of inflation since the cost functions were first published, all the capital investment costs were scaled by the Marshall and Swift equipment cost indices to represent all the costs in January 2014 values [141], except for the ones taken from NREL [18] as they were already from a 2015 version of the software, and therefore maintained at the current values as a conservative assumption. The cost scaling was done by multiplying the cost obtained from the cost function by the ratio of the Marshall and Swift equipment cost index from January 2014, to that of the year when the cost function was first published. An example is shown in Equation (5.30). For brevity, all the capital cost functions are mentioned here without the equipment cost index ratio multiplication factor.

$$C = C_{\mathrm{CF}} \cdot \frac{f_{\mathrm{M\&S}}^{2014}}{f_{\mathrm{M\&S}}^{\mathrm{CF,y}}} \tag{5.30}$$

where C is the January 2014 cost, C_{CF} is the cost estimated using the cost function, and $f_{\mathrm{M\&S}}^{2014}$ and $f_{\mathrm{M\&S}}^{\mathrm{CF}}$ are the Marshall and Swift cost indices respectively for January 2014 and the year in which the cost function was first published.

The total capital investment cost (C_{inv}) for the Kalina cycle CSP plant was estimated as the sum of the power cycle cost (C_{PC}), the solar field cost (C_{SF}), the land purchasing cost (C_{land}), and the contingencies over these three costs (C_{cnt}) as shown below:

$$C_{\mathrm{inv}} = C_{\mathrm{PC}} + C_{\mathrm{SF}} + C_{\mathrm{land}} + C_{\mathrm{cnt}} \tag{5.31}$$

The power cycle cost was calculated using Equation (5.32) as the sum of the equipment cost ($C_{\mathrm{PC,eqp}}$) and the miscellaneous cost ($C_{\mathrm{PC,misc}}$). The equipment cost ($C_{\mathrm{PC,eqp}}$) consisted of the capital investment cost for the turbine (C_{tur}), the generator (C_{gen}), the pumps (C_{pu}), the heat exchangers – recuperators (C_{re}) and condensers (C_{cd}), and the vapour-liquid separator (C_{sep}) for a central receiver CSP plant, as shown in Equation (5.33). For a parabolic trough CSP plant, the cost of the boiler (C_{blr}), which is the sum of the costs of the superheater, the evaporator, and the economizer, was also added to the power cycle equipment cost. The miscellaneous cost ($C_{\mathrm{PC,misc}}$) included the piping cost ($C_{\mathrm{PC,pip}}$), the instrumentation and control system cost ($C_{\mathrm{PC,insc}}$), the electrical equipment and materials cost ($C_{\mathrm{PC,el}}$), and the installation cost ($C_{\mathrm{PC,inst}}$), as shown in Equation (5.34).

$$C_{PC} = C_{PC,eqp} + C_{PC,misc} \tag{5.32}$$

$$C_{PC,eqp} = C_{tur} + C_{gen} + \sum C_{pu} + \sum C_{re} + \sum C_{cd} + C_{sep} + C_{blr} \tag{5.33}$$

$$C_{PC,misc} = C_{PC,pip} + C_{PC,insc} + C_{PC,el} + C_{PC,inst} \tag{5.34}$$

The Kalina cycle turbine and pump costs were estimated with the turbine power output ($\dot{W}_{tur}$) and the required pump power ($\dot{W}_{pu}$) in kW with [142]:

$$C_{tur} = 4405 \cdot \dot{W}_{tur}^{0.7} \tag{5.35}$$

$$C_{pu} = 1120 \cdot \dot{W}_{pu}^{0.7} \tag{5.36}$$

The cost of the generator and electrical auxiliaries was estimated with the generator electrical power output ($\dot{W}_{gen}$) in kW with [143]:

$$C_{gen} = 10 \times 10^6 \cdot \left(\frac{\dot{W}_{gen}}{160 \times 10^3} \right)^{0.7} \tag{5.37}$$

All the heat exchangers in this study were assumed to be shell-and-tube type, the cost of which were estimated based on the heat transfer area (A_{hx}) using the following correlation [127]:

$$C_{hx} = 32800 \cdot \left(\frac{A_{hx}}{80} \right)^{0.8} \cdot f_{pres} \cdot f_{temp} \tag{5.38}$$

where the pressure (f_{pres}) and the temperature (f_{temp}) correction factors were calculated as suggested in Smith [127]. The heat transfer area was estimated from the heat exchanger model presented in Section 5.3.2.

The separator cost (C_{sep}) was estimated assuming it to be a vertical vessel [144,145]:

$$C_{sep} = f_{pres} \cdot 10^{f_{s1} + f_{s2} \cdot \log_{10} H_{sep} + f_{s3} \cdot (\log_{10} H_{sep})^2} \tag{5.39}$$

where the height of the separator (H_{sep}) was calculated using the volumetric flow rate at the separator inlet assuming a residence time of 3 min and a height to diameter ratio equal to 3, common specification assumptions in commercial models [146]. The pressure correction factor (f_{pres}) was calculated as suggested in Ulrich [144]. The values of the factors f_{s1}, f_{s2},

and f_{s3} are chosen based on the separator diameter (D_{sep}):

$$\begin{aligned}
\{f_{s1},\ f_{s2},\ f_{s3}\} &= \{3.3392, 0.5538, 0.2851\} && D_{sep} \leq 0.3 \text{ m} \\
&= \{3.4746, 0.5893, 0.2053\} && 0.3 < D_{sep} \leq 0.5 \text{ m} \\
&= \{3.6237, 0.5262, 0.2146\} && 0.5 < D_{sep} \leq 1.0 \text{ m} \\
&= \{3.7559, 0.6361, 0.1069\} && 1.0 < D_{sep} \leq 1.5 \text{ m} \\
&= \{3.9484, 0.4623, 0.1717\} && 1.5 < D_{sep} \leq 2.0 \text{ m} \\
&= \{4.0547, 0.4620, 0.1558\} && 2.0 < D_{sep} \leq 2.5 \text{ m} \\
&= \{4.1110, 0.6094, 0.0490\} && 2.5 < D_{sep} \leq 3.0 \text{ m} \\
&= \{4.3919, 0.2859, 0.1842\} && D_{sep} > 3.0 \text{ m}
\end{aligned} \tag{5.40}$$

The piping cost ($C_{PC,pip}$), the instrumentation and control system cost ($C_{PC,insc}$), the electrical equipment and material cost ($C_{PC,el}$), and the installation cost ($C_{PC,inst}$) were respectively 66 %, 10 %, 10 %, and 45 % of the power cycle equipment costs ($C_{PC,eqp}$) as suggested in Bejan et al. [147].

For the **central receiver CSP plant**, the total solar field cost (C_{SF}) included the cost of the heliostat mirror collectors (C_{col}), the tower (C_{tow}), the receiver (C_{rec}), and site improvement (C_{site}) given by the following equations [18]:

$$C_{SF} = C_{col} + C_{tow} + C_{rec} + C_{site} \tag{5.41}$$

$$C_{col} = 170 \cdot A_{col} \tag{5.42}$$

$$C_{tow} = 3 \times 10^6 \cdot \exp\left[0.0113 \cdot \left(\frac{H_{tow} - H_{rec}}{2} + \frac{H_{col}}{2}\right)\right] \tag{5.43}$$

$$C_{rec} = 55402800 \cdot \left(\frac{\pi \cdot D_{rec} \cdot H_{rec}}{1110}\right)^{0.7} \tag{5.44}$$

$$C_{site} = 15 \cdot A_{col} \tag{5.45}$$

where A_{col} is the heliostat field total aperture area, H_{tow}, H_{rec}, and H_{col} are respectively the tower height, the receiver height, and the heliostat mirror height, and D_{rec} is the receiver diameter.

For the **parabolic trough CSP plant**, the total solar field cost (C_{SF}) included the cost of the parabolic trough solar field with the collectors, receivers, and auxiliaries (C_{pt}), the heat transfer fluid systems with the required pumps, field headers, and piping (C_{htf}), and the cost for site improvement (C_{site}). These were estimated using the collector aperture area (A_{col})

with the following equations [18]:

$$C_{SF} = C_{pt} + C_{htf} + C_{site} \tag{5.46}$$

$$C_{pt} = 270 \cdot A_{col} \tag{5.47}$$

$$C_{htf} = 80 \cdot A_{col} \tag{5.48}$$

$$C_{site} = 30 \cdot A_{col} \tag{5.49}$$

The capital investment cost for the state-of-the-art steam Rankine power cycle was assumed to be $ 1200 per kW of the gross power output as suggested by NREL [18]. The yearly O&M cost ($C_{O\&M,y}$) for both the Kalina and the steam Rankine cycles was the sum of the fixed and the variable components. The yearly fixed O&M cost for the central receiver and the parabolic trough CSP plants was respectively $ 50 and $ 65 per kW of the rated plant capacity [18]. The variable O&M cost factor for both the central receiver and parabolic trough CSP plants was $ 4 per MWh of the generated electricity [18]. The land purchasing cost (C_{land}) for both the Kalina and the steam Rankine cycles was assumed to be $ 10000 per acre [18], where 1 acre is 4046.825 m^2. The required land area (A_{land}) for the central receiver CSP plant was obtained from the design DELSOL3 run. For the parabolic trough CSP plant, the land area was calculated using the collector aperture area (A_{col}), the collector spacing ($L_{col,spa}$), and the collector width (W_{col}) in the following equation [18]:

$$A_{land} = 1.4 \cdot \frac{A_{col} \cdot L_{col,spa}}{W_{col}} \tag{5.50}$$

The contingency cost (C_{cnt}) was assumed to be 20 % of the sum of the capital investment costs for the solar field, the power cycle, and the required land as suggested in the ECOSTAR report [119]:

$$C_{cnt} = 0.2 \cdot (C_{PC} + C_{SF} + C_{land}) \tag{5.51}$$

5.7 Results

The results from the thermoeconomic optimization are presented for both the central receiver and the parabolic trough CSP plants with the Kalina cycle KC12. The part-load performance curves are presented first, followed by the key cycle operation parameters and LCOE values from the optimization.

5.7.1 Part-load performance

The decision variables for the optimal part-load performance solutions for a **central receiver CSP plant** for an exemplary case are shown in Table 5.6. In the table, ζ_{pl} is the *relative plant*

Table 5.6: Decision variable values for the optimal part-load solutions for a turbine inlet ammonia mass fraction of 0.6 for a central receiver CSP plant.

ζ_{pl}	p_1 (bar)	T_{10} (°C)	x_{10}
1.000	100	70.00	0.4037
0.899	89.64	66.60	0.4029
0.791	79.95	67.60	0.4021
0.683	70.30	68.50	0.4020
0.575	60.70	69.65	0.4028
0.468	50.96	66.60	0.4005

load, i.e. the ratio of the cycle net electrical power output in part load to that at the design point. From Table 5.6, it may be observed that the turbine inlet pressure varies almost linearly with the change in the plant load because of the use of sliding pressure control strategy for part-load operation while maintaining the turbine inlet temperature at the design value. The separator inlet temperature and ammonia mass fraction are maintained at near-design values for a smooth transition between the different part-load conditions. The separator inlet ammonia mass fraction increases with increasing plant load, while the separator inlet temperature decreases. There is however a change in the separator inlet temperature trend at the lowest load, whereas the trend in the separator inlet ammonia mass fraction exhibits an anomaly at the second lowest load. These anomalies were experienced because it was not possible for the optimization algorithm to find a better solution for these loads due to convergence failures from the thermodynamic property calculations. As the part-load operation is within a small range of the separator inlet ammonia mass fraction values, it is not expected for these anomalies to have a significant impact on the final results. It may also be observed that the gap between the relative plant load value and the turbine inlet pressure widens at lower loads. This is because the separator inlet ammonia mass fraction is limited to ±1 % variation from the design value, and it restricts the turbine inlet pressure from going below a certain value in order to avoid pinch violation in the recuperator RE1.

Figure 5.10 shows the part-load performance curves for different turbine inlet ammonia mass fractions for the central receiver CSP plant. In the figure, the *relative cycle efficiency* is the ratio of the cycle efficiency in part load to that at the design point. The basis of the part-load performances shown here are the cycle design efficiencies shown in Figure 4.7. The equations for the part-load curves in Figure 5.10 for the central receiver CSP plant were generated using the Curve Fitting Toolbox of MATLAB. These are shown in Table 5.7. The equations were fitted with polynomial fitting option and a robust least-squares fitting method (Least Absolute Residuals or LAR), both standard options in the toolbox. In the equations, ζ_{pl} is the relative plant load. All the equations have a coefficient of determination (R^2) greater than 0.997.

The part-load performance curves show a decreasing performance with the decreasing plant load. It may be observed that the part-load performance at the higher plant loads

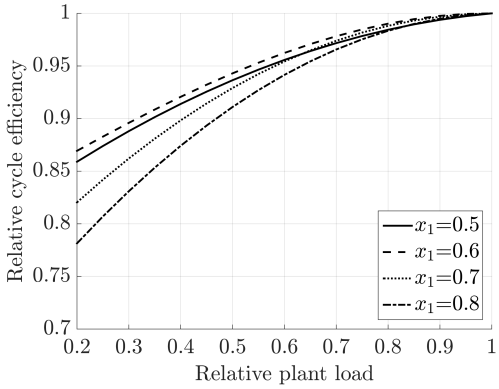

Figure 5.10: Part-load relative cycle efficiency for a central receiver CSP plant with Kalina cycle KC12.

Table 5.7: Part-load relative cycle efficiency as a function of the relative plant load for a central receiver CSP plant with Kalina cycle KC12.

x_1	Part-load relative cycle efficiency
0.5	$-0.1641 \cdot \zeta_{pl}^2 + 0.3732 \cdot \zeta_{pl} + 0.7909$
0.6	$-0.08693 \cdot \zeta_{pl}^3 - 0.01653 \cdot \zeta_{pl}^2 + 0.291 \cdot \zeta_{pl} + 0.8125$
0.7	$-0.2757 \cdot \zeta_{pl}^2 + 0.5554 \cdot \zeta_{pl} + 0.7203$
0.8	$-0.3175 \cdot \zeta_{pl}^2 + 0.6542 \cdot \zeta_{pl} + 0.6633$

(above 90 %) is almost the same for all the turbine inlet ammonia mass fractions because of operating close to the design point. However, the trends of the performance curves differ when going towards lower plant loads. The part-load performance of the cycle with higher values of turbine inlet ammonia mass fraction (0.7 and above) decreases more rapidly with decreasing plant load as compared with the lower values of the turbine inlet ammonia mass fraction. This is because of the significant differences in the basic solution ammonia mass fraction (stream 5 in Figure 4.1), and therefore the condensing pressures. For example, the condenser CD1 pressure (also the turbine outlet pressure) at 50 % relative heat input for turbine inlet ammonia mass fractions of 0.6 and 0.8 is respectively 1.70 bar and 5.56 bar, whereas the turbine inlet pressures for the two cases are nearly the same at 50.96 bar and 52.85 bar, respectively. This results in less expansion in the turbine at low plant loads for a turbine inlet ammonia mass fraction of 0.8, resulting in a lower part-load efficiency for the same relative heat input.

A higher working solution ammonia mass fraction requires a higher basic solution ammonia mass fraction for feasible operation of the Kalina cycle. Consequently, a higher value of the basic solution ammonia mass fraction results in a higher condensing pressure. In fact this is the reason to have a distillation-condensation subsystem in the first place – to reduce the ammonia mass fraction in the condenser CD1 so that the working solution in the turbine can

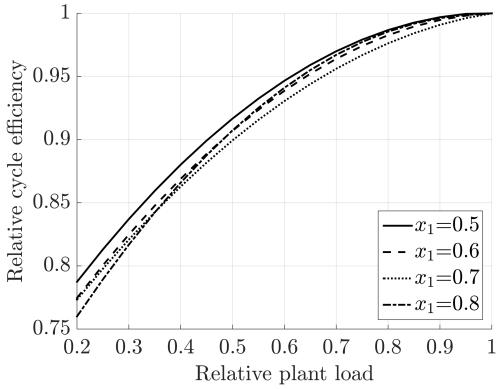

Figure 5.11: Part-load relative cycle efficiency for a parabolic trough CSP plant with Kalina cycle KC12.

Table 5.8: Part-load relative cycle efficiency as a function of the relative plant load for a parabolic trough CSP plant with Kalina cycle KC12.

x_1	Part-load relative cycle efficiency
0.5	$-0.3290 \cdot \zeta_{pl}^2 + 0.6613 \cdot \zeta_{pl} + 0.6683$
0.6	$-0.02349 \cdot \zeta_{pl}^3 - 0.27910 \cdot \zeta_{pl}^2 + 0.64560 \cdot \zeta_{pl} + 0.65690$
0.7	$-0.2740 \cdot \zeta_{pl}^2 + 0.6123 \cdot \zeta_{pl} + 0.6618$
0.8	$-0.3840 \cdot \zeta_{pl}^2 + 0.7599 \cdot \zeta_{pl} + 0.6234$

be expanded to lower pressures. Therefore, even though a higher working solution ammonia mass fraction might result in a higher design point efficiency because of more effective recuperation and condensation [60], it might also result in lower part-load performance at low plant loads because of a larger relative reduction in the turbine inlet pressure than the corresponding turbine outlet pressure relative reduction.

The part-load performance curves for the **parabolic trough CSP plant** with the Kalina cycle KC12 were prepared in a similar way and are shown in Figure 5.11. The part-load performance curves for the parabolic trough CSP plant also show a decreasing relative cycle efficiency with decreasing relative plant load, similar to the curves for the central receiver CSP plant. However, all the curves for the different turbine inlet ammonia mass fractions follow nearly the same trend for the entire range of plant loads. The higher values of the turbine inlet ammonia mass fractions still show a worse performance at lower plant loads as compared with the lower values, same as in the case of the central receiver CSP plant, though the gap is not as wide. This is because the part-load performance of the parabolic trough CSP plant is governed mainly by the boiler pinch violation consideration, and not the turbine outlet pressure as was the case with the central receiver CSP plant. This means that in order to satisfy the pinch point constraints for the boiler and the recuperator RE1 simultaneously, the turbine inlet pressure was further limited to operate in a much narrower

range for feasible part-load operation. Moreover, the presence of an additional parasitic consumer by means of the heat transfer fluid pump and a lower turbine inlet temperature further reduce the plant performance at lower loads. Table 5.8 lists the fitted equations for part-load performance curves shown in Figure 5.11. All the equations have a coefficient of determination (R^2) greater than 0.997.

5.7.2 Optimization

Table 5.9 shows the main results from the thermoeconomic optimization of the **central receiver CSP plant** with the Kalina cycle KC12. The results suggest that the LCOE is more sensitive to the turbine inlet pressure than to the turbine inlet ammonia mass fraction. All the combinations of the turbine inlet pressures and ammonia mass fractions result in a close range of LCOE values, between 212.2 $\$\,MWh^{-1}$ and 218.9 $\$\,MWh^{-1}$. This is because of the large share of the solar field in the capital cost which governs the overall cost structure of the plant. The specific investment cost ($\widehat{C}_{inv}$) for the different Kalina cycle cases is between 5322.7 $\$\,kW^{-1}$ and 5559.8 $\$\,kW^{-1}$. For a similar plant, the state-of-the-art steam Rankine cycle had an LCOE equal to 181.0 $\$\,MWh^{-1}$ with the plant specific investment cost ($\widehat{C}_{inv}$) equal to 4822.3 $\$\,kW^{-1}$.

Table 5.9: Thermoeconomic optimization results for the Kalina cycle central receiver CSP plant with a turbine inlet temperature of 500 °C.

x_1	p_1 (bar)	η_{cy} (%)	$\widehat{C}_{inv}$ ($\$\,kW^{-1}$)	$\widehat{C}_{SF}$ ($\$\,kW^{-1}$)	$\widehat{C}_{PC}$ ($\$\,kW^{-1}$)	LCOE ($\$\,MWh^{-1}$)
0.5	100	28.58	5427.3	2860.8	1447.9	214.6
	120	28.67	5380.3	2855.5	1414.6	213.5
	140	28.58	5359.8	2860.8	1391.7	212.2
0.6	100	28.61	5559.8	2859.0	1560.3	218.9
	120	28.60	5482.2	2859.0	1495.6	216.2
	140	28.59	5428.7	2859.9	1450.1	214.2
0.7	100	28.58	5530.0	2860.8	1533.5	218.9
	120	29.28	5463.8	2819.3	1524.1	219.1
	140	30.20	5445.3	2768.9	1564.1	217.5
0.8	100	29.97	5432.3	2781.3	1539.7	218.8
	120	30.65	5372.6	2745.1	1529.7	216.0
	140	30.88	5322.7	2732.7	1501.7	214.1

The specific capital investment cost for the power cycle ($\widehat{C}_{PC}$) shows a decreasing trend with the increasing turbine inlet pressure for the different turbine inlet ammonia mass fractions. The specific investment cost for the solar field ($\widehat{C}_{SF}$) remains nearly the same for lower values of the turbine inlet ammonia mass fraction, whereas it shows a decreasing trend for its higher values. The solar field specific investment cost ($\widehat{C}_{SF}$) is directly related

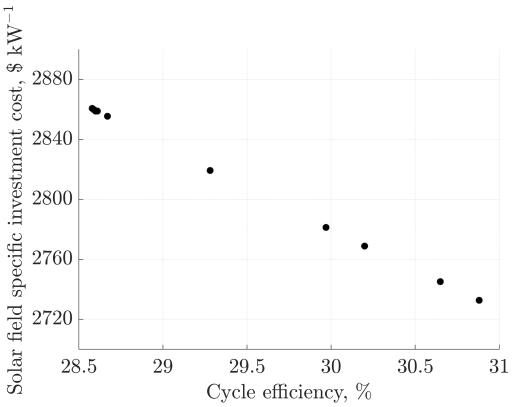

Figure 5.12: Solar field specific investment cost ($\widehat{C}_{SF}$) as a function of the power cycle efficiency (η_{cy}) for Kalina cycle central receiver CSP plant for all the simulated cases.

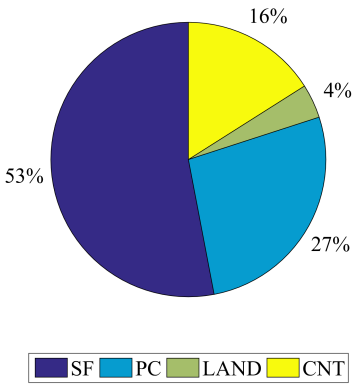

Figure 5.13: Capital cost breakdown for the Kalina cycle central receiver CSP plant for a turbine inlet pressure and ammonia mass fraction of 100 bar and 0.5.

to the power cycle efficiency. A cycle with a lower efficiency requires a higher heat input for the same net electrical power output. This required heat input then governs the solar field design and consequently the capital investment cost. This trend may be observed by comparing the respective power cycle efficiency (η_{cy}) and the solar field specific investment cost ($\widehat{C}_{SF}$) values, and is shown in Figure 5.12 for all the simulated combinations of turbine inlet pressures and ammonia mass fractions as listed in Table 5.9.

Figure 5.13 shows an exemplary breakdown of the total capital investment cost (C_{inv}) for a turbine inlet pressure and ammonia mass fraction of 100 bar and 0.5. The other combinations of the turbine inlet pressures and ammonia mass fractions exhibit a similar trend. In the figure, 'SF' represents the solar field capital investment cost (C_{SF}), 'PC' represents the power cycle capital investment cost (C_{PC}), 'LAND' represents the land purchase cost (C_{land}), and

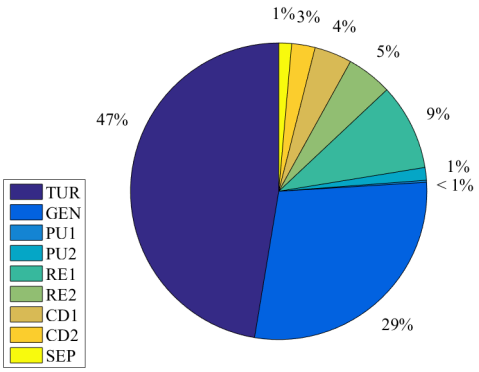

Figure 5.14: Capital investment cost for the power cycle equipment for the Kalina cycle central receiver CSP plant for a turbine inlet pressure and ammonia mass fraction of 100 bar and 0.5.

Table 5.10: LCOE breakdown for the Kalina cycle central receiver CSP plant for a turbine inlet pressure and ammonia mass fraction of 100 bar and 0.5.

LCOE component	Value ($\$\,MWh^{-1}$)	Share in LCOE (%)
Solar field capital investment cost	101.5	47.3
Power cycle equipment capital investment cost	22.2	10.4
Power cycle miscellaneous investment cost	29.2	13.6
Land purchasing cost	7.6	3.5
Contingency	32.1	14.9
Fixed O&M cost	18.0	8.4
Variable O&M cost	4.0	1.9
Total	214.6	100

'CNT' represents the contingencies (C_{cnt}). Figure 5.14 shows the breakdown of the capital investment cost for the power cycle equipment ($C_{PC,eqp}$) for the same case as in Figure 5.13. The turbine and the generator occupy the largest share of the power cycle equipment investment cost, followed by the recuperators, the condensers, the pumps, and finally the separator. The relatively larger share of the recuperator RE1 among the heat exchangers is because of the pressure and temperature factors used to scale the heat exchanger investment cost. The recuperator RE1 is the only heat exchanger in the central receiver CSP plant which operates with high pressure on the tube side and relatively higher temperatures than the other three heat exchangers (the recuperator RE2, and the condensers CD1 and CD2). Table 5.10 shows the share of the various costs in the optimal LCOE for the Kalina cycle with a turbine inlet pressure and ammonia mass fraction of 100 bar and 0.5. The solar field capital investment cost has clearly the highest share in the LCOE, followed by the power cycle total investment cost (equipment plus the miscellaneous expenses). The contingency costs have a significant share because the contingency is calculated on the sum of the capital investment cost for the solar field, the power cycle, and the land.

Table 5.11: Thermoeconomic optimization results for the Kalina cycle parabolic trough CSP plant with a turbine inlet temperature of 370 °C.

x_1	p_1 (bar)	η_{cy} (%)	$\widehat{C}_{inv}$ ($\$\,kW^{-1}$)	$\widehat{C}_{SF}$ ($\$\,kW^{-1}$)	$\widehat{C}_{PC}$ ($\$\,kW^{-1}$)	LCOE ($\$\,MWh^{-1}$)
0.5	80	25.65	5838.0	2978.8	1804.9	270.8
	90	25.84	5797.2	2956.5	1793.7	269.1
	100	26.19	5782.6	2919.5	1819.6	268.7
0.6	80	25.21	5966.7	3029.0	1860.5	277.5
	90	25.68	5923.4	2974.8	1880.1	275.8
	100	26.06	5889.5	2932.0	1895.8	274.5
0.7	80	24.37	6038.7	3133.9	1812.8	281.7
	90	24.89	5972.7	3068.9	1824.5	278.9
	100	25.37	5923.0	3010.1	1843.5	276.9
0.8	80	24.03	6037.9	3180.2	1764.5	281.0
	90	24.52	5974.0	3116.4	1776.8	278.3
	100	24.89	5919.8	3068.2	1781.2	276.0

Table 5.11 shows the main results from the thermoeconomic optimization of the **parabolic trough CSP plant** with the Kalina cycle KC12. The results for the parabolic trough CSP plant indicate a slightly different trend from the central receiver CSP plant results. The results suggest that the LCOE is more sensitive to the turbine inlet ammonia mass fraction than the turbine inlet pressure, unlike in the case of the central receiver CSP plant. This is because of the addition of the boiler where the working solution ammonia mass fraction significantly affects the heat transfer performance, and therefore the investment cost. All the combinations of the turbine inlet pressures and ammonia mass fractions nevertheless still result in a close range of LCOE values, between 268.7 $\$\,MWh^{-1}$ and 281.7 $\$\,MWh^{-1}$. This is again because the large share of the solar field in the capital cost. The specific investment cost ($\widehat{C}_{inv}$) for the different cases is between 5782.6 $\$\,kW^{-1}$ and 6038.7 $\$\,kW^{-1}$. For a similar plant, the state-of-the-art steam Rankine cycle had an LCOE equal to 202.5 $\$\,MWh^{-1}$ with the plant specific investment cost ($\widehat{C}_{inv}$) equal to 5008.4 $\$\,kW^{-1}$.

The specific capital investment cost for the power cycle ($\widehat{C}_{PC}$) exhibits an increasing trend with the increasing turbine inlet pressure whereas the specific investment cost for the solar field ($\widehat{C}_{SF}$) exhibits a decreasing trend for all the turbine inlet ammonia mass fractions. Since a boiler is now a part of the power cycle costs, there are more heat exchangers working with high pressure and temperature than in the central receiver CSP plant. Therefore, the increase in turbine inlet pressure results in an overall increase in the power cycle specific investment cost ($\widehat{C}_{PC}$). The solar field specific investment cost ($\widehat{C}_{SF}$) is again related directly to the power cycle efficiency (η_{cy}). This relation may be observed by comparing the respective values for the two quantities, and is shown in Figure 5.15 for all the simulated combinations of turbine inlet pressures and ammonia mass fractions as listed in Table 5.11.

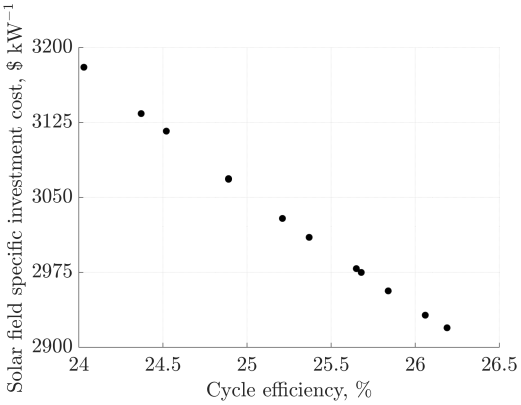

Figure 5.15: Solar field specific investment cost ($\widehat{C}_{SF}$) as a function of the power cycle efficiency (η_{cy}) for Kalina cycle parabolic trough CSP plant for all the simulated cases.

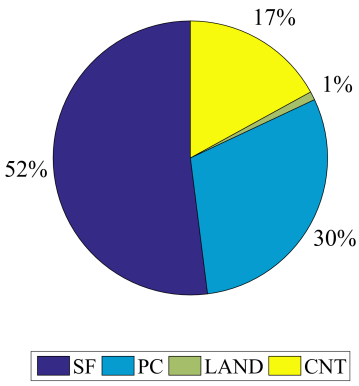

Figure 5.16: Capital cost breakdown for the Kalina cycle parabolic trough CSP plant for a turbine inlet pressure and ammonia mass fraction of 100 bar and 0.5.

Figure 5.16 shows an exemplary breakdown of the total capital investment cost (C_{inv}) for a turbine inlet pressure and ammonia mass fraction of 100 bar and 0.5. In the figure, 'SF' represents the solar field capital investment cost (C_{SF}), 'PC' represents the power cycle capital investment cost (C_{PC}), 'LAND' represents the land purchase cost (C_{land}), and 'CNT' represents the contingency costs (C_{cnt}). The solar field investment cost (C_{SF}) share is about the same as for the central receiver CSP plant, but the power cycle capital cost (C_{PC}) share is higher. This is mainly because of the addition of the boiler in the power cycle for the parabolic trough CSP plant. Figure 5.17 shows the breakdown of capital investment cost for the power cycle equipment ($C_{PC,eqp}$) for the same case as in Figure 5.16. The turbine and the generator still occupy the largest share of the power cycle investment costs, but the third largest share is now for the boiler, followed by the recuperators, the condensers, the pumps, and finally the separator.

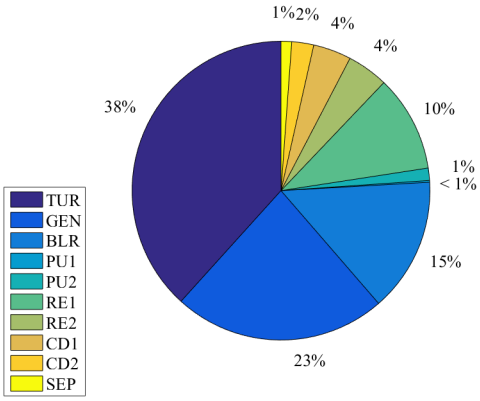

Figure 5.17: Capital investment cost for the power cycle equipment for the Kalina cycle parabolic trough CSP plant for a turbine inlet pressure and ammonia mass fraction of 100 bar and 0.5.

Table 5.12: LCOE breakdown for the Kalina cycle parabolic trough CSP plant for a turbine inlet pressure and ammonia mass fraction of 100 bar and 0.5.

LCOE component	Value ($ MWh^{-1})	Share in LCOE (%)
Solar field capital investment cost	122.4	45.2
Power cycle equipment capital investment cost	32.1	11.8
Power cycle miscellaneous investment cost	42.0	15.5
Land purchasing cost	3.3	1.2
Contingency	40.0	14.8
Fixed O&M cost	27.0	10.0
Variable O&M cost	4.0	1.5
Total	270.8	100

Table 5.12 shows the share of the various costs in the optimal LCOE for the Kalina cycle with a turbine inlet pressure and ammonia mass fraction of 100 bar and 0.5. Similar to the central receiver CSP plant, the solar field capital investment cost has the highest share in the LCOE for the parabolic trough CSP plant too, followed by the power cycle total investment cost (equipment and miscellaneous expenses). The additional heat exchangers for the boiler have resulted in the percentage share of the power cycle cost to be larger than that for the central receiver CSP plant, and the share for the solar field to be slightly lower.

5.8 Sensitivity analysis

A sensitivity analysis on the results of the thermoeconomic optimization was performed in order to identify the parameters that affect the results most significantly. For the sensitivity analysis, the different cost parameters for the Kalina cycle CSP plant were varied by ±30 %

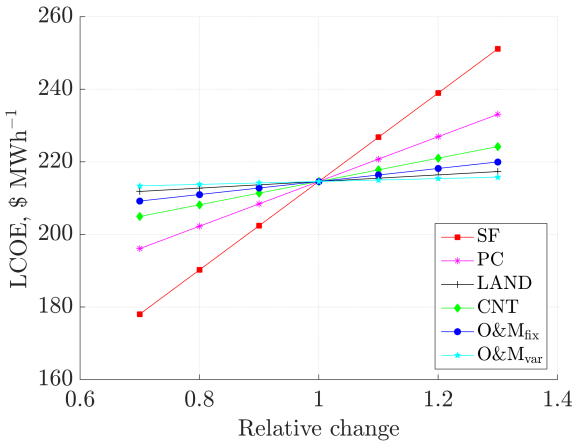

Figure 5.18: Sensitivity analysis for the different cost parameters for the Kalina cycle central receiver CSP plant for a turbine inlet pressure and ammonia mass fraction of 100 bar and 0.5.

from their optimal values and their effect on the LCOE was calculated. In the figures showing the sensitivity analysis results, the *relative change* on the horizontal axis denotes the ratio of the changed parameter value to its optimal value. The varied parameters were the solar field investment cost (C_{SF}), the power cycle investment cost (C_{PC}), the land investment cost (C_{land}), the contingency cost (C_{cnt}), and the fixed and variable O&M costs ($C_{O\&M,fix}$ and $C_{O\&M,var}$). In addition, the capital investment cost for the various solar field and power cycle components were also varied for a better insight into the results. The components such as the separator and the pumps had almost no impact on the LCOE because of their small share in the total plant capital investment cost, and therefore these components were omitted from the sensitivity analysis.

Figure 5.18 shows the variation in the LCOE for the **central receiver CSP plant** with the variation in the solar field investment cost (C_{SF}), the power cycle investment cost (C_{PC}), the land investment cost (C_{land}), the contingency cost (C_{cnt}), and the fixed and variable O&M costs ($C_{O\&M,fix}$ and $C_{O\&M,var}$). It may be observed that the LCOE is the most sensitive to the solar field investment cost (C_{SF}) which might be expected as the solar field occupies the largest share in the total plant investment cost (Figure 5.13). A 30 % change in the solar field investment cost (C_{SF}) results in about 17 % change in the LCOE. Similarly, a 30 % change in the power cycle investment cost (C_{PC}) results in about 9 % change in the LCOE. This is relevant for the Kalina cycle studies with an inherently complex layout resulting in higher capital investment costs. The LCOE is the least sensitive to the variable O&M cost ($C_{O\&M,var}$) and the land investment cost (C_{land}), which might be expected as the land purchasing cost occupies a much smaller share in the total capital investment cost as compared with the other costs.

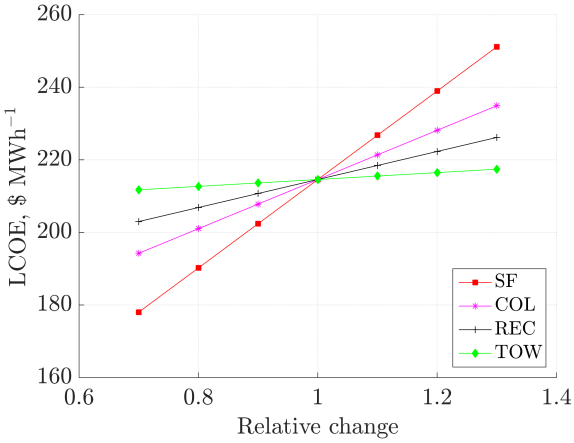

Figure 5.19: Sensitivity analysis for the different solar field cost parameters for the Kalina cycle central receiver CSP plant for a turbine inlet pressure and ammonia mass fraction of 100 bar and 0.5.

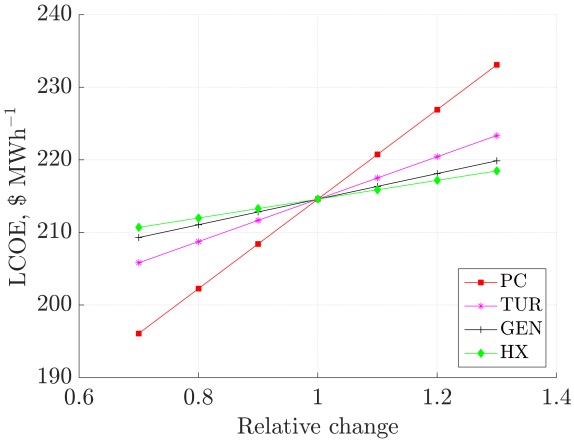

Figure 5.20: Sensitivity analysis for the different power cycle cost parameters for the Kalina cycle central receiver CSP plant for a turbine inlet pressure and ammonia mass fraction of 100 bar and 0.5.

Figures 5.19 and 5.20 show variation in the LCOE with respect to the variation in the individual elements of the solar field and the power cycle cost parameters, respectively, while Figure 5.21 shows the effect of variation in the real debt interest rate and the annual insurance rate. From the solar field, the tower has the least effect on the LCOE, whereas the heliostat mirror collectors have the highest effect. A 30 % change in the heliostat mirror collector capital investment cost (C_{col}) results in about 10 % change in the LCOE, which is slightly more than the variation for the entire power cycle capital investment cost (C_{PC}).

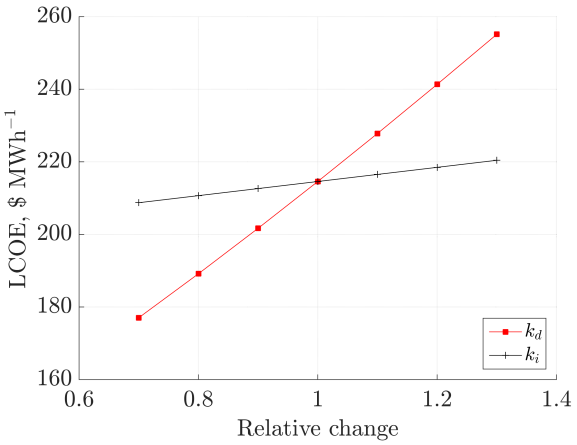

Figure 5.21: Sensitivity analysis for the different economic parameters for the Kalina cycle central receiver CSP plant for a turbine inlet pressure and ammonia mass fraction of 100 bar and 0.5.

This is because the heliostat mirror collectors are the most expensive part of the solar field because of the use of high quality reflective materials in their manufacturing. For the receiver of a central receiver CSP plant working with high temperature and pressure configuration, expensive materials will be required for manufacturing, hence the significant effect on the LCOE. Among the power cycle equipment, the turbine cost (C_{tur}) has the highest impact on the LCOE, followed by the generator and the heat exchangers. A 30 % change in the turbine capital investment cost (C_{tur}) results in about 4 % change in the LCOE. The real debt interest rate (k_d) has a significant impact on the LCOE as well, about as much as the solar field investment cost (C_{SF}). Therefore, a thorough market research must be conducted in order to find a suitable value for the economic calculations.

Figure 5.22 shows the variation in the LCOE for the **parabolic trough CSP plant** with the variation in the solar field investment cost (C_{SF}), the power cycle investment cost (C_{PC}), the land investment cost (C_{land}), the contingency cost (C_{cnt}), and the fixed and variable O&M costs ($C_{\text{O\&M,fix}}$ and $C_{\text{O\&M,var}}$). Similar to the central receiver CSP plant, the LCOE is the most sensitive to the solar field investment cost (C_{SF}) here as well. A 30 % change in the solar field capital investment cost (C_{SF}) results in about 16 % change in the LCOE, while the same for the power cycle capital investment cost (C_{PC}) results in about 10 % change in the LCOE.

Figures 5.23 and 5.24 show the variation in the LCOE with respect to the variation in the individual elements of the solar field and the power cycle cost parameters, while Figure 5.25 shows the effect of variation in the real debt interest rate and the annual insurance rate. Within the solar field, the parabolic trough system capital investment cost (C_{pt}) affects the LCOE more than the heat transfer fluid system capital investment cost (C_{htf}). This is because

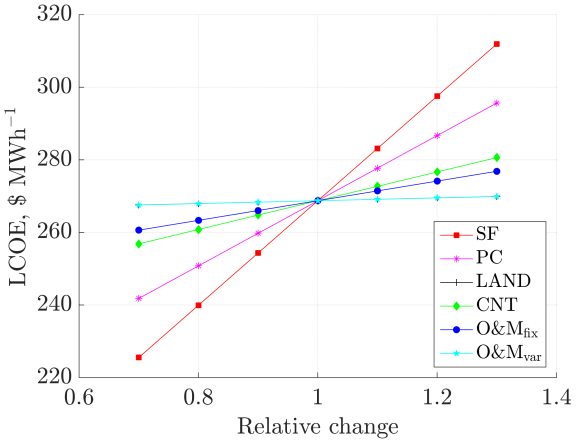

Figure 5.22: Sensitivity analysis for the different cost parameters for the Kalina cycle parabolic trough CSP plant for a turbine inlet pressure and ammonia mass fraction of 100 bar and 0.5.

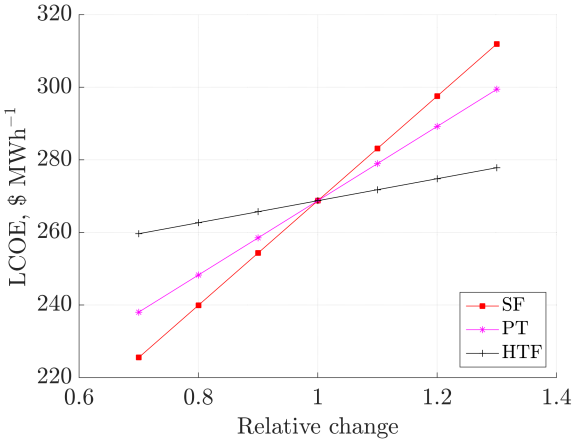

Figure 5.23: Sensitivity analysis for the different solar field cost parameters for the Kalina cycle parabolic trough CSP plant for a turbine inlet pressure and ammonia mass fraction of 100 bar and 0.5.

the parabolic trough field is the most expensive part of the solar field including both the reflective collector assembly and the receiver tubes, while the heat transfer fluid system mainly consists of the field headers and piping and the heat transfer fluid pump. A 30 % change in the parabolic trough system capital investment cost (C_{pt}) results in about 11 % change in the LCOE, while the same for the heat transfer system capital investment cost (C_{htf}) results in about 3 % change in the LCOE. Among the power cycle equipment, the turbine cost (C_{tur}) has the highest impact on the LCOE, but the second highest impact is now by the heat exchangers, followed by the generator. This is because of the addition of

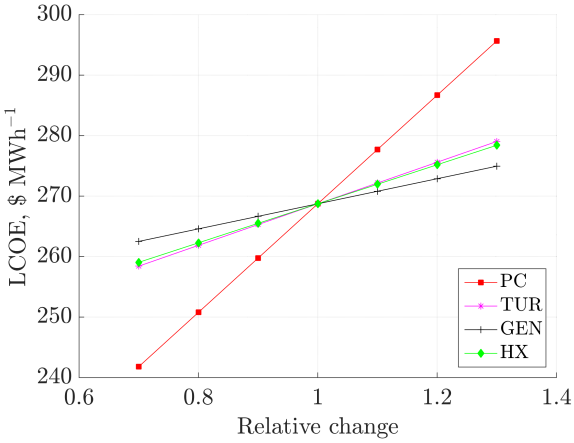

Figure 5.24: Sensitivity analysis for the different power cycle cost parameters for the Kalina cycle parabolic trough CSP plant for a turbine inlet pressure and ammonia mass fraction of 100 bar and 0.5.

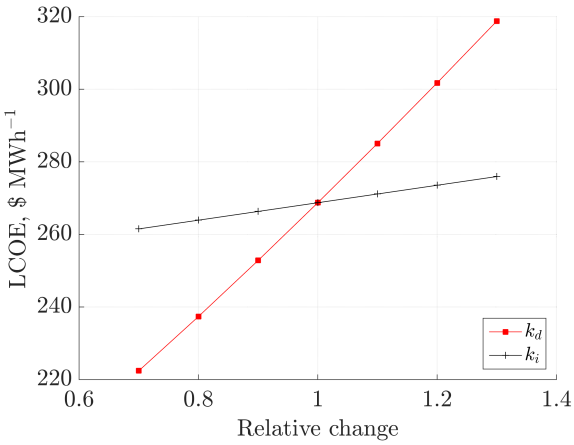

Figure 5.25: Sensitivity analysis for the different economic parameters for the Kalina cycle parabolic trough CSP plant for a turbine inlet pressure and ammonia mass fraction of 100 bar and 0.5.

the very expensive boiler in the power cycle (Figure 5.17). A 30 % change in the turbine capital investment cost (C_{tur}) results in about 4 % change in the LCOE. A 30 % change in total heat exchanger capital investment cost (including the boiler, the recuperators, and the condensers) also results in about 4 % change in the LCOE, although slightly lower than that for the turbine. Similar to the central receiver CSP plant, the real debt interest rate (k_d) has a significant impact on the LCOE for the parabolic trough CSP plant too, and again about as much as the solar field investment cost (C_{SF}).

5.9 Discussion

Kalina and Leibowitz [71] presented a part-load performance curve for the second law efficiency for a Kalina cycle operating as a gas turbine bottoming cycle. It was suggested that for the part-load operation, the mass flow rate through the Kalina cycle turbine could be kept constant while varying the turbine inlet ammonia mass fraction so as to vary the enthalpy drop across the turbine. In the current study, the turbine inlet ammonia mass fraction was however maintained at its design value during part-load operation. This was done as it was observed from an experimental investigation [107] that the turbine power output oscillates severely when the turbine inlet ammonia mass fraction is varied simultaneously with the evaporation pressure, and the oscillations were observed for several hours. Since the solar energy input varies throughout the day, changing the turbine inlet ammonia mass fraction frequently might not be the best operation strategy. On the other hand, the variation in the separator inlet ammonia mass fraction could be achieved by controlling the split fraction for the splitter SPL, without having to alter the turbine inlet ammonia mass fraction. In this way, the additional benefit of using fluid mixtures in the power cycle could be exploited by varying the composition in order to obtain a better performance in part-load conditions. For a turbine inlet ammonia mass fraction of 0.6 as an example, Figure 5.26 highlights the relative benefit between optimizing the separator inlet ammonia mass fraction in part load as compared with maintaining it at its design value. This relative benefit allows to operate the plant with better overall part-load performance resulting in larger electricity production for the same energy input (as fixed by the available solar energy at the plant location), thereby lowering the LCOE.

Table 5.13 shows an exemplary comparison of the optimal solutions from the thermodynamic and the thermoeconomic optimizations for the central receiver CSP plant with the Kalina cycle KC12 for a turbine inlet pressure and ammonia mass fraction of 100 bar and 0.5. It may be observed that the thermoeconomic optimum is quite different from the thermodynamic optimum. The LCOE calculated using the decision variable values from the thermodynamic optimum is much higher than the LCOE for the thermoeconomic optimum. The thermodynamic optimum has a cycle efficiency about 1.1 percentage point higher than the thermoeconomic optimum. A similar trend was observed for all the simulated combinations of the turbine inlet pressures and ammonia mass fractions, e.g. the thermodynamic and thermoeconomic optimal cycle efficiencies for a turbine inlet pressure and ammonia mass fraction of 140 bar and 0.8 are respectively 31.54 % and 30.88 %. The main difference lies in the preference to reject more heat in the condensers for the thermoeconomic optimum, than to recuperate the heat within the cycle for the thermodynamic optimum which would result in a higher cycle efficiency. This is because the capital investment cost of the recuperators is more than that for the condensers (as may be observed from the cost breakdown in Figure 5.14), hence the cycle optimization finds an overall cheaper solution by finding a thermoeconomic optimum in a less efficient cycle design. At the same time, it may also be

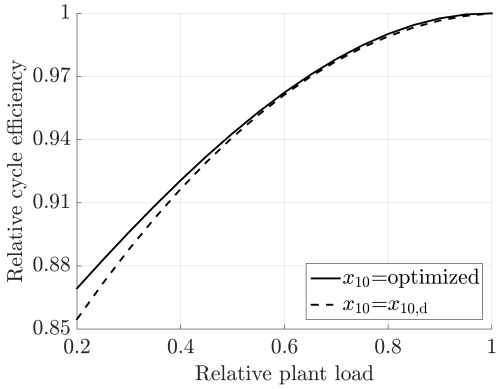

Figure 5.26: Part-load relative cycle efficiency when the separator inlet ammonia mass fraction (x_{10}) is maintained at its design value, or optimized in part load.

Table 5.13: Comparison between the thermodynamic and the thermoeconomic optima for a central receiver CSP plant for a turbine inlet pressure, temperature, and ammonia mass fraction of 100 bar, 500 °C, and 0.5.

		Value for the optimal solution	
Parameter	Symbol	Thermodynamic	Thermoeconomic
Levelized cost of electricity	LCOE	222.5 $\$\,MWh^{-1}$	214.6 $\$\,MWh^{-1}$
Cycle efficiency	η_{cy}	29.71 %	28.58 %
Turbine outlet pressure	p_2	1.00 bar	1.37 bar
Separator inlet ammonia mass fraction	x_{10}	0.3235	0.3280
Separator inlet temperature	T_{10}	71 °C	65 °C
Separator inlet vapour quality	X_{10}	9.41 %	6.09 %
Recuperator RE1 heat transfer	$\dot{Q}_{re1}$	5.69 MW	6.70 MW
Recuperator RE2 heat transfer	$\dot{Q}_{re2}$	28.99 MW	30.81 MW
Condenser CD1 heat transfer	$\dot{Q}_{cd1}$	34.41 MW	36.74 MW
Condenser CD2 heat transfer	$\dot{Q}_{cd2}$	12.07 MW	12.40 MW

observed that the thermodynamic and the thermoeconomic optimal cycle efficiencies are not too far apart from each other. This is because going for a very inefficient design will result in a larger solar field, which in turn will significantly increase the capital investment cost for the total plant, thereby resulting in a higher LCOE.

The Kalina cycle has a higher specific capital investment cost ($\widehat{C}_{inv}$) and a higher LCOE than the respective steam Rankine cycles for both the central receiver and the parabolic trough CSP plants. This is mainly because of two reasons: (1) worse power cycle efficiency than the corresponding steam Rankine cycle configuration resulting in a larger solar field requirement for the same net electrical power output, and (2) the higher capital investment cost for the power cycle itself. Even though the better part-load performance of the Kalina cycle allows it to operate for more hours annually (e.g. 3495 h for the central receiver CSP plant with Kalina

cycle compared with 3110 h for the steam Rankine cycle), the higher capital investment cost for the solar field and the power cycle make the additional few hundred hours of operation insufficient to achieve a lower LCOE than that for the steam Rankine cycle. Although the specific investment costs for the Kalina cycle are still within the ranges for the contemporary CSP plants without storage, between 4500 $\$\,kW^{-1}$ and 7150 $\$\,kW^{-1}$ [148], the costs are still on the higher side. The various shares in the breakdown of the capital investment costs (the solar field, the power cycle, the land, and the contingency in Figures 5.13 and 5.16) also exhibit a similar trend as could be found in the open literature [119,149]. The LCOE values for the contemporary CSP plants are between 146 $\$\,MWh^{-1}$ and 213 $\$\,MWh^{-1}$ [150], whereas for the Kalina cycles, the LCOE was found to be between about 212 $\$\,MWh^{-1}$ and 282 $\$\,MWh^{-1}$, generally outside the range of the contemporary values.

Looking at the Kalina cycle cost figures, the LCOE for the central receiver CSP plants is much lower than the LCOE for the parabolic trough CSP plants. This is because of two reasons. First, because of the huge increase in the power cycle investment cost (C_{PC}) for the parabolic trough CSP plant because of the addition of the boiler and a more expensive turbine due to the additional parasitic consumption for the heat transfer fluid pump (e.g. from about 1390 $\$\,kW^{-1}$ for a central receiver CSP plant to about 1820 $\$\,kW^{-1}$ for a parabolic trough CSP plant for a Kalina cycle with a turbine inlet pressure and ammonia mass fraction of 100 bar and 0.5). Second, because of the reduction in the operating hours for the power cycle (e.g. 3296 h of operation for the parabolic trough CSP plant as compared with the 3495 h for the central receiver CSP plant for a Kalina cycle with a turbine inlet pressure and ammonia mass fraction of 100 bar and 0.5). This reduction is possibly due to the lower solar field availability because of single-axis tracking for the parabolic trough solar field as compared with the two-axis tracking for the central receiver solar field, along with the additional boiler pinch and minimum thermal oil operation temperature constraints. In this study, the power cycle investment cost for the steam Rankine cycle were assumed to be the same for both the central receiver and the parabolic trough CSP plants, which explains the wider gap in the LCOE values for the Kalina cycle for the central receiver and the parabolic trough CSP plants, as compared with the relatively narrower gap between the LCOE values for the steam Rankine cycle for the two cases.

It might be argued that the steam Rankine cycle's specific capital investment cost for the state-of-the-art configuration with reheat and several feedwater heaters might be higher than the assumed $ 1200 per kW of gross capacity, given that the considered Kalina cycle configuration gives a relatively higher power cycle specific capital investment cost ($\widehat{C}_{PC}$) – between 1390 $\$\,kW^{-1}$ and 1560 $\$\,kW^{-1}$ for a central receiver CSP plant and between 1760 $\$\,kW^{-1}$ and 1900 $\$\,kW^{-1}$ for a parabolic trough CSP plant. However, even when the steam Rankine cycle specific investment cost is increased by 50 % from $ 1200 to $ 1800 per kW of gross capacity, the obtained LCOE for the central receiver and the parabolic trough CSP plants are respectively 207.0 $\$\,MWh^{-1}$ and 229.8 $\$\,MWh^{-1}$. These are still lower than

the lowest achievable LCOE for the respective Kalina cycle cases which is because of the huge share of the solar field in the overall cost structure for the CSP plants, and the requirement of a larger solar field for the Kalina cycle for the same plant rated capacity. As may be observed from the sensitivity analysis (Figures 5.18 and 5.22), the only way for the Kalina cycle to obtain an LCOE equivalent to the steam Rankine cycle is by reducing the solar field cost by at least 30 %. This implies that for large scale CSP plants, unless the power cycle is changed drastically which indirectly also affects the solar field, such as using a combined cycle with a volumetric receiver [151] resulting in a much higher cycle efficiency, the key to reducing the CSP plant costs lie in a cheaper solar field.

On the whole, the use of the Kalina cycle for CSP plants has its advantages and disadvantages. The main advantage is the reduction in the irreversibility during a phase change heat transfer process when using the ammonia-water mixture as the working fluid – the basis of the main hypothesis in this thesis. Other advantages include the possibility of all the cycle components operating at above atmospheric pressure, to be able to improve the part-load performance by varying the ammonia mass fraction, and the quick response to the changes in the operating conditions (e.g. it took less than 6 min for changing the ammonia mass fraction in the high pressure condenser from 0.80 to 0.72 as mentioned in Marston [152]). The disadvantages are mainly the inherent complexity of the plant and the lower cycle efficiency as compared with the state-of-the-art steam Rankine cycles which the Kalina cycle intends to replace, resulting in economically unattractive configurations. Thermodynamically, it is indeed possible to obtain higher efficiencies with Kalina cycles than the state-of-the-art steam Rankine cycles, but this requires even more complex layouts than the ones considered in this thesis. These layouts include multiple turbines, multiple mixers and splitters, and several heat exchangers some of which could be multi-stream heat exchangers as well [77]. These layouts may be considered for a base load operation or for operations where there are fewer fluctuations in the energy input or demand, but they might prove to be too complex to operate and control for highly fluctuating sources like solar energy. Therefore, when considering both the thermodynamic and the economic perspectives, the results from this thesis suggest that it is not beneficial to use the Kalina cycle for high temperature CSP plants.

5.10 Summary

The methodology and the results from the thermoeconomic optimization of the Kalina cycle KC12 for high temperature CSP plants (central receiver and parabolic trough) are presented and discussed. The Kalina cycle has the advantage of quick response times to the change in the operating conditions and an added degree of freedom in terms of the ammonia mass fraction as compared with using a pure fluid, which can be varied for a better part-load performance. However, the achievable design point cycle efficiencies are much lower than those of the state-of-the-art steam Rankine cycles resulting in larger solar fields for the same

rated plant capacity, thereby significantly increasing the capital investment cost. This causes the LCOE for nearly all the considered Kalina cycle cases to be outside the range of the contemporary LCOE values for both the central receiver and the parabolic trough CSP plants. Thus the results from this thesis suggest that it is not beneficial to use the Kalina cycle for high temperature CSP applications.

6

CONCLUSION

The thesis is concluded with an overview of the Kalina cycle thermoeconomic optimization methodology and results for CSP plants along with some suggestions for further research.

6.1 Modelling and results

The Kalina cycle was first introduced as a gas turbine bottoming cycle around 30 years ago. Since then it has been proposed for several low and high temperature applications such as geothermal power plants, waste heat recovery, ocean thermal energy conversion, and solar power plants. A high temperature Kalina cycle is inherently complex with the presence of a distillation-condensation subsystem and several heat exchangers in order to maximize the benefit of using a mixture as the cycle working fluid. Solving such a cycle in a computationally efficient manner presents a significant challenge. In this thesis, the thermoeconomic performance of a high temperature Kalina cycle was investigated for a central receiver and a parabolic trough CSP plant without storage. The key research question was that whether or not the use of a zeotropic mixture instead of a pure fluid in the power cycle enhances the overall cycle performance without compromising on the cycle's economic attractiveness. To answer this question, a thermoeconomic optimization considering both the thermodynamic and the economic aspects was carried out to fully evaluate the feasibility of using a Kalina cycle for a CSP plant.

An algorithm was first presented to solve a high temperature Kalina cycle in order to obtain the design and the part-load operating conditions. The design models based on the proposed methodology were validated from existing literature. The results from the thermodynamic optimization of different Kalina cycle layouts suggest that the placement and the number of the recuperators within the cycle affect the overall cycle performance trends. Among the compared configurations, the maximum cycle efficiency was obtained by the KC1234 layout (31.61 %) at a turbine inlet pressure and ammonia mass fraction of 140 bar and 0.8. The KC123 and the KC12 layouts were close with their maximum cycle efficiencies respectively equal to 31.60 % and 31.54 % at a turbine inlet pressure and ammonia mass fraction of 140 bar and 0.8 for both the layouts. The lowest cycle efficiency was obtained

by the KC234 layout (27.35 %), at a turbine inlet pressure and ammonia mass fraction of 100 bar and 0.8. Based on these results, the KC12 layout was selected for the detailed thermoeconomic analysis because of being simpler than the others with fewer recuperators, while being nearly as efficient as the more complex layouts.

For the thermoeconomic optimization, the LCOE was minimized by varying the turbine outlet pressure and the separator inlet temperature and ammonia mass fraction as the decision variables. The turbine inlet pressure and ammonia mass fraction were varied for a parametric analysis. The LCOE was calculated using the operation parameters from the power cycle and the solar field design along with their part-load performances and the cost functions to estimate the capital investment and the O&M costs. The proposed optimization methodology is generic in nature and therefore could also be employed for other Kalina cycle applications with slight modifications depending on the case at hand. Finally, a sensitivity analysis was carried out in order to determine the parameters which affected the LCOE the most.

From the thermoeconomic optimization of the Kalina cycle central receiver CSP plant, the results suggest that the LCOE is more sensitive to the turbine inlet pressure than to the turbine inlet ammonia mass fraction. All the combinations of the turbine inlet pressures and ammonia mass fractions resulted in a close range of LCOE values, between 212.2 $\$\,\mathrm{MWh}^{-1}$ and 218.9 $\$\,\mathrm{MWh}^{-1}$, mainly because of the large share of the solar field in the capital cost which governs the overall cost structure of the plant. For a similar plant, the state-of-the-art steam Rankine cycle had an LCOE of 181.0 $\$\,\mathrm{MWh}^{-1}$. From the thermoeconomic optimization of the Kalina cycle parabolic trough CSP plant, the results suggest that the LCOE is more sensitive to the turbine inlet ammonia mass fraction than the turbine inlet pressure, unlike in the case of the central receiver CSP plant. This is because of the addition of the boiler where the working solution ammonia mass fraction significantly affects the heat transfer performance, and therefore the investment cost. All the combinations of the turbine inlet pressures and ammonia mass fractions nevertheless still resulted in a close range of LCOE values, between 268.7 $\$\,\mathrm{MWh}^{-1}$ and 281.7 $\$\,\mathrm{MWh}^{-1}$, again because the large share of the solar field in the capital cost. For a similar plant, the state-of-the-art steam Rankine cycle had an LCOE of 202.5 $\$\,\mathrm{MWh}^{-1}$.

On the whole, the results from this thesis indicate that the Kalina cycle has a higher specific capital investment cost ($\widehat{C}_{\mathrm{inv}}$) and a higher LCOE than the respective steam Rankine cycles for both the central receiver and the parabolic trough CSP plants. This is mainly because of two reasons: (1) worse power cycle design point efficiency than the corresponding steam Rankine cycle configuration resulting in a larger solar field requirement for the same net electrical power output, and (2) the higher capital investment cost for the power cycle itself. This causes the LCOE for nearly all the considered Kalina cycle cases to be outside the range of the LCOE values for contemporary CSP plants. Even after increasing the steam

Rankine cycle capital investment cost by 50 % in order to account for any uncertainties in the Rankine cycle calculations, the steam Rankine cycle LCOE values are still lower than those of the Kalina cycle. The sensitivity analysis suggests that the only way to lower the LCOE for the Kalina cycles to the level of the contemporary values is to lower the solar field investment costs by at least 30 %. However, this would also positively affect the steam Rankine cycle plants, thereby reducing their LCOE as well. Therefore when considering both the thermodynamic and the economic perspectives, the results from this study suggest that it is not beneficial to use the Kalina cycle for high temperature CSP plants.

6.2 Further research

The current analysis may be furthered by including a thermal energy storage system in the plant. Using a molten salt central receiver with a molten salt storage system could be an example, where a better match between the temperature profiles of the receiver heat transfer fluid and the power cycle working fluid could further reduce the irreversibility in the cycle. Additionally, for a fairer comparison, the steam Rankine cycle may also be modelled in a similar way as was done for the Kalina cycle.

One of the biggest bottlenecks in the high temperature Kalina cycle research is the lack of experimental data and computationally efficient methods to estimate the thermophysical properties of the ammonia-water mixtures. This causes the optimization iterations to not converge on many occasions and a single optimization simulation could run for 4-5 days on a decent computer. Therefore, having more accurate and computationally efficient ways to estimate the thermodynamic and transport properties of the ammonia-water mixtures would be a significant development in evaluating the Kalina cycles.

Even though all the costs in this thesis have been inflated to represent current values, establishing more recent capital and O&M cost functions would be an important step further.

One of the advantages of using an ammonia-water mixture as the working fluid is that the mixture freezing point is much lower than that of pure water. This is a desirable quality for power plants which are designed to operate in cold countries where using pure water could lead to freezing problems. The thermoeconomic performance of the Kalina cycle could be analysed for these climatic conditions.

Lastly, using Kalina cycles for low temperature applications has seen increased interest in recent years. This could be combined with micro-CSP plants for rural and off-grid applications to develop compact low temperature solar power plants. The same analysis could also be carried out with simpler collectors (e.g. flat plate) as a way to reduce the plant capital investment costs.

REFERENCES

[1]. NORDEN and IEA. Nordic energy technology perspectives: Pathways to a carbon neutral energy future. Report, International Energy Agency, Paris Cedex, France, 2013.

[2]. Government of India - Ministry of New and Renewable Energy. Jawaharlal Nehru National Solar Mission, 2015. [Online]. Available: `www.mnre.gov.in/solar-mission/jnnsm/introduction-2/`. [Accessed: 2015-05-30].

[3]. REN21 Renewable Energy Policy Network for the 21st Century. Renewables 2014 Global Status Report. Report, Paris, France, 2014.

[4]. J. Twidell and T. Weir. *Renewable energy resources*. Taylor & Francis, Abingdon, Oxon, UK, 2nd edition, 2006.

[5]. T.M. Razykov, C.S. Ferekides, D. Morel, E. Stefanakos, H.S. Ullal, and H.M. Upadhyaya. *Solar photovoltaic electricity: Current status and future prospects*. Solar Energy, 85(8):1580–1608, 2011.

[6]. A. Modi, A. Chaudhuri, B. Vijay, and J. Mathur. *Performance analysis of a solar photovoltaic operated domestic refrigerator*. Applied Energy, 86(12):2583–2591, 2009.

[7]. F. Fuso Nerini, F. Valentini, A. Modi, G. Upadhyay, M. Abeysekera, S. Salehin, and E. Appleyard. *The Energy and Water Emergency Module; A containerized solution for meeting the energy and water needs in protracted displacement situations*. Energy Conversion and Management, 93:205–214, 2015.

[8]. J. Mathur, A. Modi, and S.S. Janakiraman. *Improving indoor air quality in rural areas using solar and wind energy*. World Renewable Energy Congress X, pages 284–289, Glasgow, Scotland. WREN. 2008.

[9]. C.-J. Winter, R.L. Sizmann, and L.L. Vant-Hull, editors. *Solar power plants*. Springer-Verlag, Heidelberg, Germany, 1st edition, 1991.

[10]. K. Lovegrove and W. Stein, editors. *Concentrating solar power technology: Principles, Developments and Applications*. Woodhead Publishing Limited, Cambridge, UK, 1st edition, 2012.

[11]. OECD and IEA. Energy technology perspectives 2014: Harnessing electricity's potential. Report, International Energy Agency, Paris Cedex, France, 2014.

[12]. Greenpeace International, ESTIA, and SolarPACES. Concentrated solar thermal power - Now! Report, 2005.

[13]. Greenpeace International, SolarPACES, and ESTELA. Concentrating Solar Power: Global Outlook 2009. Report, Amsterdam, Netherlands, 2009.

[14]. H. Chen, D.Y. Goswami, M.M. Rahman, and E.K. Stefanakos. *A supercritical Rankine cycle using zeotropic mixture working fluids for the conversion of low-grade heat into power*. Energy, 36(1):549–555, 2011.

[15]. A.I. Kalina. *Combined-cycle system with novel bottoming cycle*. Journal of Engineering for Gas Turbines and Power, 106:737–742, 1984.

[16]. MathWorks. MATLAB, 2015. [Online]. Available: `www.mathworks.se/products/matlab`. [Accessed: 2015-03-16].

[17]. Sandia National Laboratories. DELSOL3, 2015. [Online]. Available: `http://energy.sandia.gov/energy/renewable-energy/solar-energy/csp-2/csp-codes-and-tools/`. [Accessed: 2015-06-24].

[18]. NREL. System Advisor Model, 2015. [Online]. Available: `www.sam.nrel.gov`. [Accessed: 2015-06-25].

[19]. National Institute for Standards and Technology. NIST REFPROP 9.1, 2013. [Online]. Available: `www.nist.gov/srd/nist23.cfm`. [Accessed: 2015-08-23].

[20]. B.L. Kistler. A user's manual for DELSOL3: A computer code for calculating the optical performance and optimal system design for solar thermal central receiver plants. Report, Sandia National Laboratories, Livermore, USA, 1986.

[21]. J.A. Duffie and W.A. Beckman. *Solar Engineering of thermal processes*. John Wiley & Sons, Inc., Hoboken, New Jersey, USA, 4th edition, 2013.

[22]. M.J. Montes, A. Abánades, J.M. Martínez-Val, and M. Valdés. *Solar multiple optimization for a solar-only thermal power plant, using oil as heat transfer fluid in the parabolic trough collectors*. Solar Energy, 83(12):2165–2176, 2009.

[23]. K. Vignarooban, X. Xu, A. Arvay, K. Hsu, and A.M. Kannan. *Heat transfer fluids for concentrating solar power systems - A review*. Applied Energy, 146:383–396, 2015.

[24]. Technology For Life. Europe's first commercial CSP tower opens in Spain, 2015. [Online]. Available: `https://technology4life.wordpress.com/2007/04/01/europe%C2%B4s-first-commercial-csp-tower-opens-in-spain/`. [Accessed: 2015-07-27].

[25]. W.B. Stine and M. Geyer. Power from the sun, 2015. [Online]. Available: `www.powerfromthesun.net/book.html`. [Accessed: 2015-07-27].

[26]. Q. Yu, Z. Wang, E. Xu, X. Li, and M. Guo. *Modeling and dynamic simulation of the collector and receiver system of 1* MWe *DAHAN solar thermal power tower plant*. Renewable Energy, 43:18–29, 2012.

[27]. T. Mancini, P. Heller, B. Butler, B. Osborn, W. Schiel, V. Goldberg, R. Buck, R. Diver, C. Andraka, and J. Moreno. *Dish-Stirling Systems: An Overview of Development and Status*. Journal of Solar Energy Engineering, 125(2):135, 2003.

[28]. Torresol Energy. Gemasolar CSP plant, 2015. [Online]. Available: `www.`

torresolenergy.com/TORRESOL/gemasolar-plant/en. [Accessed: 2015-07-27].

[29]. SOLUCAR. PS10 CSP plant, 2015. [Online]. Available: www.oddities123.com/solar-tower-solucar-ps10/. [Accessed: 2015-07-27].

[30]. C.K. Ho and B.D. Iverson. *Review of high-temperature central receiver designs for concentrating solar power*. Renewable and Sustainable Energy Reviews, 29:835–846, 2014.

[31]. NREL. TroughNet paraboilc trough solar power network, 2015. [Online]. Available: www.nrel.gov/csp/troughnet/power_plant_data.html. [Accessed: 2015-07-01].

[32]. DLR. Parabolic trough collector-receiver system, 2015. [Online]. Available: www.dlr.de/dlr/en/Portaldata/1/Resources/bilder/portal/portal_2011_7/parabolrinnen_almeria.jpg. [Accessed: 2015-07-27].

[33]. Schott Solar. Schott PTR70 receivers, 2015. [Online]. Available: www.schott.com/csp/english/download/schott_ptr70_4th_generation_brochure.pdf. [Accessed: 2015-07-27].

[34]. A. Gil, M. Medrano, I. Martorell, A. Lázaro, P. Dolado, B. Zalba, and L.F. Cabeza. *State of the art on high temperature thermal energy storage for power generation. Part 1 - Concepts, materials and modellization*. Renewable and Sustainable Energy Reviews, 14(1):31–55, 2010.

[35]. M. Medrano, A. Gil, I. Martorell, X. Potau, and L.F. Cabeza. *State of the art on high-temperature thermal energy storage for power generation. Part 2 - Case studies*. Renewable and Sustainable Energy Reviews, 14(1):56–72, 2010.

[36]. M. Liu, W. Saman, and F. Bruno. *Review on storage materials and thermal performance enhancement techniques for high temperature phase change thermal storage systems*. Renewable and Sustainable Energy Reviews, 16(4):2118–2132, 2012.

[37]. P. Pardo, A. Deydier, Z. Anxionnaz-Minvielle, S. Rougé, M. Cabassud, and P. Cognet. *A review on high temperature thermochemical heat energy storage*. Renewable and Sustainable Energy Reviews, 32:591–610, 2014.

[38]. SOLUCAR. PS10: a 11.0-MWe Solar Tower Power Plant with Saturated Steam Receiver, 2006. [Online]. Available: www.upcomillas.es/catedras/crm/report05/Comunicaciones/MesaIV/D.ValerioFern%25C3%25A1ndez-Solucar2.pdf.

[39]. NREL. CSP projects, 2015. [Online]. Available: www.nrel.gov/csp/solarpaces/. [Accessed: 2015-07-28].

[40]. ETHZ. PREC, 2015. [Online]. Available: www.pre.ethz.ch/research/projects/?id=solarcombinedcycle. [Accessed: 2015-08-24].

[41]. B. Kelly, U. Hermann, and M.J. Hale. *Optimization studies for integrated solar combined cycles*. Solar Forum, Washington, DC, USA. ASME. 2001.

[42]. Z. Ma and C.S. Turchi. Advanced supercritical carbon dioxide power cycle configurations for use in concentrating solar power systems. Report, NREL, Golden, Colorado, USA, 2011.

[43]. R. Radermacher and Y. Hwang. *Vapor compression heat pumps with refrigerant mixtures*. Taylor & Francis Group, LLC, Florida, USA, 1st edition, 2005.

[44]. K. Braimakis, M. Preißinger, D. Brüggemann, S. Karellas, and K. Panopoulos. *Low grade waste heat recovery with subcritical and supercritical Organic Rankine Cycle based on natural refrigerants and their binary mixtures*. Energy, 88:80–92, 2015.

[45]. G. Angelino and P. Colonna Di Paliano. *Multicomponent working fluids for organic Rankine cycles (ORCs)*. Energy, 23(6):449–463, 1998.

[46]. M. Chys, M. van den Broek, B. Vanslambrouck, and M. De Paepe. *Potential of zeotropic mixtures as working fluids in organic Rankine cycles*. Energy, 44(1):623–632, 2012.

[47]. F. Heberle, M. Preißinger, and D. Brüggemann. *Zeotropic mixtures as working fluids in organic Rankine cycles for low-enthalpy geothermal resources*. Renewable Energy, 37(1):364–370, 2012.

[48]. J.G. Andreasen, U. Larsen, T. Knudsen, L. Pierobon, and F. Haglind. *Selection and optimization of pure and mixed working fluids for low grade heat utilization using organic Rankine cycles*. Energy, 73:204–213, 2014.

[49]. T. Weith, F. Heberle, M. Preißinger, and D. Brüggemann. *Performance of siloxane mixtures in a high-temperature organic Rankine cycle considering the heat transfer characteristics during evaporation*. Energies, 7(9):5548–5565, 2014.

[50]. F. Heberle and D. Brüggemann. *Thermo-economic evaluation of organic Rankine cycles for geothermal power generation using zeotropic mixtures*. Energies, 8(3):2097–2124, 2015.

[51]. X. Zhang, M. He, and Y. Zhang. *A review of research on the Kalina cycle*. Renewable and Sustainable Energy Reviews, 16(7):5309–5318, 2012.

[52]. E. Thorin. *Power cycles with ammonia-water mixtures as working fluid*. Phd thesis, KTH Royal Institute of Technology, Stockholm, Sweden, 2000.

[53]. S. Mao, J. Deng, and M. Lü. *A Helmholtz free energy equation of state for the NH3-H2O fluid mixture: Correlation of the PVTx and vapor-liquid phase equilibrium properties*. Fluid Phase Equilibria, 393:26–32, 2015.

[54]. National Institute for Standards and Technology. REFPROP MATLAB Interface, 2015. [Online]. Available: `www.boulder.nist.gov/div838/theory/refprop/LINKING/Linking.htm#MatLabApplications`. [Accessed: 2015-04-08].

[55]. F-chart Software. Engineering Equation Solver (EES), 2015. [Online]. Available: `www.fchart.com/ees/`. [Accessed: 2015-07-10].

[56]. R. Tillner-Roth and D.G. Friend. *A Helmholtz free energy formulation of the thermodynamic properties of the mixture {water+ammonia}*. Journal of Physical and Chemical Reference Data, 27(1):63–96, 1998.

[57]. D.-Y. Peng and D.B. Robinson. *A new two-constant equation of state*. Industrial & Engineering Chemistry Fundamentals, 15(1):59–64, 1976.

[58]. E. Lemmon. National Institute of Standards and Technology. Private communication, 2013.

[59]. J.K. Jensen. Technical University of Denmark. Private communication, 2013.

[60]. A. Modi and F. Haglind. *Thermodynamic optimisation and analysis of four Kalina cycle layouts for high temperature applications*. Applied Thermal Engineering, 76: 196–205, 2015.

[61]. M. Conde Engineering. Thermophysical properties of {NH3 + H2O} solutions, 2006. [Online]. Available: `www.mrc-eng.com/Downloads/NH3&H2OPropsEnglish.pdf`. [Accessed: 2015-07-07].

[62]. C.L. Sassen, R.A.C. van Kwartel, H.J. van der Kooi, and J. de Swaan Arons. *Vapor-liquid equilibria for the system ammonia + water up to the critical region*. Journal of Chemical and Engineering Data, 35(2):140–144, 1990.

[63]. R.C. Reid, J.M. Prausnitz, and B.E. Poling. *The properties of gases and liquids*. McGraw-Hill, New York, USA, 4th edition, 1987.

[64]. E. Thorin. *Thermophysical properties of ammonia-water mixtures for prediction of heat transfer areas in power cycles*. International Journal of Thermophysics, 22(1): 201–213, 2001.

[65]. S.R. Nordtvedt. *Experimental and theoretical study of a compression/absorption heat pump with ammonia/water as working fluid*. Phd thesis, Norwegian University of Science and Technology, Trondheim, Norway, 2005.

[66]. M.R. Kærn, A. Modi, J.K. Jensen, and F. Haglind. *An assessment of transport property estimation methods for ammonia-water mixtures and their influence on heat exchanger size*. International Journal of Thermophysics, 36(7):1468–1497, 2015.

[67]. Y. El-Sayed. *On exergy and surface requirements for heat transfer processes involving binary mixtures*. The Winter Annual Meeting of the American Society of Mechanical Engineers, pages 19–24, Chicago, Illinois, USA. ASME. 1988.

[68]. M.D. Mirolli. Kalina cycle power systems in waste heat recovery applications, 2012. [Online]. Available: `www.globalcement.com/magazine/articles/721-kalina-cycle-power-systems-in-waste-heat-recovery-applications`. [Accessed: 2015-07-08].

[69]. A.I. Kalina. *Method of preventing nitridation or carburization of metals*. United States Patent 6482272 B2, 2002.

[70]. Kalex LLC. Kalina cycle power systems for solar-thermal applications, 2015. [Online]. Available: `www.kalexsystems.com/KalexSolarThermalBrochure7-11.pdf`. [Accessed: 2015-06-13].

[71]. A.I. Kalina and M. Tribus. *The Kalina power cycles, A progress report*. American Power Conference, pages 5–21, Chicago, Illinois, USA. Illinois Institute of Technology. 1989.

[72]. A.I. Kalina and H. Leibowitz. *Applying Kalina technology to a bottoming cycle for utility combined cycles*. Gas Turbine Conference and Exhibition, Anahelm, California, USA. ASME. 1987.

[73]. A.I. Kalina and H.M. Leibowitz. *System design and experimental development of the Kalina cycle technology*. 9th Annual Industrial Energy Technology Conference, pages 270–275, Houston, Texas, USA. September16-18, 1987.

[74]. A.I. Kalina and H.M. Leibowitz. *The design of a 3* MW *Kalina cycle experimental plant*. Gas Turbine and Aeroengine Congress, Amsterdam, Netherlands. ASME. June 6-9, 1988.

[75]. A.I. Kalina, H.M. Leibowitz, D.W. Markus, and R.I. Pelletier. *Further technical aspects and economics of a utility-size Kalina bottoming cycle*. Gas Turbine and Aeroengine Congress and Exposition, Orlando, Florida, USA. ASME. 1991.

[76]. A.I. Kalina and M. Tribus. *Advances in Kalina cycle technology (1980-1991): Part I Development of a practical cycle*. S.S. Stecco and M.J. Moran, editors, Flowers '92 Florence World Energy Research Symposium, pages 97–110, Florence, Italy. Nova Science Publishers, Inc. 1992.

[77]. A.I. Kalina and M. Tribus. *Advances in Kalina cycle technology (1980-1991): Part II Iterative improvements*. S.S. Stecco and M.J. Moran, editors, Flowers '92 Florence World Energy Research Symposium, pages 111–124, Florence, Italy. Nova Science Publishers, Inc. 1992.

[78]. N.G. Zervos. *Preliminary design and economics of a 100* MWe *coal-fired Kalina cycle power plant*. International Power Generation Conference, Atlanta, Georgia, USA. ASME. 1992.

[79]. N.G. Zervos, H.M. Leibowitz, and K.S. Robinson. *Startup and operating experience of the Kalina cycle demonstration plant*. ASME COGEN-TURBO, 6th International Conference on Gas Turbines in Cogeneration and Utility, Industrial and Independent Power Generation, volume 7, Houston, Texas, USA. ASME. 1992.

[80]. R.W. Smith, J. Ranasinghe, D. Stats, and S. Dykas. *Kalina combined cycle performance and operability*. PWR Joint Power Generation Conference, volume 30, pages 701–727. ASME. 1996.

[81]. S. Ogriseck. *Integration of Kalina cycle in a combined heat and power plant, a case study*. Applied Thermal Engineering, 29(14-15):2843–2848, 2009.

[82]. P. Bombarda, C.M. Invernizzi, and C. Pietra. *Heat recovery from diesel engines: A thermodynamic comparison between Kalina and ORC cycles*. Applied Thermal Engineering, 30(2-3):212–219, 2010.

[83]. O.K. Singh and S.C. Kaushik. *Energy and exergy analysis and optimization of Kalina cycle coupled with a coal fired steam power plant*. Applied Thermal Engineering, 51 (1-2):787–800, 2013.

[84]. A. Coskun, A. Bolatturk, and M. Kanoglu. *Thermodynamic and economic analysis and optimization of power cycles for a medium temperature geothermal resource*. Energy Conversion and Management, 78:39–49, 2014.

[85]. J. Wang, Z. Yan, E. Zhou, and Y. Dai. *Parametric analysis and optimization of a Kalina cycle driven by solar energy*. Applied Thermal Engineering, 50(1):408–415, 2013.

[86]. F. Sun, W. Zhou, Y. Ikegami, K. Nakagami, and X. Su. *Energy-exergy analysis and optimization of the solar-boosted Kalina cycle system 11 (KCS-11)*. Renewable Energy, 66:268–279, 2014.

[87]. U. Larsen, T.-V. Nguyen, T. Knudsen, and F. Haglind. *System analysis and optimisation of a Kalina split-cycle for waste heat recovery on large marine diesel engines*. Energy, 64:484–494, 2014.

[88]. T.-V. Nguyen, T. Knudsen, U. Larsen, and F. Haglind. *Thermodynamic evaluation of the Kalina split-cycle concepts for waste heat recovery applications*. Energy, 71:277–288, 2014.

[89]. H. Junye, C. Yaping, and W. Jiafeng. *Thermal performance of a modified ammonia-water power cycle for reclaiming mid/low-grade waste heat*. Energy Conversion and Management, 85:453–459, 2014.

[90]. C. Yue, D. Han, W. Pu, and W. He. *Comparative analysis of a bottoming transcritical ORC and a Kalina cycle for engine exhaust heat recovery*. Energy Conversion and Management, 89:764–774, 2015.

[91]. P. Zhao, J. Wang, and Y. Dai. *Thermodynamic analysis of an integrated energy system based on compressed air energy storage (CAES) system and Kalina cycle*. Energy Conversion and Management, 98:161–172, 2015.

[92]. V. Zare, S.M.S. Mahmoudi, and M. Yari. *On the exergoeconomic assessment of employing Kalina cycle for GT-MHR waste heat utilization*. Energy Conversion and Management, 90:364–374, 2015.

[93]. Z. Zhang, Z. Guo, Y. Chen, J. Wu, and J. Hua. *Power generation and heating performances of integrated system of ammonia-water Kalina-Rankine cycle*. Energy Conversion and Management, 92:517–522, 2015.

[94]. O.K. Singh and S.C. Kaushik. *Thermoeconomic evaluation and optimization of a Brayton-Rankine-Kalina combined triple power cycle*. Energy Conversion and Management, 71:32–42, 2013.

[95]. C.H. Marston. *Parametric analysis of the Kalina cycle*. Journal of Engineering for Gas Turbines and Power, 112:107–116, 1990.

[96]. C.H. Marston and M. Hyre. *Gas turbine bottoming cycles: Triple-pressure steam versus Kalina*. Journal of Engineering for Gas Turbines and Power, 117(January):10–15, 1995.

[97]. M.B. Ibrahim and R.M. Kovach. *A Kalina cycle application for power generation*. Energy, 18(9):961–969, 1993.

[98]. P.K. Nag and A.V.S.S.K.S. Gupta. *Exergy analysis of the Kalina cycle*. Applied Thermal Engineering, 18(6):427–439, 1998.

[99]. C. Dejfors, E. Thorin, and G. Svedberg. *Ammonia-water power cycles for direct-*

fired cogeneration applications. Energy Conversion and Management, 39(16-18): 1675–1681, 1998.

[100]. A. Modi and F. Haglind. *Performance analysis of a Kalina cycle for a central receiver solar thermal power plant with direct steam generation*. Applied Thermal Engineering, 65(1-2):201–208, 2014.

[101]. A. Modi, T. Knudsen, F. Haglind, and L.R. Clausen. *Feasibility of using ammonia-water mixture in high temperature concentrated solar power plants with direct vapour generation*. Energy Procedia, 57:391–400, 2014.

[102]. A. Modi and F. Haglind. *Optimisation of a Kalina cycle for a central receiver solar thermal power plant*. World Renewable Energy Congress XIII, London, UK. WREN. 2014.

[103]. T. Knudsen, L.R. Clausen, F. Haglind, and A. Modi. *Energy and exergy analysis of the Kalina cycle for use in concentrated solar power plants with direct steam generation*. Energy Procedia, 57:361–370, 2014.

[104]. A. Modi, M.R. Kærn, J.G. Andreasen, and F. Haglind. *Economic optimization of a Kalina cycle for a parabolic trough solar thermal power plant*. ECOS 2015 - 28th International Conference on Efficiency, Cost, Optimization, Simulation and Environmental Impact of Energy Systems, Pau, France. 2015.

[105]. Y. Amano, K. Takeshita, T. Hashizume, M. Akiba, A. Usul, and Y. Tanzawa. *Experimental results of an ammonia-water mixture turbine system*. JPGC International Joint Power Generation Conference, pages 69–75, New Orleans, Louisiana, USA. ASME. 2001.

[106]. K. Takeshita, Y. Amano, and T. Hashizume. *Experimental results of an ammonia-water mixture turbine system (Part 2: Effect of the ammonia mass fraction)*. JPGC International Joint Power Generation Conference, pages 959–964, Phoenix, Arizona, USA. ASME. 2002.

[107]. Y. Amano, K. Kawanishi, and T. Hashizume. *Experimental investigations of oscillatory fluctuation in an ammonia-water mixture turbine system*. IMECE International Mechanical Engineering Congress and Exposition, volume 45, pages 391–398, Ontario, Florida, USA. ASME. 2005.

[108]. K. Takeshita, Y. Amano, and T. Hashizume. *Experimental study of advanced cogeneration system with ammonia-water mixture cycles at bottoming*. Energy, 30(2-4): 247–260, 2005.

[109]. H. Yuan, N. Mei, S. Hu, L. Wang, and S. Yang. *Experimental investigation on an ammonia-water based ocean thermal energy conversion system*. Applied Thermal Engineering, 61(2):327–333, 2013.

[110]. G. Mittelman and M. Epstein. *A novel power block for CSP systems*. Solar Energy, 84 (10):1761–1771, 2010.

[111]. Abengoa Solar. Abengoa CSP plants, 2015. [Online]. Available: `www.abengoasolar.com/web/en/plantas_solares/plantas_propias/espana/`. [Accessed: 2015-07-01].

[112]. S.M.I. Karimulla. Arani Power Systems Ltd. Private communication, 2014.

[113]. SOLUTIA. Therminol VP-1, 2015. [Online]. Available: www.twt.mpei.ac.ru/TTHB/HEDH/HTF-VP1.PDF. [Accessed: 2014-06-30].

[114]. F. Lippke. Simulation of the part-load behavior of a 30 MWe SEGS plant. Report, Sandia National Laboratories, SAND95-1293, 1995.

[115]. A.M. Patnode. *Simulation and performance evaluation of parabolic trough solar power plants*. Master thesis, University of Wisconsin-Madison, USA, 2006.

[116]. MathWorks. MATLAB Genetic Algorithm, 2015. [Online]. Available: https://se.mathworks.com/discovery/genetic-algorithm.html. [Accessed: 2015-08-20].

[117]. K.H. Kim, C.H. Han, and K. Kim. *Effects of ammonia concentration on the thermodynamic performances of ammonia-water based power cycles*. Thermochimica Acta, 530: 7–16, 2012.

[118]. Meteotest. Meteonorm. www.meteonorm.com. Accessed: 2015-08-31.

[119]. R. Pitz-Paal, J. Dersch, and B. Milow. ECOSTAR European Concentrated Solar Thermal Road-Mapping. Report, DLR, 2005.

[120]. H.A. Mlcak and M.D. Mirolli. *Systems and methods for increasing the efficiency of a Kalina cycle*. United States Patent 8744636 B2, 2014.

[121]. D.H. Cooke. *Modeling of off-design multistage turbine pressures by Stodola's ellipse*. Energy Incorporated PEPSE User's Group Meeting, pages 205–234, Richmond, Virginia, USA. Bechtel Power Corporation. 1983.

[122]. A. Ray. *Dynamic modelling of power plant turbines for controller design*. Applied Mathematical Modelling, 4(2):109–112, 1980.

[123]. F. Haglind and B. Elmegaard. *Methodologies for predicting the part-load performance of aero-derivative gas turbines*. Energy, 34(10):1484–1492, 2009.

[124]. P. Schwarzbözl. A TRNSYS model library for solar thermal electric components (STEC). Report, Deutsches Zentrum für Luft und Raumfahrt e.V. (DLR), Cologne, Germany, 2006.

[125]. M.R. Kærn, A. Modi, J.K. Jensen, J.G. Andreasen, and F. Haglind. *An assessment of in-tube flow boiling correlations for ammonia-water mixtures and their influence on heat exchanger size*. Applied Thermal Engineering, 93:623–638, 2016.

[126]. P.K. Nag. *Power plant engineering*. Tata Mc-Graw Hill Publishing Company Limited, New Delhi, India, 3rd edition, 2008.

[127]. R. Smith. *Chemical Process - Design and Integration*. John Wiley & Sons, Ltd., West Sussex, 2005.

[128]. R.K. Sinnott. *Coulson & Richardson's Chemical Engineering Volume 6*. Elsevier Butterworth-Heinemann, Oxford, UK, 4th edition, 2005.

[129]. T.L. Bergman, A.S. Lavine, F.P. Incropera, and D.P. Dewitt. *Fundamentals of heat and mass transfer*. John Wiley & Sons, Inc., Jefferson City, USA, 7th edition, 2011.

[130]. M.M. Shah, A.M. Mahmoud, and J. Lee. *An assessment of some predictive methods for in-tube condensation heat transfer of refrigerant mixtures*. ASHRAE Transactions, 119 (2):38–51, 2013.

[131]. K.J. Bell and M.A. Ghaly. *An approximate generalized design method for multicomponent/partial condensers*. 13th National Heat Transfer Conference, Denver, Colorado, USA. AIChE-ASME. 1972.

[132]. M.M. Shah. *Chart correlation for saturated boiling heat transfer: equations and further study*. ASHRAE Transactions, 88(1):185–196, 1982.

[133]. D.Q. Kern. *Process Heat Transfer*. McGraw-Hill Book Company, Singapore, 1950.

[134]. F. De Luca, V. Ferraro, and V. Marinelli. *On the performance of CSP oil-cooled plants, with and without heat storage in tanks of molten salts*. Energy, 83:230–239, 2015.

[135]. B.D. Ehrhart and D.D. Gill. Evaluation of annual efficiencies of high temperature central receiver concentrated solar power plants with thermal energy storage. Report, Sandia National Laboratories, SAND2013-5493, 2013.

[136]. A.L. Avila-Marin, J. Fernandez-Reche, and F.M. Tellez. *Evaluation of the potential of central receiver solar power plants: Configuration, optimization and trends*. Applied Energy, 112:274–288, 2013.

[137]. B. Ehrhart. Univeristy of Colorado at Boulder. Private communication, 2015.

[138]. N.B. Desai and S. Bandyopadhyay. *Optimization of concentrating solar thermal power plant based on parabolic trough collector*. Journal of Cleaner Production, 89:262–271, 2015.

[139]. DLR German Aerospace Center. Greenius, 2015. [Online]. Available: `http://freegreenius.dlr.de`. [Accessed: 2015-07-06].

[140]. N.S. Suresh, N.C. Thirumalai, B.S. Rao, and M.A. Ramaswamy. *Methodology for sizing the solar field for parabolic trough technology with thermal storage and hybridization*. Solar Energy, 110:247–259, 2014.

[141]. Marshall Valuation Services. Comparative cost indexes, 2014.

[142]. P. Dorj. *Thermoeconomic analysis of a new geothermal utilization CHP plant in Tsetserleg, Mongolia*. Master thesis, The United Nations University, Reykjavik, Iceland, 2005.

[143]. S. Pelster. *Environomic modelling and optimization of advanced combined cycle cogeneration power plants including CO_2 separation options*. Phd thesis, Ecole Polytechnique Federale de Lausanne, Lausanne, Switzerland, 1998.

[144]. G.D. Ulrich. *A Guide to Chemical Engineering Process Design and Economics*. John Wiley & Sons, Inc., New Jersey, USA, 1984.

[145]. R. Turton, R.C. Bailie, W.B. Whiting, J.A. Shaeiwitz, and D. Bhattacharyya. *Analysis, synthesis and design of chemical processes*. Prentice Hall, New Jersey, USA, 4th edition, 2012.

[146]. The Alstrom Corporation. Two-phase flow separators, 2015. [Online]. Available: www.alstromcorp.com/PDFCatalogue/SECTION5/ALMUS.pdf. [Accessed: 2015-02-26].

[147]. A. Bejan, G. Tsatsaronis, and M. Moran. *Thermal Design & Optimization*. John Wiley & Sons, Inc., 1st edition, 1996.

[148]. IRENA. Renewable energy Technologies: Cost Analysis Series - Concentrating solar power. Report, International Renewable Energy Agency, 2012. [Online]. Available: http://www.irena.org/documentdownloads/publications/re_technologies_cost_analysis-csp.pdf.

[149]. J.T. Hinkley, J.A. Hayward, B. Curtin, A. Wonhas, R. Boyd, C. Grima, A. Tadros, R. Hall, and K. Naicker. *An analysis of the costs and opportunities for concentrating solar power in Australia*. Renewable Energy, 57:653–661, 2013.

[150]. OECD and IEA. Technology roadmap - Solar thermal electricity. Report, International Energy Agency, Paris Cedex, France, 2014.

[151]. A.L. Ávila Marín. *Volumetric receivers in solar thermal power plants with central receiver system technology: A review*. Solar Energy, 85(5):891–910, 2011.

[152]. C.H. Marston. *Development of the adjustable proportion fluid mixture cycle*. Mechanical Engineering, 114(9):76–81, 1992.

[153]. C. Trapp and P. Colonna. *Efficiency improvement in precombustion CO_2 removal units with a waste-heat recovery ORC power plant*. Journal of Engineering for Gas Turbines and Power, 135(4):042311, 2013.

Appendices

A

THERMODYNAMIC PROPERTIES

Figure A.1 shows the legend for the thermodynamic property plots shown afterwards. The compared methods are:

1. REFPROP with MATLAB with the default Tillner-Roth and Friend formulation for ammonia-water mixtures [56].
2. REFPROP with MATLAB with the Peng-Robinson equation of state [57].
3. REFPROP with MATLAB with the 'Ammonia (Lemmon)' formulation [58] to be used in calculation of properties for ammonia-water mixtures.
4. REFPROP with MATLAB with the 'Ammonia (Lemmon)' formulation to be used in calculation of properties for ammonia-water mixtures using the Peng-Robinson equation of state.
5. Ibrahim-Klein equation of state with EES using the in-built 'NH3H2O' function. The data from the EES property calculations was provided by a colleague [59].

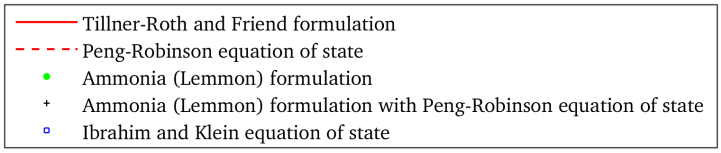

Figure A.1: Legend for the thermodynamic property comparison charts.

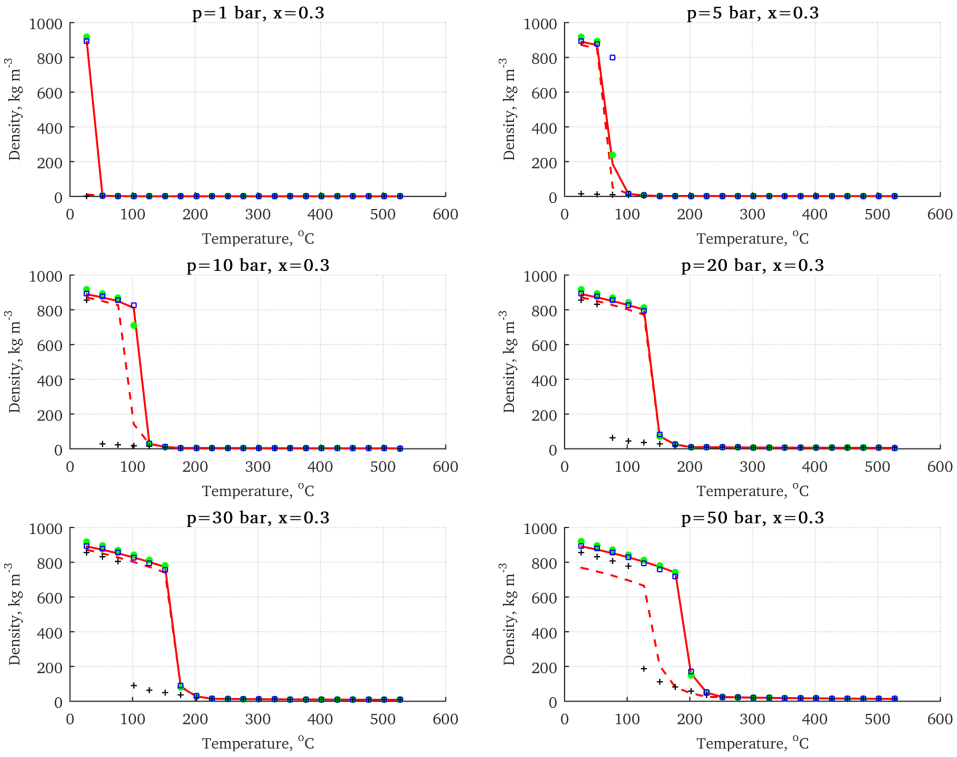

Figure A.2: Density at low pressures for an ammonia mass fraction of 0.3.

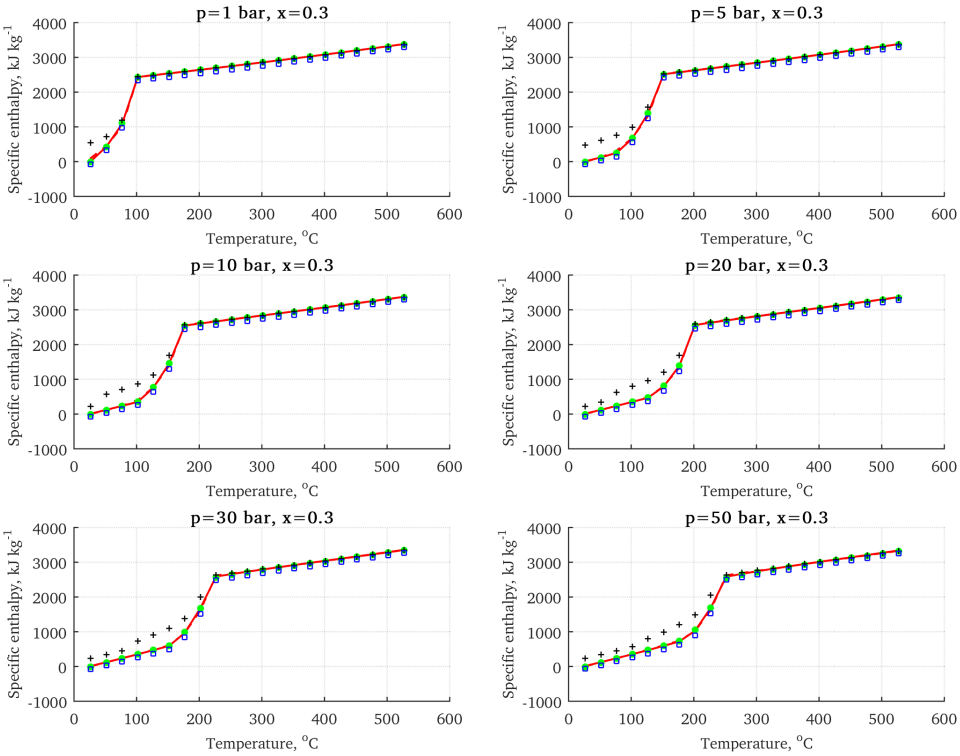

Figure A.3: Specific enthalpy at low pressures for an ammonia mass fraction of 0.3.

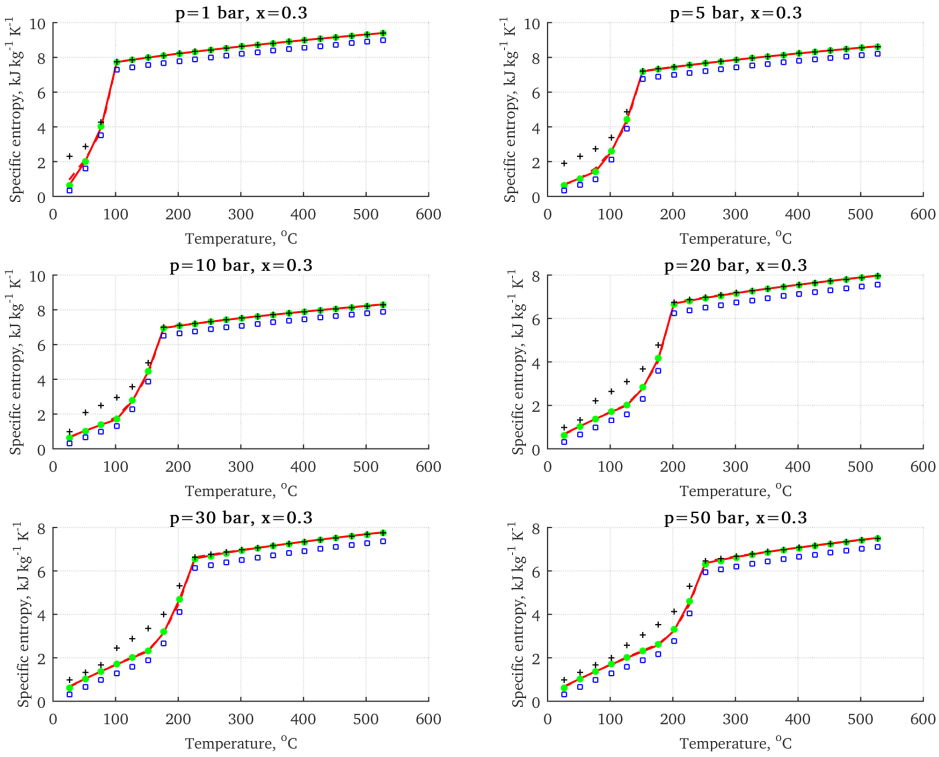

Figure A.4: Specific entropy at low pressures for an ammonia mass fraction of 0.3.

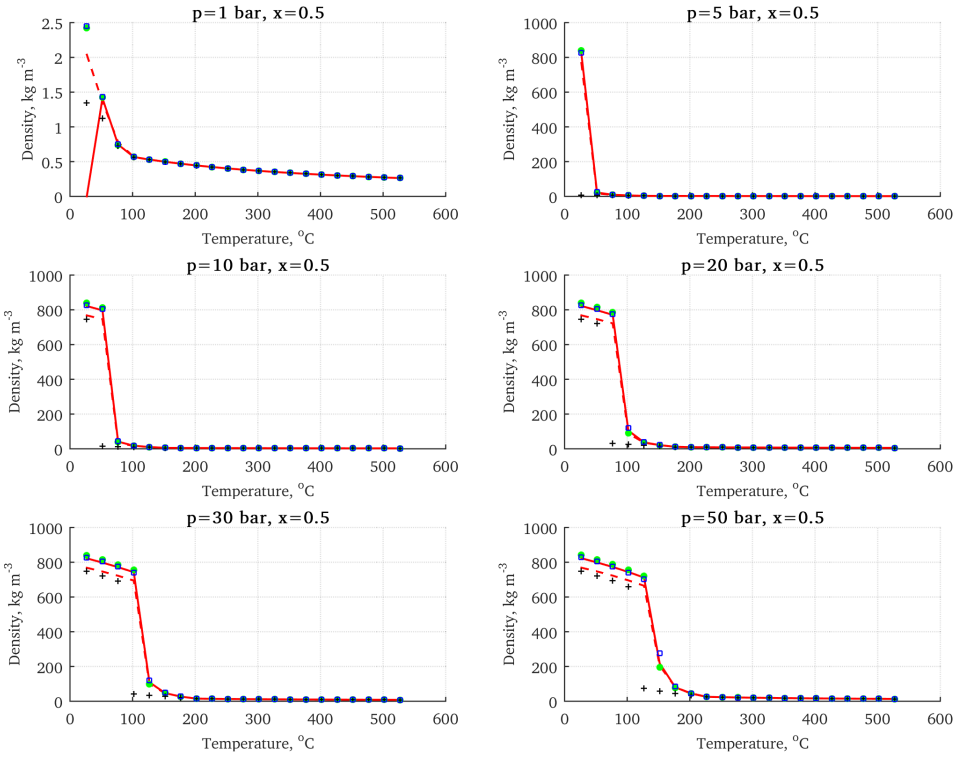

Figure A.5: Density at low pressures for an ammonia mass fraction of 0.5.

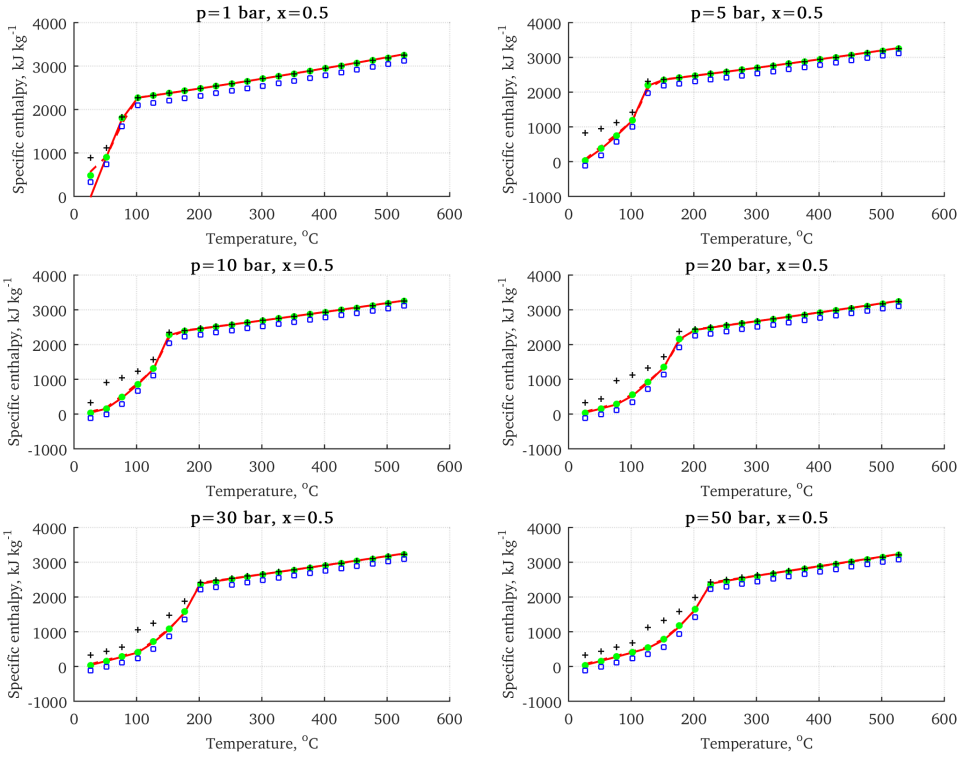

Figure A.6: Specific enthalpy at low pressures for an ammonia mass fraction of 0.5.

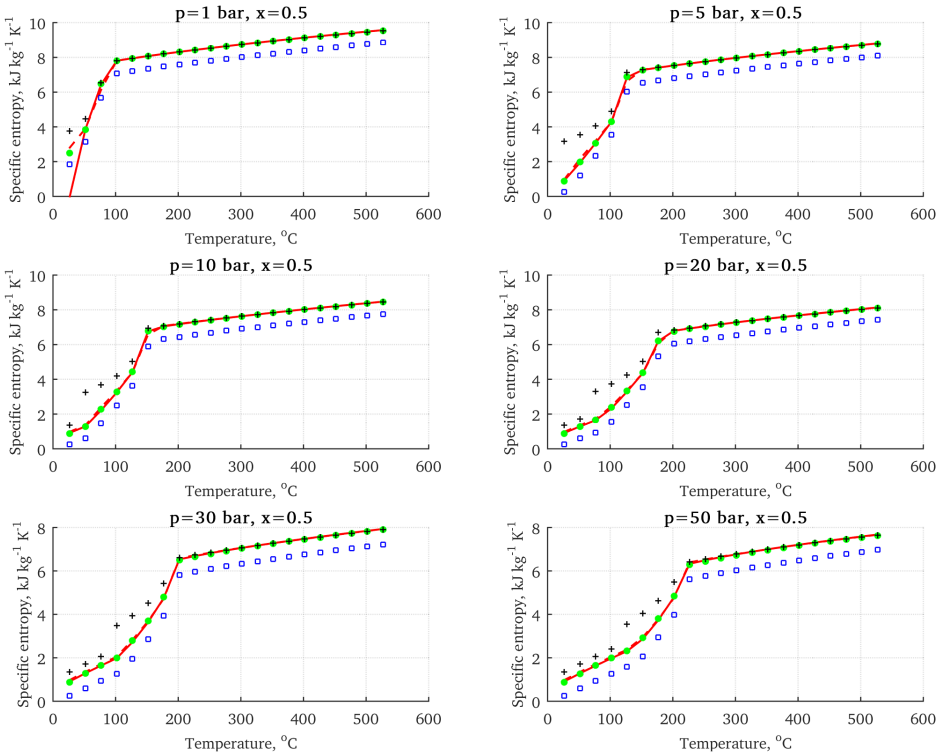

Figure A.7: Specific entropy at low pressures for an ammonia mass fraction of 0.5.

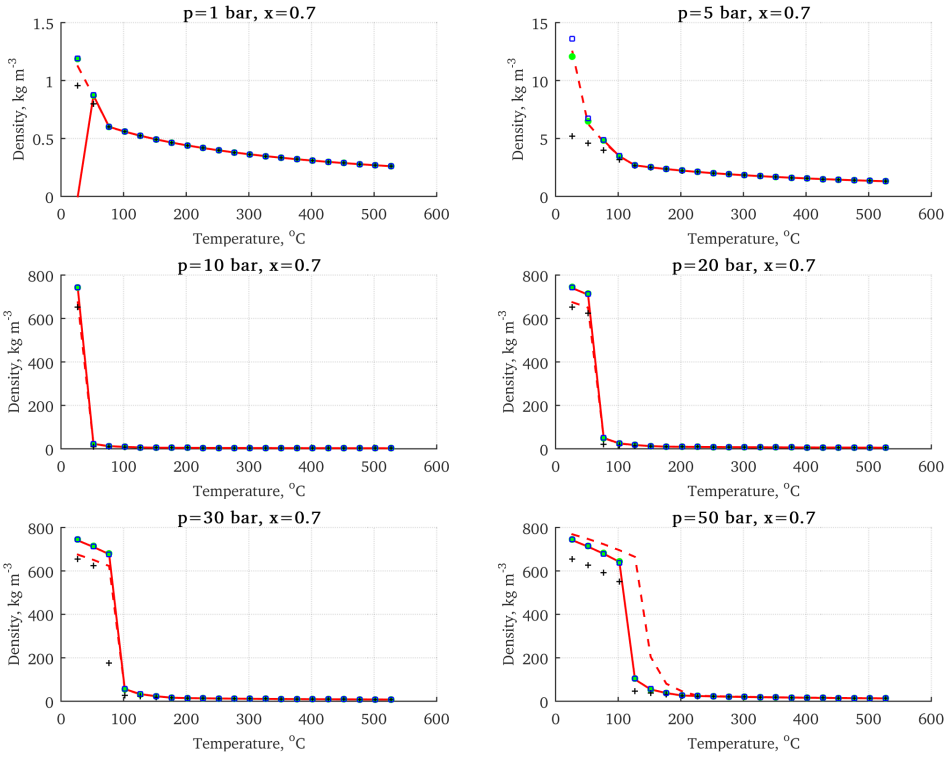

Figure A.8: Density at low pressures for an ammonia mass fraction of 0.7.

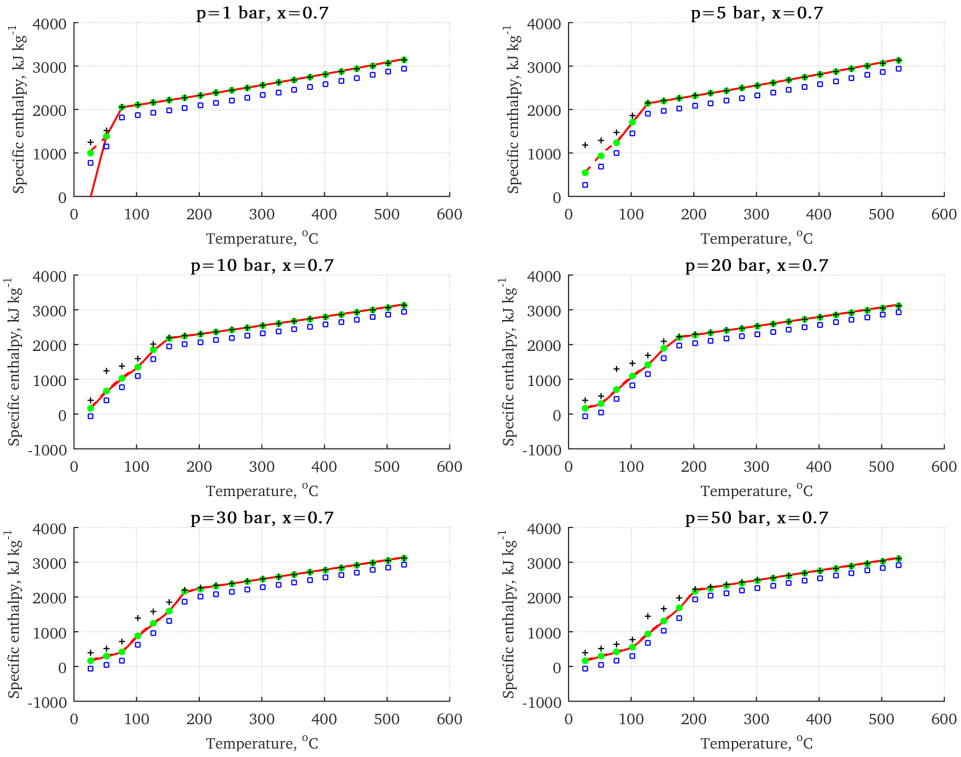

Figure A.9: Specific enthalpy at low pressures for an ammonia mass fraction of 0.7.

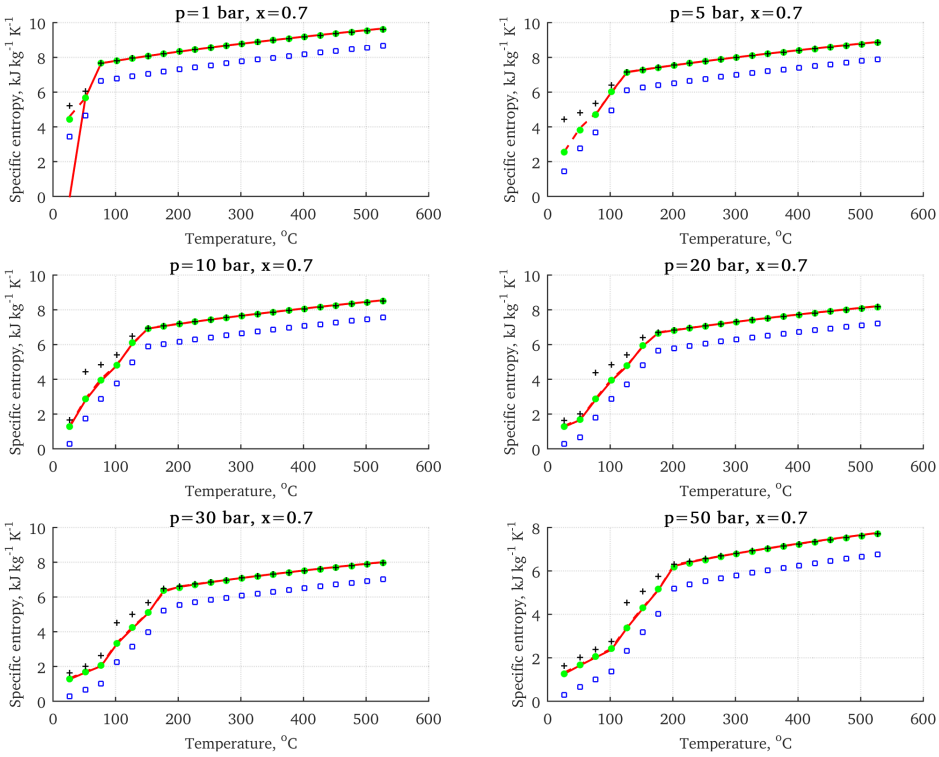

Figure A.10: Specific entropy at low pressures for an ammonia mass fraction of 0.7.

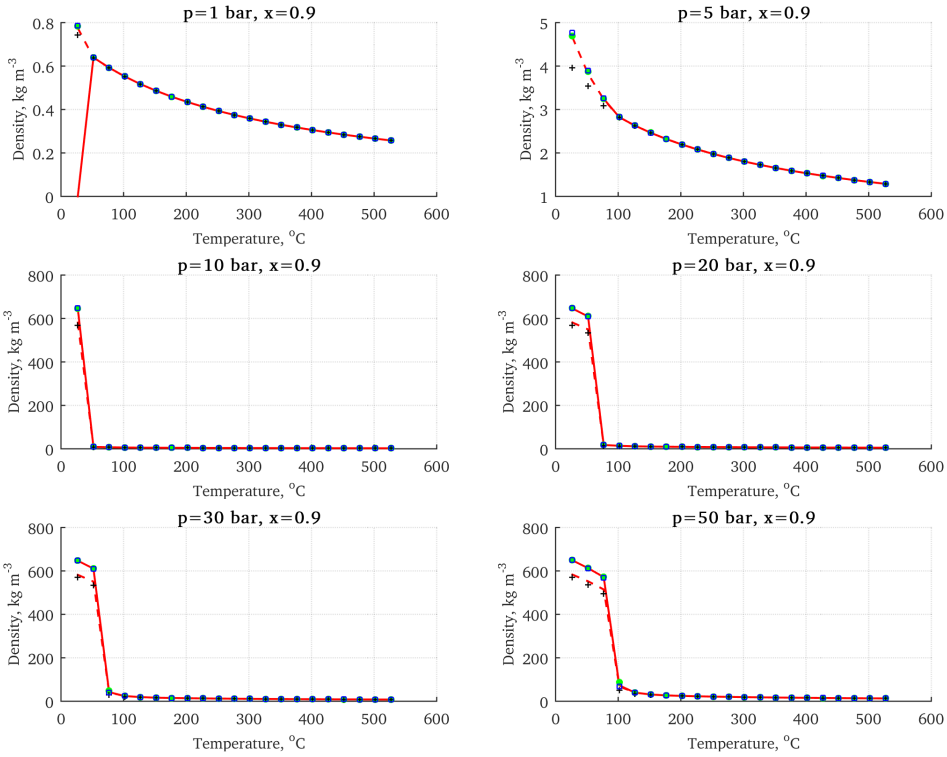

Figure A.11: Density at low pressures for an ammonia mass fraction of 0.9.

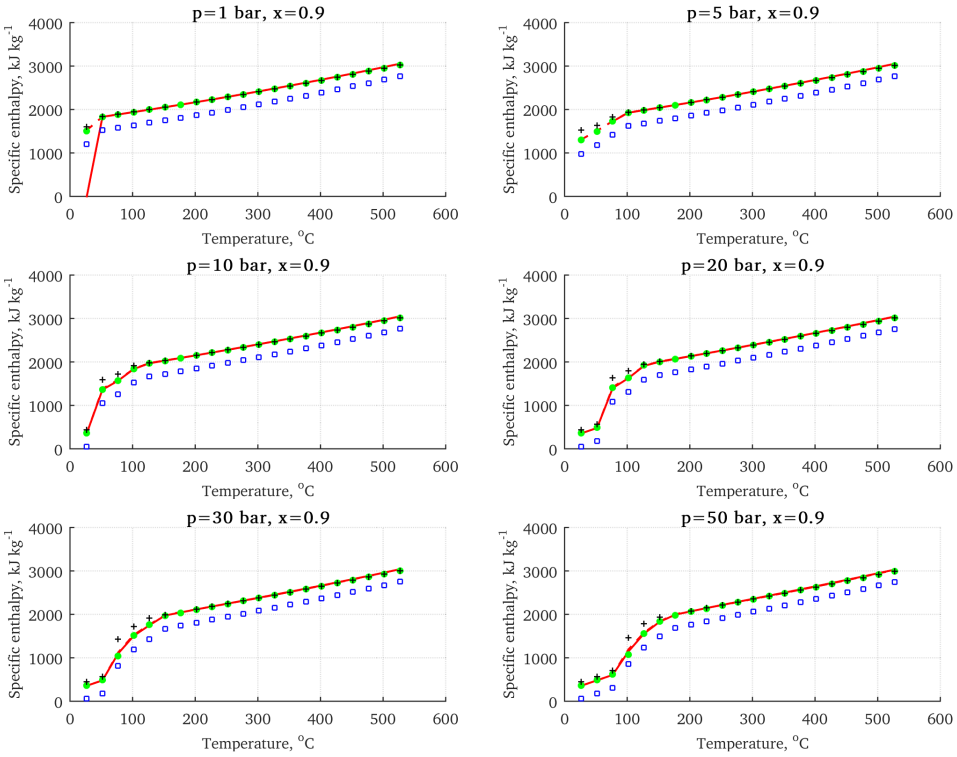

Figure A.12: Specific enthalpy at low pressures for an ammonia mass fraction of 0.9.

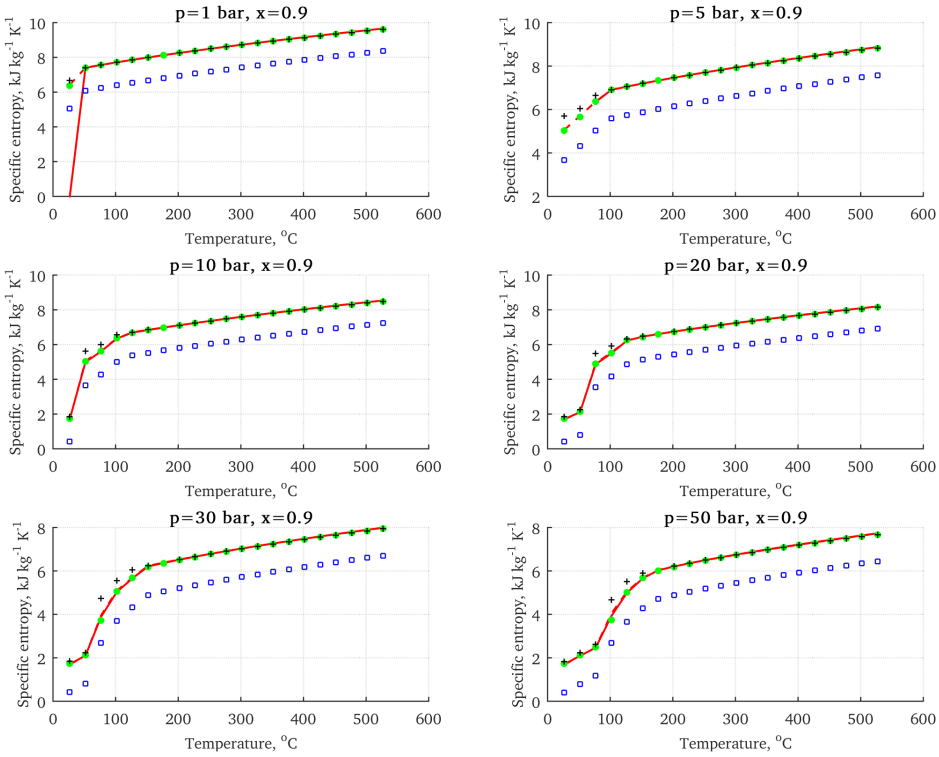

Figure A.13: Specific entropy at low pressures for an ammonia mass fraction of 0.9.

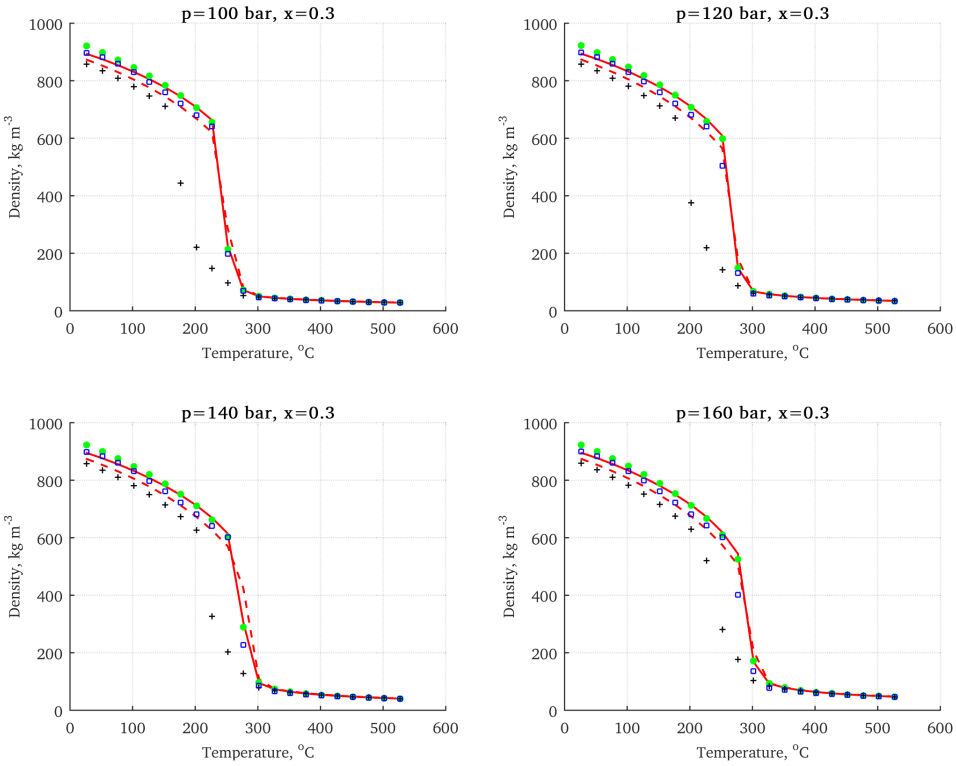

Figure A.14: Density at high pressures for an ammonia mass fraction of 0.3.

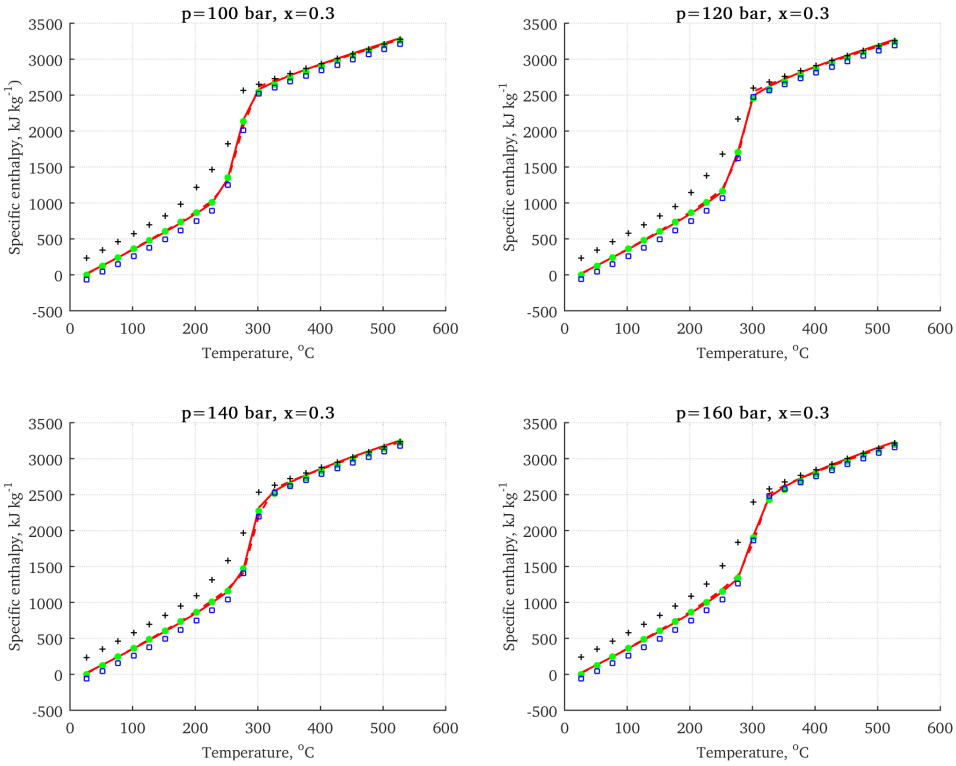

Figure A.15: Specific enthalpy at high pressures for an ammonia mass fraction of 0.3.

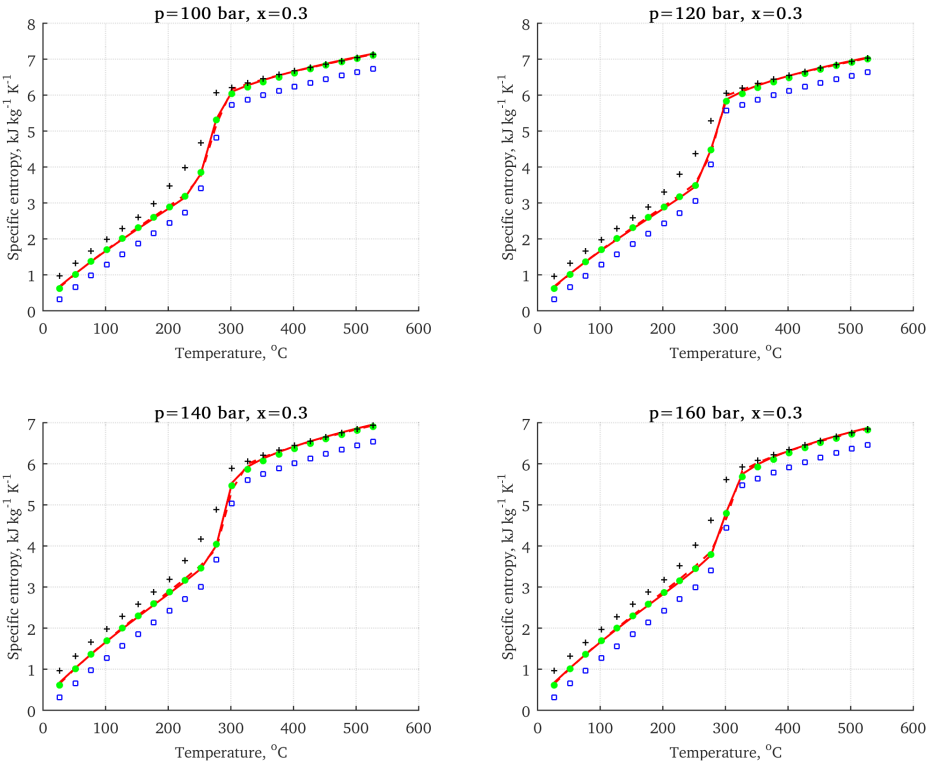

Figure A.16: Specific entropy at high pressures for an ammonia mass fraction of 0.3.

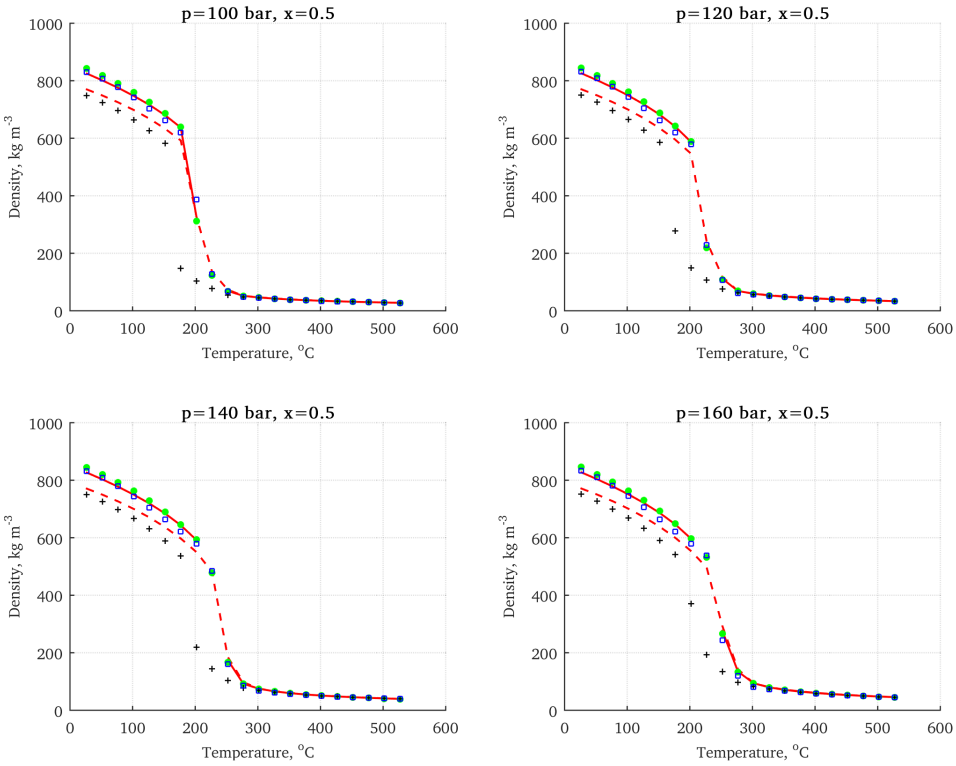

Figure A.17: Density at high pressures for an ammonia mass fraction of 0.5.

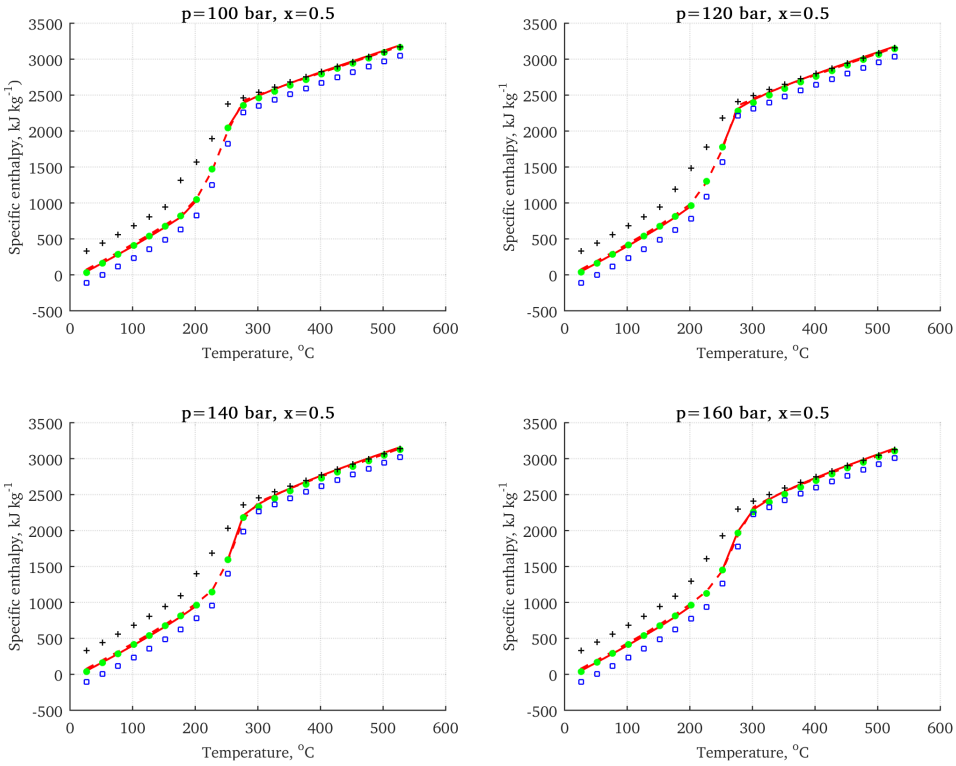

Figure A.18: Specific enthalpy at high pressures for an ammonia mass fraction of 0.5.

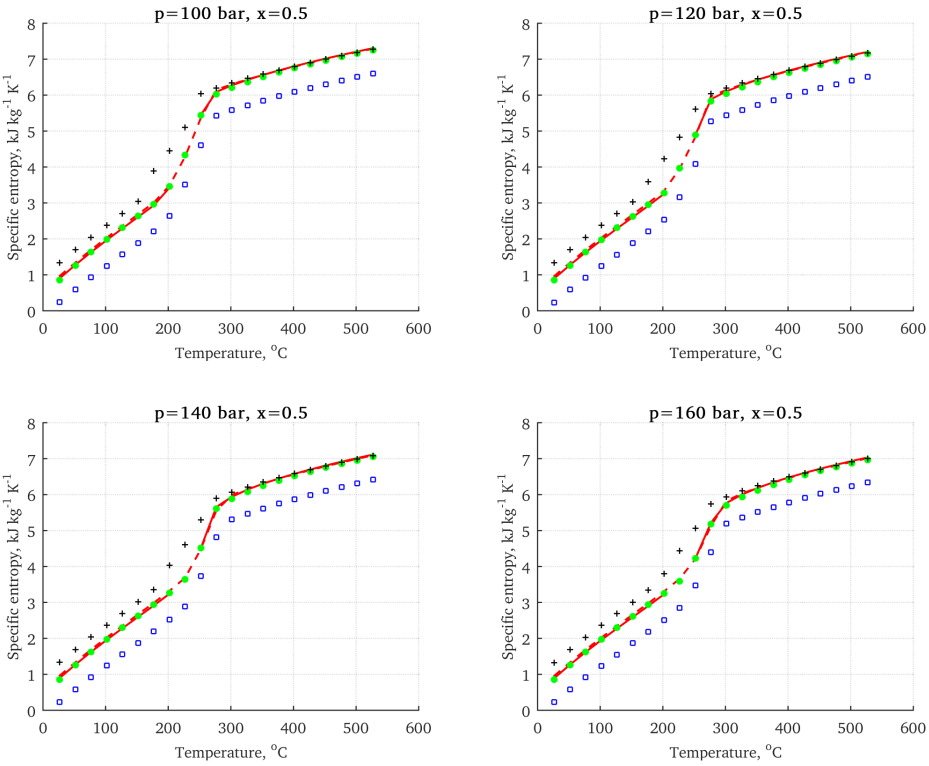

Figure A.19: Specific entropy at high pressures for an ammonia mass fraction of 0.5.

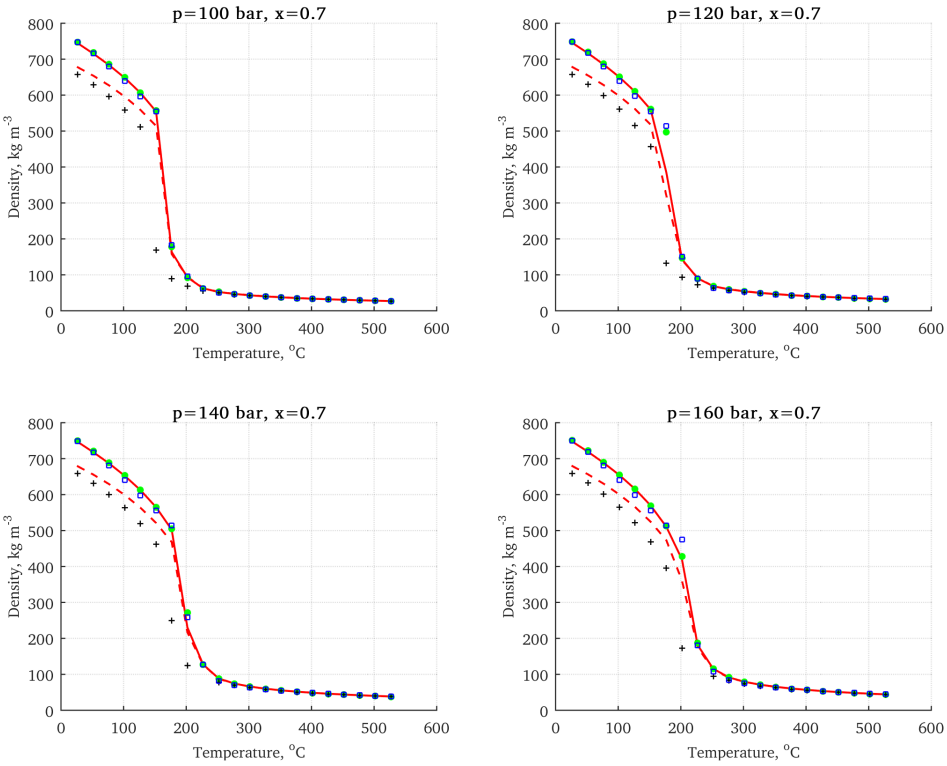

Figure A.20: Density at high pressures for an ammonia mass fraction of 0.7.

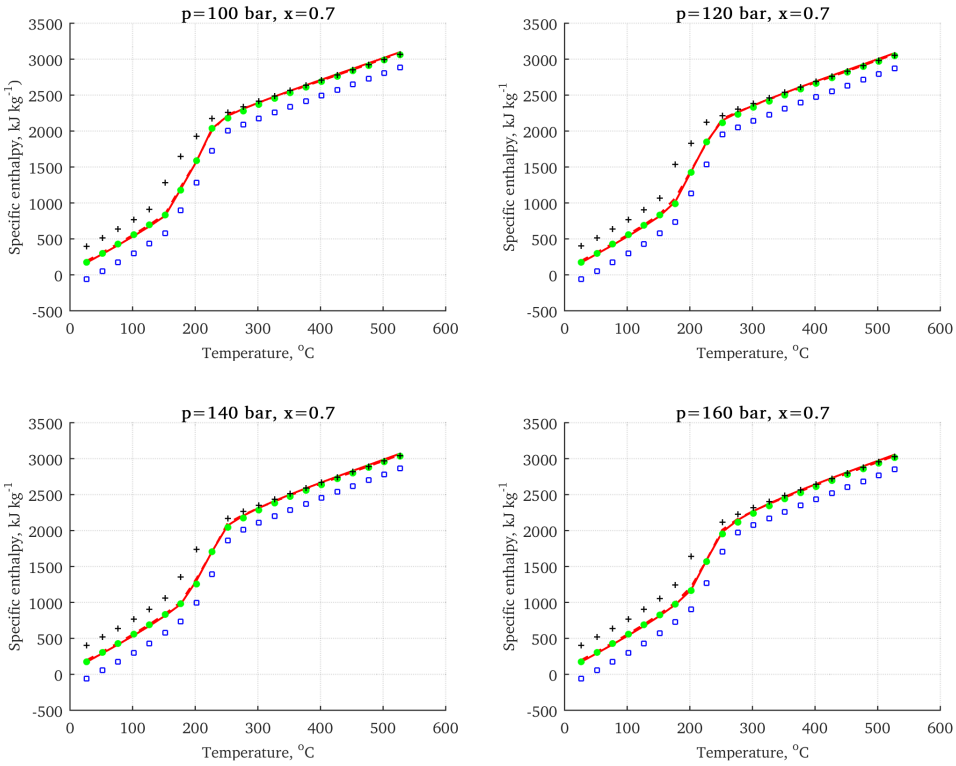

Figure A.21: Specific enthalpy at high pressures for an ammonia mass fraction of 0.7.

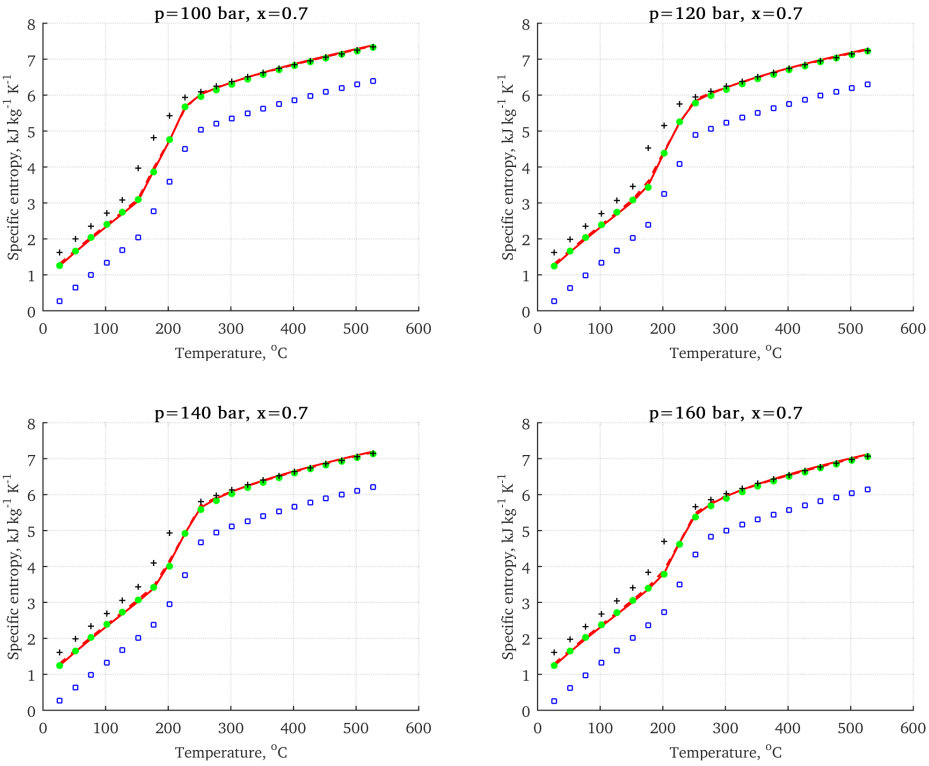

Figure A.22: Specific entropy at high pressures for an ammonia mass fraction of 0.7.

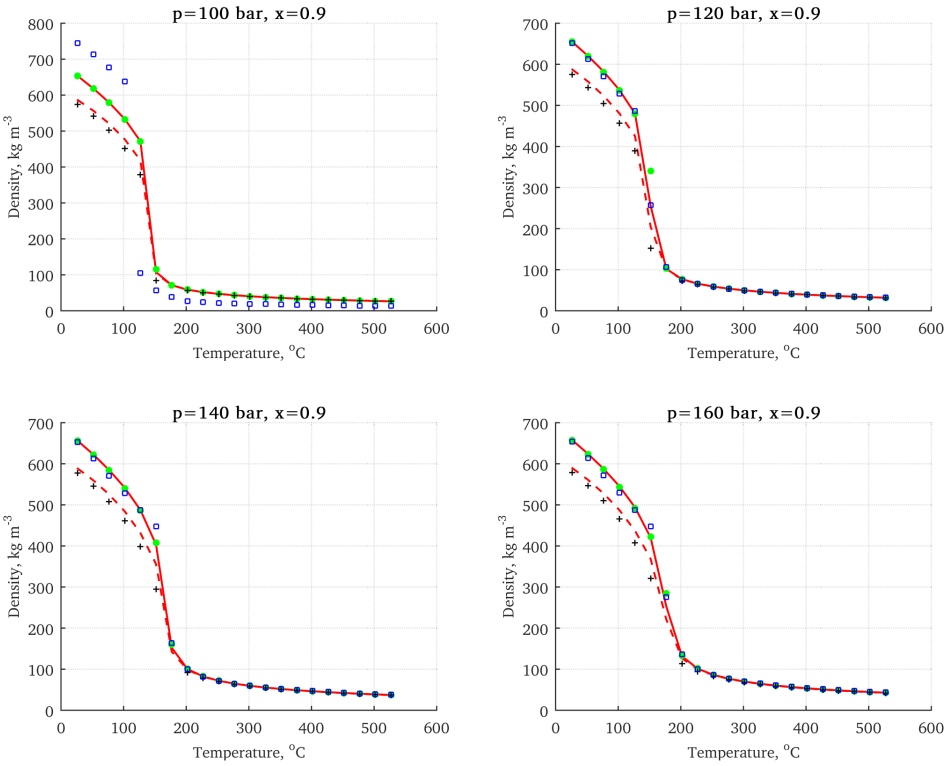

Figure A.23: Density at high pressures for an ammonia mass fraction of 0.9.

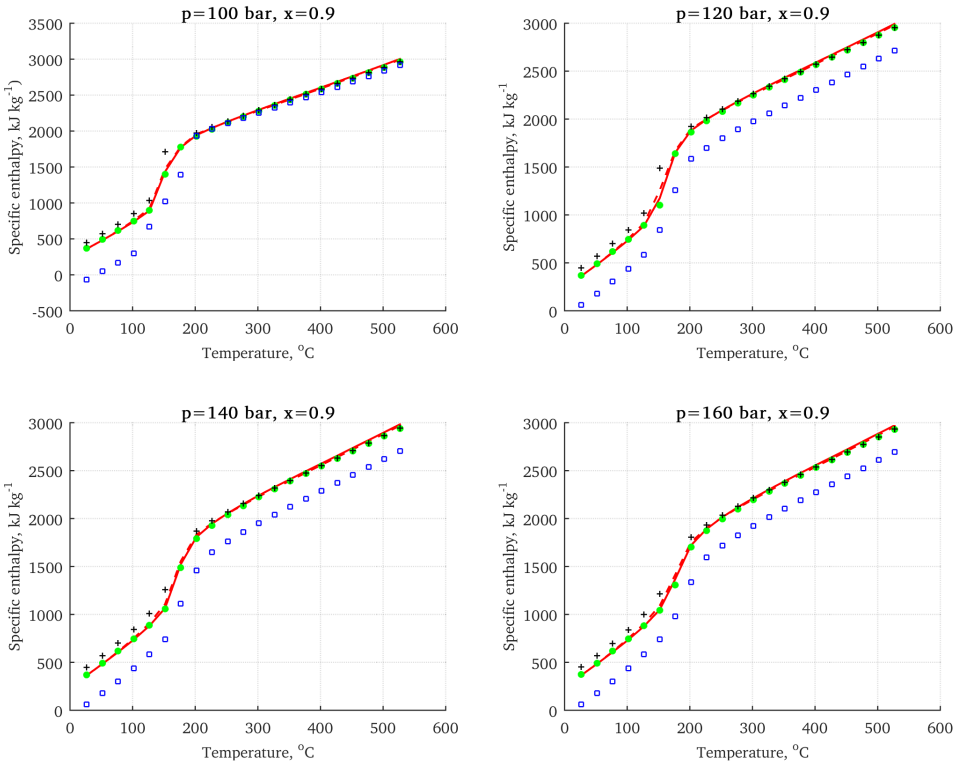

Figure A.24: Specific enthalpy at high pressures for an ammonia mass fraction of 0.9.

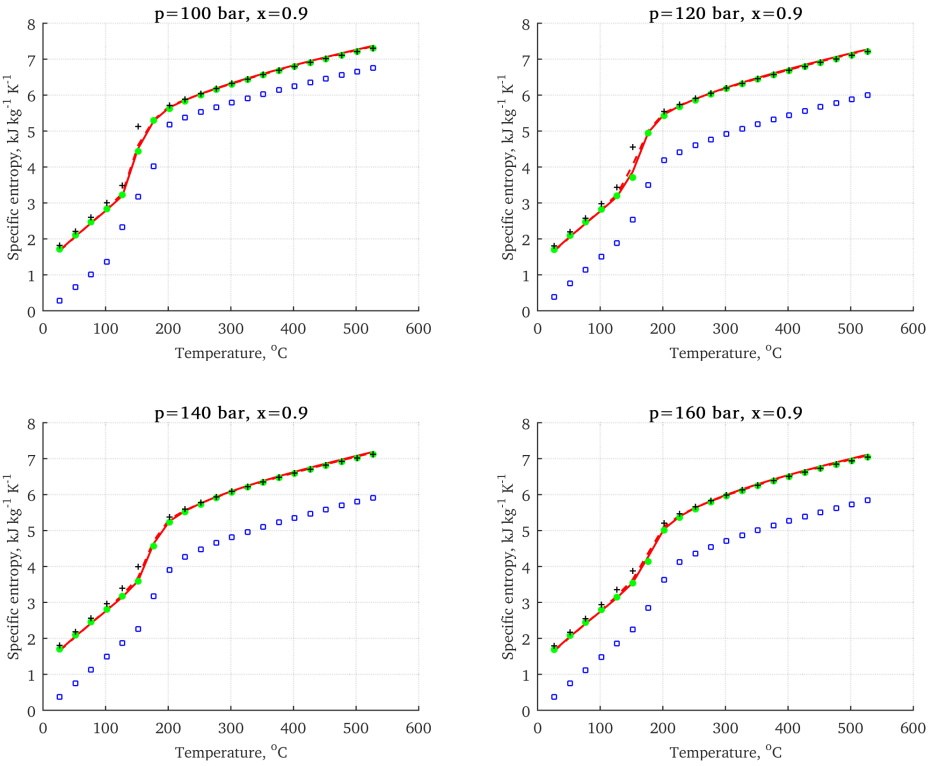

Figure A.25: Specific entropy at high pressures for an ammonia mass fraction of 0.9.

B

CORRELATIONS

As the correlations include several parameters and factors specific to particular equations, these are elaborated within the text here and not included in the main nomenclature at the beginning of the thesis.

B.1 Transport properties

The correlations for transport properties of ammonia-water mixtures presented by El-Sayed [67] as reported in Thorin [64] are as follows:

For the gas phase:

$$\mu_{mix} = \frac{\mu_{amm} \cdot x}{x + f_1 \cdot (1-x)} + \frac{\mu_{wat} \cdot (1-x)}{(1-x) + f_2 \cdot x} \tag{B.1a}$$

$$\lambda_{mix} = \frac{\lambda_{amm} \cdot x}{x + f_1 \cdot (1-x)} + \frac{\lambda_{wat} \cdot (1-x)}{(1-x) + f_2 \cdot x} \tag{B.1b}$$

$$f_1 = \frac{[1 + (\mu_{amm}/\mu_{wat})^{0.5} \cdot (M_{wat}/M_{amm})^{0.25}]^2}{[8 \cdot (1 + (M_{amm}/M_{wat}))]^{0.5}} \tag{B.1c}$$

$$f_2 = F_{12} \cdot \left(\frac{\mu_{wat}}{\mu_{amm}}\right) \cdot \left(\frac{M_{amm}}{M_{wat}}\right) \tag{B.1d}$$

For the liquid phase:

$$\ln \mu_{mix} = x \cdot \ln \mu_{amm} + (1-x) \cdot \ln \mu_{wat} + f_3 \tag{B.2a}$$

$$\lambda_{mix} = x \cdot \lambda_{amm} + (1-x) \cdot \lambda_{wat} \tag{B.2b}$$

$$T_{red} = \frac{T_{mix}}{T_{crit,mix}} = \frac{T_{amm}}{T_{crit,amm}} = \frac{T_{wat}}{T_{crit,wat}} \tag{B.2c}$$

$$f_3 = f_4 \cdot f_5 \tag{B.2d}$$

$$f_4 = 4.219 - 3.7996 \cdot \left(\frac{1.8 \cdot T_{mix}}{492}\right) + 0.842 \cdot \left(\frac{1.8 \cdot T_{mix}}{492}\right)^2 \tag{B.2e}$$

$$f_5 = \left[x \cdot (1-x) - 0.125 \cdot x^2 \cdot (1-x)\right] \cdot \{\ln(\mu_{amm} \cdot \mu_{wat})\}^{0.5} \tag{B.2f}$$

where for the liquid phase equations (Equation (B.2)), the dynamic viscosity (μ) is in µPa s. The pure fluid transport properties were obtained from REFPROP. In the equations, the subscripts 'amm' and 'wat' denote ammonia and water, respectively, λ is the thermal conductivity, x is the ammonia mass fraction, T is the temperature, and M is the molar mass.

B.2 Heat transfer coefficients

For the **single phase in-tube flow** (both liquid and vapour), the heat transfer coefficient was estimated using:

$$\alpha = \frac{\lambda \cdot Nu}{D_i} \tag{B.3}$$

where α is the fluid heat transfer coefficient, λ is the fluid thermal conductivity, and D_i is the tube inside diameter. The Nusselt number (Nu) was calculated using the Gnielinski (1976) correlation [129]:

$$Nu = \frac{(f_{\text{fric}}/8) \cdot (Re - 1000) \cdot Pr}{1 + [12.7 \cdot (f_{\text{fric}}/8)^{1/2} \cdot (Pr^{2/3} - 1)]} \tag{B.4}$$

where Re is the Reynolds number and Pr is the Prandtl number. The friction factor (f_{fric}) was estimated using the Petukhov (1970) equation [129]:

$$f_{\text{fric}} = (0.790 \cdot \ln Re - 1.64)^{-2} \tag{B.5}$$

For the **single phase shell-side flow** (btoh liquid and vapour), the heat transfer coefficient was estimated using the Kern (1950) [133] correlation as presented in Smith [127]:

$$\alpha = \alpha_{\text{ideal}} \cdot f_{\text{hn}} \cdot f_{\text{hw}} \cdot f_{\text{hb}} \cdot f_{\text{hL}} \tag{B.6}$$

where α_{ideal} is the shell-side heat transfer coefficient for ideal cross flow, f_{hn} is the correction factor to allow for the effect of the number of tube rows crossed, f_{hw} is the window correction factor, f_{hb} is the bypass stream correction factor, and f_{hL} is the leakage correction factor. The factors f_{hn}, f_{hw}, f_{hb}, and f_{hL} were conservatively assumed to be 1, 1, 0.8, and 0.8, respectively, for a well-designed heat exchanger as suggested in Smith [127]. The ideal heat transfer coefficient (α_{ideal}) was estimated using:

$$\alpha_{\text{ideal}} = j_h \cdot c_p \cdot G \cdot Pr^{-2/3} \tag{B.7}$$

where c_p is the isobaric specific heat capacity and G is the mass flux. The effect of the ratio of the bulk to wall fluid viscosity was neglected as suggested in Sinnott [128], except when using thermal oil in the boiler for a parabolic trough CSP plant. The heat transfer factor (j_h) was calculated assuming a 25 % baffle cut using [127]:

$$j_h = 0.24 \cdot Re^{-0.36} \tag{B.8}$$

The **evaporating in-tube flow** heat transfer coefficient ($\alpha_{\text{tp,evap}}$) was estimated using the Shah (1982) correlation [132]:

$$\alpha_{\text{tp,evap}} = \chi \cdot \alpha_{\text{lo}} \tag{B.9a}$$

$$\alpha_{\text{lo}} = 0.023 \cdot \frac{\lambda_{\text{liq}}}{D} \cdot \left\{ \frac{G \cdot (1-X) \cdot D_i}{\mu_{\text{liq}}} \right\}^{0.8} \cdot Pr_{\text{liq}}^{0.4} \tag{B.9b}$$

$$Pr_{\text{liq}} = \frac{\mu_{\text{liq}} \cdot c_{p,\text{liq}}}{\lambda_{\text{liq}}} \tag{B.9c}$$

where α_{lo} is the liquid-only heat transfer coefficient, Pr_{liq} is the liquid Prandtl number, and μ_{liq}, $c_{p,\text{liq}}$ and λ_{liq} are respectively the viscosity, the isobaric specific heat capacity and the thermal conductivity of the liquid part. X is the vapour quality, G is the total mass flux, and D_i is the tube inside diameter. The factor χ was calculated using Equations (B.10) to (B.12).

For $f_{\text{tp,evap}} > 1.0$:

$$\chi_{\text{nb}} = \begin{cases} 230 \cdot Bo^{0.5} & Bo > 0.00003 \\ 1 + 46 \cdot Bo^{0.5} & Bo \leq 0.00003 \end{cases} \tag{B.10a}$$

$$\chi_{\text{cb}} = \frac{1.8}{N_s^{0.8}} \tag{B.10b}$$

$$\chi = \max(\chi_{\text{nb}}, \chi_{\text{cb}}) \tag{B.10c}$$

For $0.1 < f_{\text{tp,evap}} \leq 1.0$:

$$\chi_{\text{bs}} = f_{\text{sh}} \cdot Bo^{0.5} \cdot \exp(2.47 \cdot N_s^{-0.1}) \tag{B.11a}$$

$$\chi_{\text{cb}} = \frac{1.8}{N_s^{0.8}} \tag{B.11b}$$

$$\chi = \max(\chi_{\text{bs}}, \chi_{\text{cb}}) \tag{B.11c}$$

For $f_{\text{tp,evap}} \leq 0.1$:

$$\chi_{\text{bs}} = f_{\text{sh}} \cdot Bo^{0.5} \cdot \exp(2.47 \cdot N_s^{-0.15}) \tag{B.12a}$$

$$\chi_{\text{cb}} = \frac{1.8}{N_s^{0.8}} \tag{B.12b}$$

$$\chi = \max(\chi_{\text{bs}}, \chi_{\text{cb}}) \tag{B.12c}$$

In Equations (B.11) and (B.12), the constant f_{sh} is calculated using:

$$f_{\text{sh}} = \begin{cases} 14.70 & Bo \geq 0.0011 \\ 15.43 & Bo < 0.0011 \end{cases} \tag{B.13}$$

The factor $f_{\text{tp,evap}}$ was calculated using Equations (B.14) and (B.15). For all values of Fr_{lo}

for vertical tubes, and for $Fr_{\text{lo}} \geq 0.04$ for horizontal tubes:

$$f_{\text{tp,evap}} = Co \tag{B.14}$$

For horizontal tubes with $Fr_{\text{lo}} < 0.04$:

$$f_{\text{tp,evap}} = 0.38 \cdot Fr_{\text{lo}}^{-0.3} \cdot Co \tag{B.15}$$

In Equations (B.10) to (B.15), Co is the convection number, Bo is the boiling number, and Fr_{lo} is the liquid-only Froude number, and were calculated using the following equations:

$$Co = \left(\frac{1}{X} - 1\right)^{0.8} \left(\frac{\rho_{\text{vap}}}{\rho_{\text{liq}}}\right)^{0.5} \tag{B.16a}$$

$$Bo = \frac{q''}{G \cdot h_{fg}} \tag{B.16b}$$

$$Fr_{\text{lo}} = \frac{G^2}{\rho_{\text{liq}}^2 \cdot g \cdot D_i} \tag{B.16c}$$

where ρ_{liq} and ρ_{vap} are respectively the densities of the vapour and the liquid parts, q'' is the heat flux, h_{fg} is the latent heat of vaporization, g is the acceleration due to gravity, and D_i is the tube inside diameter.

Since the Shah (1982) [132] correlation is dependent on the heat flux, the heat transfer area of each control volume was calculated iteratively. Care must be taken when calculating the liquid or the vapour properties as the ammonia mass fraction would be different in the two phases, and therefore the ammonia mass fraction of the respective phase must be used in calculation of the thermodynamic and transport properties of that phase.

The **condensing in-tube flow** heat transfer coefficient was estimated using the Shah (2013) correlation with the Silver-Bell-Ghaly correction [130,131], as is recommended for fluid mixtures. It was assumed that the heat exchangers are in horizontal orientation, therefore the Regime I for the estimation of the heat transfer coefficient occurs when:

$$J_g \geq 0.98 \cdot (Z_s + 0.263)^{-0.62} \tag{B.17}$$

where J_g is the dimensionless vapour velocity defined as follows:

$$J_g = \frac{G \cdot X}{\sqrt{g \cdot D_i \cdot \rho_{\text{vap}} \cdot (\rho_{\text{liq}} - \rho_{\text{vap}})}} \tag{B.18}$$

The Regime III occurs when both Re_{LS} and Re_{GS} are less than 1000, which were obtained

from:

$$Re_{\mathrm{LS}} = \frac{G \cdot (1-X) \cdot D_i}{\mu_{\mathrm{liq}}} \tag{B.19a}$$

$$Re_{\mathrm{GS}} = \frac{G \cdot X \cdot D_i}{\mu_{\mathrm{vap}}} \tag{B.19b}$$

The rest of the space is termed as Regime II. The two-phase flow heat transfer coefficient was then estimated using:

$$\alpha_{\mathrm{tp}} = \begin{cases} \alpha_{\mathrm{I}} & \text{for Regime I} \\ \alpha_{\mathrm{I}} + \alpha_{\mathrm{Nu}} & \text{for Regime II} \\ \alpha_{\mathrm{Nu}} & \text{for Regime III} \end{cases} \tag{B.20}$$

where α_{I} and α_{Nu} were obtained from:

$$\alpha_{\mathrm{I}} = \alpha_{\mathrm{LS}} \cdot \left[1 + \frac{3.8}{Z_s^{0.95}}\right] \cdot \left(\frac{\mu_{\mathrm{liq}}}{14 \cdot \mu_{\mathrm{vap}}}\right)^{0.0058+0.557 \cdot p_{\mathrm{red}}} \tag{B.21a}$$

$$\alpha_{\mathrm{Nu}} = 1.32 \cdot Re_{\mathrm{LS}}^{-1/3} \cdot \left[\frac{\rho_{\mathrm{liq}} \cdot (\rho_{\mathrm{liq}} - \rho_{\mathrm{vap}}) \cdot g \cdot \lambda_{\mathrm{liq}}^3}{\mu_{\mathrm{liq}}^2}\right]^{1/3} \tag{B.21b}$$

$$Z_s = \left(\frac{1}{X} - 1\right)^{0.8} \cdot p_{\mathrm{red}}^{0.4} \tag{B.21c}$$

where p_{red} is the reduced pressure. α_{LS} was calculated using Equation (B.9b). The calculated α_{tp} was then corrected for mixtures as follows:

$$\alpha_{\mathrm{tp,cond}} = \left[\frac{1}{\alpha_{\mathrm{tp}}} + \frac{Z_v}{\alpha_{\mathrm{vap}}}\right]^{-1} \tag{B.22a}$$

$$Z_v = X \cdot c_{p,\mathrm{vap}} \cdot \frac{\Delta T}{\Delta h} \tag{B.22b}$$

$$\alpha_{\mathrm{vap}} = 0.023 \cdot \frac{\lambda_{\mathrm{vap}}}{D_i} \cdot \left\{\frac{G \cdot X \cdot D_i}{\mu_{\mathrm{vap}}}\right\}^{0.8} \cdot Pr_{\mathrm{vap}}^{0.4} \tag{B.22c}$$

$$Pr_{\mathrm{vap}} = \frac{\mu_{\mathrm{vap}} \cdot c_{p,\mathrm{vap}}}{\lambda_{\mathrm{vap}}} \tag{B.22d}$$

where ΔT and Δh are respectively the temperature and the specific enthalpy differences on the tube side, across the control volume under consideration.

The **shell-side condensing flow** heat transfer coefficient was estimated using the Kern (1950) [133] correlation as presented in Smith [127]:

$$\alpha_{\text{tp}} = 0.954 \cdot \lambda_{\text{liq}} \cdot N_R^{-1/6} \cdot \left(\frac{\rho_{\text{liq}}^2 \cdot L \cdot g \cdot N_T}{\dot{m} \cdot \mu_{\text{liq}}} \right)^{1/3} \tag{B.23a}$$

$$N_R = 0.78 \cdot \frac{D_s}{p_{tt}} \tag{B.23b}$$

where the equations, N_T is the total number of tubes, L is the tube length for the control volume under consideration in m (representative of the heat transfer area), N_R is the number of tubes in a vertical row inside the shell, D_s is the equivalent shell diameter, $\dot{m}$ is the shell-side mass flow rate, and p_{tt} is the vertical tube pitch.

The calculated α_{tp} was then corrected for mixtures using Equation (B.22a) with Z_v obtained from Equation (B.22b), and α_{vap} obtained from Equation (B.7) as suggested in Trapp and Colonna [153]. The effect of the ratio of the bulk to wall fluid viscosity was neglected [128]. In order to estimate α_{vap} using Equation (B.7), $c_{p,\text{vap}}$ and Pr_{vap} must be used in place of c_p and Pr, respectively. Since the heat transfer coefficient is dependent on the tube length (and thus the heat transfer area), the heat transfer area of each control volume was calculated iteratively.

C

SOLUTION ALGORITHM AND HEAT EXCHANGER PROFILES

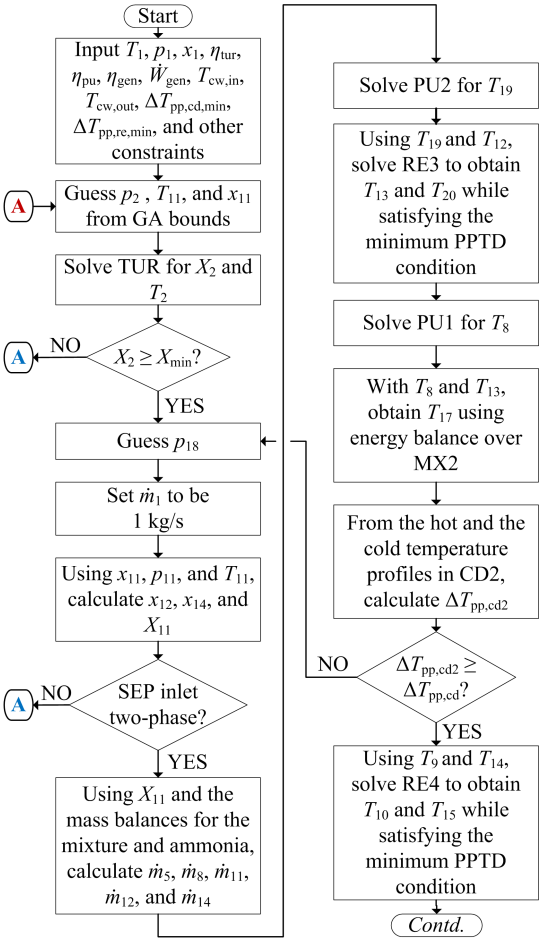

Figure C.1: Solution algorithm for every iteration of the KC1234 layout; continued on next page.

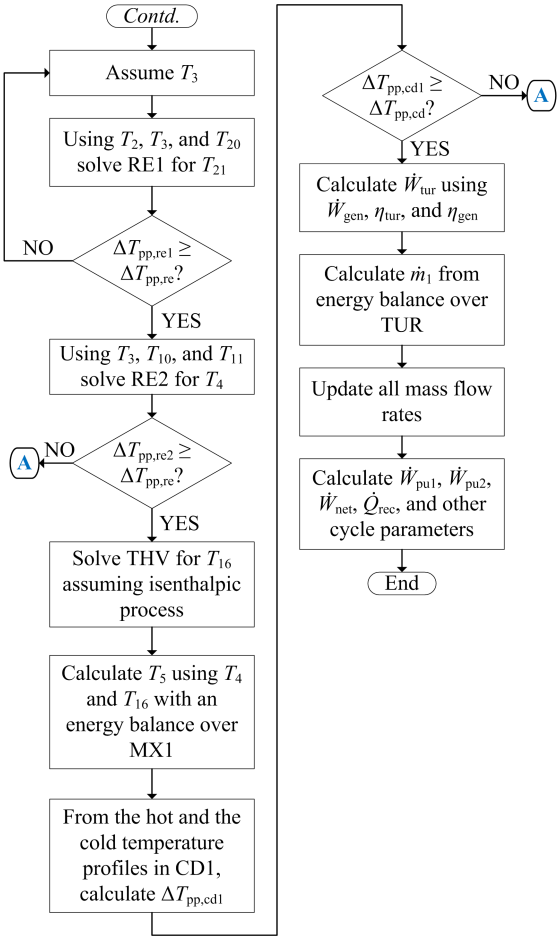

The exemplary heat exchanger profiles (T-$\dot{Q}$ plots) for the thermodynamic optimum at a turbine inlet pressure and ammonia mass fraction of 100 bar and 0.7 for the four high temperature Kalina cycle layouts (KC12, KC123, KC234, and KC1234) for a central receiver CSP plant are shown in Figures C.2 to C.5.

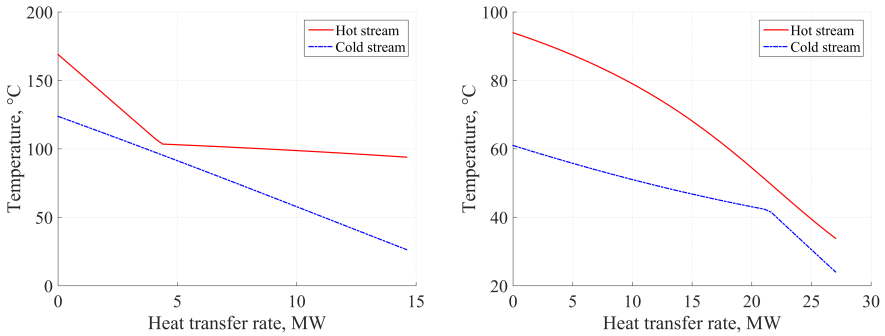

(a) Recuperator RE1.

(b) Recuperator RE2.

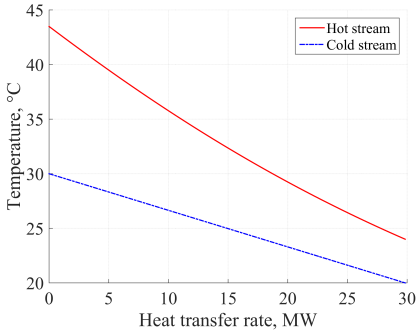

(c) Condenser CD1.

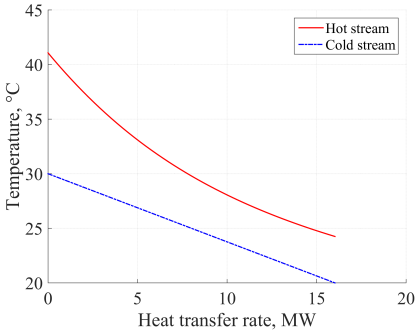

(d) Condenser CD2.

Figure C.2: Heat exchanger temperature profiles for Kalina cycle KC12 for the thermodynamic optimum for a turbine inlet pressure, temperature, and ammonia mass fraction of 100 bar, 500 °C, and 0.7.

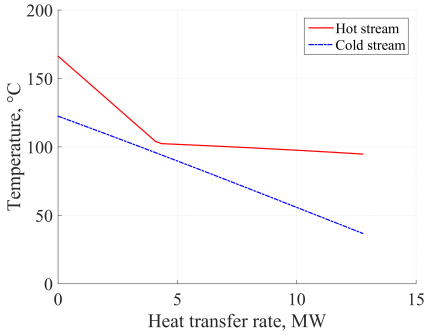

(a) Recuperator RE1.

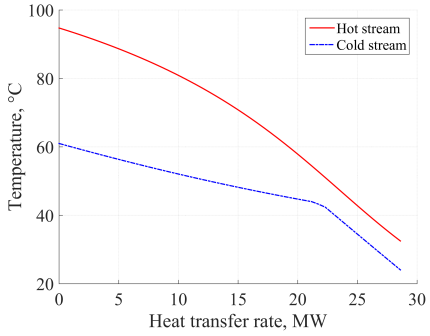

(b) Recuperator RE2.

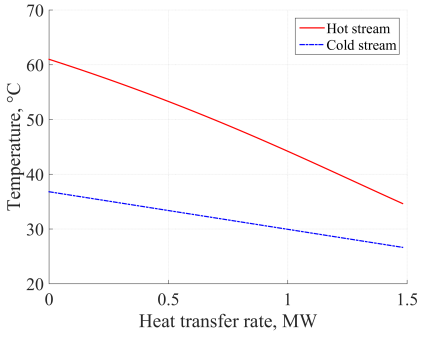

(c) Recuperator RE3.

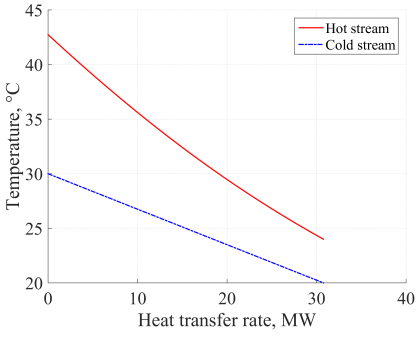

(d) Condenser CD1.

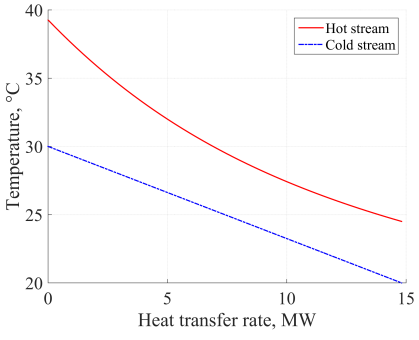

(e) Condenser CD2.

Figure C.3: Heat exchanger temperature profiles for Kalina cycle KC123 for the thermodynamic optimum for a turbine inlet pressure, temperature, and ammonia mass fraction of 100 bar, 500 °C, and 0.7.

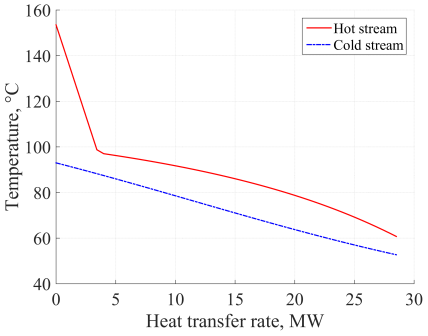

(a) Recuperator RE2.

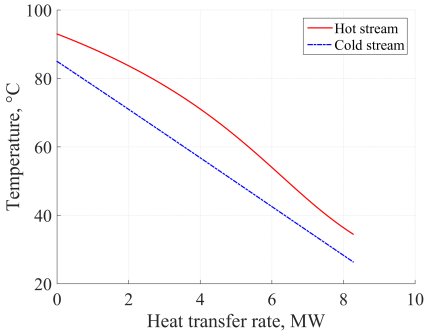

(b) Recuperator RE3.

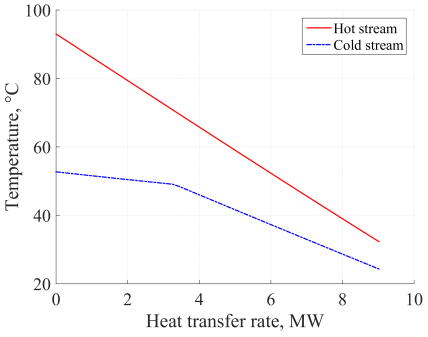

(c) Recuperator RE4.

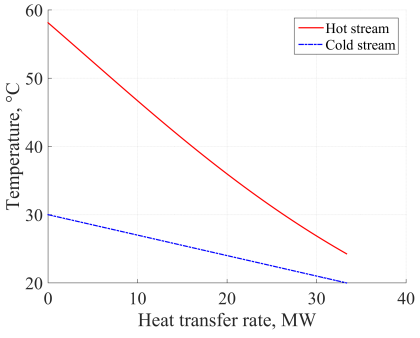

(d) Condenser CD1.

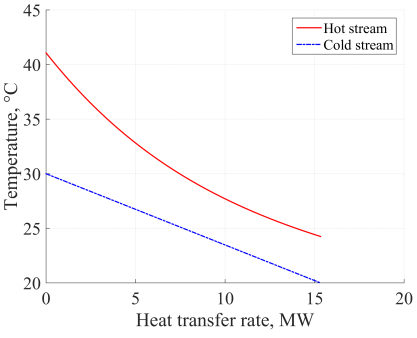

(e) Condenser CD2.

Figure C.4: Heat exchanger temperature profiles for Kalina cycle KC234 for the thermodynamic optimum for a turbine inlet pressure, temperature, and ammonia mass fraction of 100 bar, 500 °C, and 0.7.

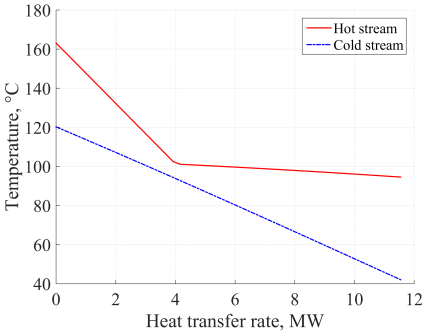

(a) Recuperator RE1.

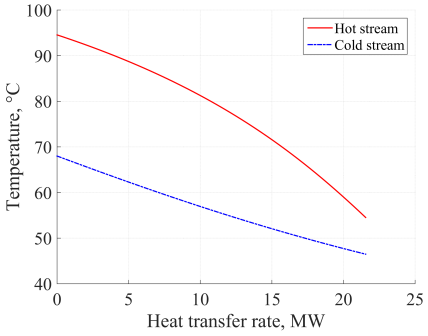

(b) Recuperator RE2.

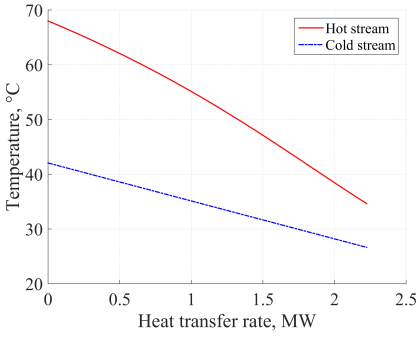

(c) Recuperator RE3.

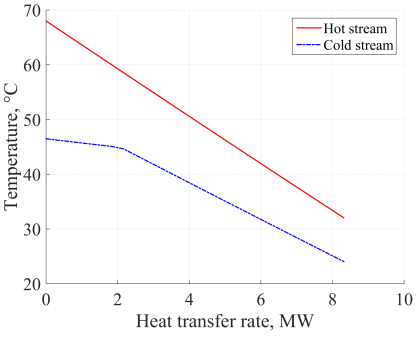

(d) Recuperator RE4.

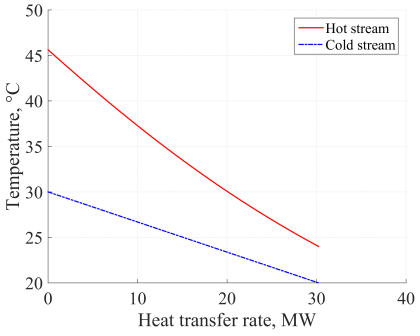

(e) Condenser CD1.

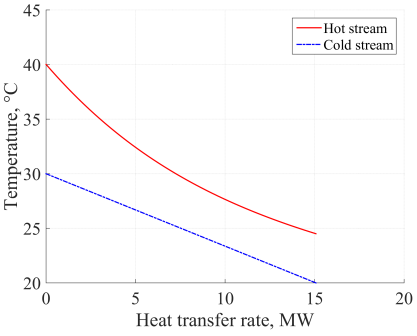

(f) Condenser CD2.

Figure C.5: Heat exchanger temperature profiles for Kalina cycle KC1234 for the thermodynamic optimum for a turbine inlet pressure, temperature, and ammonia mass fraction of 100 bar, 500 °C, and 0.7.

D

DELSOL3 INPUT PARAMETERS

An exemplary input code used for the first run of DELSOL3 to design the heliostat field for a central receiver CSP plant with the absorbed heat in the receiver equal to 70 MW is shown below:

```
&BASIC
iprob=4
itape=1
plat=37.25
refsol=0.9
/
&FIELD
radmax=9.00
/
&HSTAT
sigsy=.001
rmirl=.893
sigaz=.00075
icant=-1
/
&REC
towl=100
rrecl=0.94
iautop=0
/
&NLFLUX
/
&NLEFF
smult=1.3
iph=1
/
&REC
iautop=1
/
&OPT
numtht=20
thtst=40.0
thtend=100.0
numrec=20
wst=4.0
wend=12.0
numhtw=20
htwst=0.5
htwend=2.0
ioptum=1
numopt=1
poptmn=70.e+06
poptmx=70.e+06
iall=0
smult=1.3
iplfl=1
iotape=1
irerun=1
/
&NLFLUX
iflx=1
nxflx=4
nflxmx=4
fazmin=0
```

```
fazmax=270
flxlim(1)=6.e+05
flxlim(2)=6.e+05
flxlim(3)=6.e+05
flxlim(4)=6.e+05
/
&NLEFF
smult=1.3
iph=1
/
&NLCOST
crpref=0.0
cspref=0.0
chpref=0.0
ccpref=0.0
cstref=0.0
cstrmd=0.0
cheref=0.0
/
&NLECON
/
&REC
w=-100.
/
```

The input code to generate the heliostat field efficiency in a second DELSOL3 run for the same case as above is as follows:

```
&BASIC
iprob=3
itape=3
tdesp=70.
uel(1)=0
uel(2)=25
uel(3)=45
uel(4)=65
uel(5)=75
uel(6)=90
/
&FIELD
/
&HSTAT
/
&REC
/
&NLFLUX
/
&NLEFF
/
&REC
w=-100.
/
```

GLOSSARY

Absorptivity
The fraction of the incident energy absorbed by a surface.

Ammonia-water basic solution
In a high temperature Kalina cycle (e.g. Figure 3.5), the basic solution refers to the ammonia mass fraction through the first condenser and entering the separator.

Ammonia-water lean liquid
In a high temperature Kalina cycle (e.g. Figure 3.5), the lean liquid refers to the ammonia mass fraction of the liquid stream from the vapour-liquid separator.

Ammonia-water rich vapour
In a high temperature Kalina cycle (e.g. Figure 3.5), the rich vapour refers to the ammonia mass fraction of the vapour stream from the vapour-liquid separator.

Ammonia-water working solution
In a high temperature Kalina cycle (e.g. Figure 3.5), the working solution refers to the ammonia mass fraction through the boiler. In the configurations considered in this thesis, it is the same as the turbine inlet ammonia mass fraction.

Atmospheric attenuation
The loss of solar power due to the absorption and scattering of the reflected radiation from the collector before it reaches the receiver.

Azeotropic mixture
A mixture of two or more fluids for which the compositions of the liquid and vapour phases are the same for at least one combination of temperature and pressure.

Blocking
The blocking of a portion of the reflected sunlight from one collector, by another collector.

Concentrating solar power
The concentration of the incident solar radiation by reflecting it on a smaller area, thereby increasing the heat flux.

Cosine loss
The reduction in the projected collector area visible to the sun caused by the geometry and tilt of the collector.

Declination angle
The angle between the equator and a line drawn from the centre of the earth to the centre of the sun at solar noon.

Design condition
The nominal operating condition for the power plant, i.e. the operating state for which the plant was designed.

Diffuse radiation
The solar radiation scattered by the atmosphere.

Direct normal irradiance
The direct solar radiation on a surface perpendicular to the sun's rays.

Direct radiation
The incident solar radiation without being scattered by the atmosphere. Also referred to as beam radiation.

Direct steam generation
The conversion of the water to steam in the solar receiver of a steam Rankine cycle CSP plant.

Direct vapour generation
The conversion of the liquid ammonia-water mixture to vapour in the solar receiver of a Kalina cycle CSP plant.

Emissivity
The ratio of the radiant energy emitted by a surface to that emitted by a black body of the same temperature and area.

Geometric concentration ratio
The ratio of the collector aperture area to the receiver area for a CSP plant.

Heat transfer fluid
The fluid that transports the heat from the solar receiver to the power cycle, e.g. thermal oils and molten salts. In case of a direct steam or vapour generation configuration, the heat transfer fluid and the power cycle working fluid are the same.

Irradiance
The incident solar radiation power per unit area of a surface, measured in $\mathrm{W\,m^{-2}}$.

Irradiation
The incident solar radiation energy per unit area of a surface, measured in $\mathrm{J\,m^{-2}}$.

Levelized cost of electricity
The average cost the generated electricity by a power plant considering all the direct and indirect costs.

Nameplate capacity
See *Rated capacity*.

Part-load condition
Any operating state for the plant other than the design condition, typically because of a change in the available heat input or the desired power output, and usually a state with less net power generation than the design condition. Also referred to as off-design operating condition.

Plant capacity factor
The ratio of the actual electricity generated over a period to the maximum possible electricity generation over the same period. The maximum possible electricity generation would occur if the power plant is always operated at its rated capacity.

Plant location
The plant site coordinates represented by the latitude and the longitude.

Power cycle
The set of equipment to convert heat into electrical power such as the Rankine cycle, the Kalina cycle, etc. Also referred to as the power block.

Power plant
The combination of the solar field, the power cycle, and the storage system, if any.

Rated capacity
The net electrical power output from the power plant at design condition. Also referred to as the plant nameplate capacity.

Reflectivity
The fraction of the incident energy which is reflected by a surface. It is considered to be the same as reflectance for the cases investigated in this thesis.

Shadowing
The shading of a portion of a collector's reflective part due to the proximity to another collector.

Solar azimuth angle
The angular displacement from south of the projection of direct radiation on the horizontal plane. The displacements east of south are negative and west of south are positive.

Solar collector
A generic term used to describe the reflecting part of the solar field which 'collects' the incident solar radiation. It would be the heliostat mirrors for a central receiver CSP plant and the parabolic troughs for a parabolic trough CSP plant.

Solar field
The solar collectors and receivers along with their auxiliaries, e.g. the central receiver, heliostats, and the tower for the central receiver CSP plant.

Solar multiple
The ratio of the power delivered by the solar field at design condition to the power required by the power cycle to operate at its nominal condition.

Solar receiver
A generic term used to describe the equipment which 'receives' the concentrated reflected radiation from the solar collector. It would be the tube bundles or ceramic foam for a central receiver CSP plant, and the receiver tube for a parabolic trough CSP plant.

Solar time
The time with respect to the position of the sun. Solar noon occurs when the sun is directly above the observer.

Spillage
The portion of the reflected radiation from the collector which fails to reach the receiver surface.

Temperature glide
The difference between the saturated liquid and the saturated vapour temperatures at a given pressure.

Transmissivity
The fraction of the incident energy which is transmitted through the surface.

Working fluid
The fluid that produces work by going through the turbine in a power plant. For example, it is ammonia-water mixture for a Kalina cycle, hot gas for a Brayton cycle,

and steam for a steam Rankine cycle.

Zenith angle
The angle between the vertical (zenith) and the line of sight to the sun.

Zeotropic mixture
A mixture of two or more fluids for which the compositions of the liquid and vapour phases are always different in phase equilibrium, i.e. the phase change occurs with a temperature glide.

DTU Mechanical Engineering
Section of Thermal Energy
Technical University of Denmark

Nils Koppels Allé, Bld. 403
DK- 2800 Kgs. Lyngby
Denmark
Phone (+45) 4525 4131
Fax (+45) 4588 4325
www.mek.dtu.dk
ISBN: 978-87-7475-430-5

DCAMM
Danish Center for Applied Mathematics and Mechanics

Nils Koppels Allé, Bld. 404
DK-2800 Kgs. Lyngby
Denmark
Phone (+45) 4525 4250
Fax (+45) 4593 1475
www.dcamm.dk
ISSN: 0903-1685